

**STRUCTURAL AND BIOCHEMICAL CHARACTERIZATIONS OF THE SKELETAL
MUSCLE AND CARDIAC RYANODINE RECEPTOR N-TERMINAL DISEASE-
ASSOCIATED MUTANTS**

by

Lynn Kimlicka

B.Sc. Hon., The University of British Columbia, 2009

A THESIS SUBMITTED IN PARTIAL FULFILLMENT OF
THE REQUIREMENTS FOR THE DEGREE OF

DOCTOR OF PHILOSOPHY

in

THE FACULTY OF GRADUATE AND POSTDOCTORAL STUDIES
(Biochemistry and Molecular Biology)

THE UNIVERSITY OF BRITISH COLUMBIA
(Vancouver)

April 2014

© Lynn Kimlicka, 2014

Abstract

Ryanodine receptors (RyRs) are calcium release channels located in the endo/sarcoplasmic reticulum that play a crucial role in the excitation-contraction coupling. Over 500 mutations have been found in the skeletal muscle (RyR1) and cardiac (RyR2) isoforms that cause severe muscle disorders or life-threatening arrhythmias. Mechanisms of these mutations have remained elusive largely due to the lack of high-resolution structures. Here, we compare pseudo-atomic models of the N-terminal region of RyR1 in the open and closed states together with crystal structures and thermal melts of multiple disease-associated mutants. We describe a model in which the intersubunit interface at the N-terminal region acts as a brake in channel opening. Next, we depict crystal structures of mutants at the intersubunit interface of RyR2 N-terminal region that perturb the structure of a loop targeted by multiple mutations. Furthermore, the crystal structure of the N-terminal domains of RyR2 reveals a unique, central anion-binding site. This anion binding is ablated in a disease-associated mutant that targets one of the anion-coordinating arginine residues, resulting in domain reorientations. Several other disease-causing mutations destabilize the protein. Taken together, the results illustrate a common theme across the RyR isoforms and their homologous IP₃ receptors that conformational changes at the N-terminal region caused by the destabilization of the interfaces are allosterically coupled to channel opening.

Preface

The Introduction (Chapter 1) is adapted from two previous publications with several updates based on recent studies. The majority of Sections 1.1 and 1.2 come from portions of a chapter in a book, from the sections my supervisor and I have written: Yuchi, Z., Kimlicka, L., and Van Petegem, F. Structural Insights Into Disease Mutations of the Ryanodine Receptor. *Genetic Disorders, InTech*, 2013, Chapter 5:105-141. The rest of the Introduction is based on a review article I have written with my supervisor: Kimlicka, L. and Van Petegem, F. The structural biology of ryanodine receptors. *Sci. China Life Sci.*, 2011, 54(8):712-724.

Chapter 2 is based on the work published in Kimlicka, L., Lau, L., Tung, C.C., and Van Petegem, F. Disease mutations in the ryanodine receptor N-terminal region couple to a mobile intersubunit interface. *Nature Commun.*, 2013, 4:1506, DOI:10.1038/ncomms2501. I cloned, expressed, and purified all the disease-associated mutants, collected the diffraction data, solved their structures, and performed the thermal melt, CD spectroscopic, cross-linking, pull-down, and dynamic light scattering experiments. Kelvin Lau purified FKBP12 and performed the corresponding ITC experiment. Ching-Chieh Tung crystallized RyR1BC and RyR1ABC at different pH levels, performed diffraction experiments and carried out the ITC experiments between domains A and BC. My supervisor designed and supervised the project, performed the docking experiments, solved RyR1BC structure, and wrote the manuscript.

Chapter 3 is adapted from a portion of the work published in collaboration with the laboratory of Dr. Mitsuhiro Ikura (University of Toronto): Amador, F.J., Kimlicka, L., Stathopoulos, P.B., Gasami-Seabrook, G.M.C., MacLennan, D.H., Van Petegem, F., and Ikura, M. Type 2 Ryanodine Receptor Domain A Contains a Unique and Dynamic α -Helix That

Transitions to a β -Strand in a Mutant Linked with a Heritable Cardiomyopathy. *J. Mol. Biol.*, 2013, 425(21):4034-4046. My supervisor prepared the disease-associated mutants and obtained crystals. I collected the diffraction data and solved the crystal structures. Fernando J. Amador performed the NMR experiments.

The majority of Chapter 4 is based on the work published in Kimlicka, L., Tung, C.C., Carlsson, A.C.C., Lobo, P.A., Yuchi, Z., and Van Petegem, F. The Cardiac Ryanodine Receptor N-Terminal Region Contains an Anion Binding Site that Is Targeted by Disease Mutations. *Structure*, 2013, 21(8):1440-1449. I performed all mutagenesis, expressed, purified, and crystallized the R420Q mutant, collected its diffraction data and solved its structure, and performed thermal melt experiments. I was also responsible for the training and supervision of Dr. Anna-Carin C. Carlsson, a visiting postdoctoral fellow from the laboratory of Dr. Mate Erdelyi (University of Gothenburg). Ching-Chieh Tung cloned, expressed, purified, and crystallized the wild-type RyR2ABC, collected its diffraction data, and assisted with thermal melt analysis. My supervisor solved the wild-type RyR2ABC structure, designed experiments, and wrote the manuscript. Paolo A. Lobo purified the RyR2ABC exon3 deletion mutant. Anna-Carin C. Carlsson purified some of the point mutants (L62F, F329L, T415R, and L433P). Zhinguang Yuchi helped design the experiments. The portion of Chapter 4 on the G230C mutant is based on a part of the work published in collaboration with the laboratory of Dr. Wayne Chen (University of Calgary): Liu, Y., Kimlicka, L., Hiess, F., Tian, X., Wang, R., Zhang, L., Jones, P.P., Van Petegem, F., and Chen, S.R.W. The CPVT-associated RyR2 mutation G230C enhances store overload induced Ca^{2+} release and destabilizes the N-terminal domains. *Biochem. J.*, 2013, 454(1):123-131. The homology model of the RyR2ABC structure in the original publication is now replaced with the actual crystal structure of RyR2ABC. I was responsible for the cloning,

expression, purification, and thermal melt analysis of the G230C RyR2ABC mutant. My supervisor wrote part of the manuscript. The rest of Chapter 4 is based on unpublished data. I prepared the R414C RyR2ABC mutant, collected its diffraction data, solved its structure, and performed thermal melt experiment. Paolo A. Lobo solved the crystal structure of the RyR1ABCD construct. Ching-Chieh Tung and I performed the ITC experiment using HMT-RyR2ABC. I crystallized the wild-type RyR2ABC protein in low KCl concentrations (both dialysis and crystal soaking experiments), collected their diffraction data and solved their structures, including the new wild-type structure with an additional α -helix in the β 22- β 23 loop.

The three topics discussed in the Conclusion (Chapter 5) were graciously suggested by my supervisor.

Table of Contents

Abstract.....	ii
Preface.....	iii
Table of Contents	vi
List of Tables	xi
List of Figures.....	xii
List of Abbreviations	xiv
Acknowledgements	xvi
Chapter 1: Introduction	1
1.1 Ryanodine receptors and genetic disease.....	5
1.1.1 Malignant hyperthermia.....	6
1.1.2 Core myopathies	7
1.1.3 Catecholaminergic polymorphic ventricular tachycardia	8
1.2 Functional studies of RyRs	8
1.2.1 Model systems	9
1.2.1.1 Native expression systems	9
1.2.1.2 Recombinant expression systems	10
1.2.1.3 <i>In vivo</i> systems.....	10
1.2.2 Methods.....	10
1.2.2.1 [⁴⁵ Ca ²⁺]-uptake and release assays.....	10
1.2.2.2 Whole-cell Ca ²⁺ fluorescence assays.....	11
1.2.2.3 [³ H]-ryanodine binding assays.....	11

1.2.2.4	Single-channel electrophysiology	11
1.2.3	Highlights of the results	12
1.2.3.1	Gain-of-function mutations.....	13
1.2.3.2	Loss-of-function mutations.....	13
1.2.3.3	Mutations with no discernible functional change	14
1.2.3.4	Remark on functional studies.....	15
1.3	Structural studies of RyRs	15
1.3.1	Cryo-EM studies of closed RyRs.....	16
1.3.2	Opening and closing	21
1.3.3	Insertion studies	24
1.3.3.1	N-terminal region.....	25
1.3.3.2	Central region.....	26
1.3.3.3	Divergent regions.....	27
1.3.3.4	Phosphorylation sites in the central region	28
1.3.3.5	Remark on insertion studies.....	28
1.3.4	Binding sites of protein binding partners.....	29
1.3.4.1	FK506-binding proteins	29
1.3.4.2	Calmodulin.....	30
1.3.4.3	Chloride intracellular channel 2.....	30
1.3.4.4	Toxins	31
1.3.5	X-ray crystallography and NMR	31
1.3.5.1	EF-hand proteins in complex with RyR peptides	31
1.3.5.1.1	CaM-peptide complex.....	32

1.3.5.1.2	S100A1	33
1.3.5.2	N-terminal region.....	34
1.3.5.2.1	Domain A of RyR1 and RyR2	34
1.3.5.2.2	Domains ABC of RyR1	36
1.3.5.2.3	Exon-3 deletion in domain A of RyR2	38
1.3.5.3	Phosphorylation domain in the central region	39
1.3.6	Pseudo-atomic models	41
1.3.6.1	Remark on docking reliability	41
1.3.6.2	N-terminal region: domains ABC.....	41
1.3.6.3	N-terminal region: residues 850-1060	43
1.3.6.4	Phosphorylation domain	44
1.3.7	Analogies with the inositol-1,4,5-triphosphate receptor.....	44
1.3.8	Research question	47
Chapter 2: Disease mutations in the ryanodine receptor N-terminal region couple to a		
mobile intersubunit interface.....		49
2.1	Methods.....	52
2.1.1	Cryo-EM docking	52
2.1.2	Cloning and crystallization of disease mutants.....	53
2.1.3	Data collection and refinement	54
2.1.4	Thermal melt analysis	56
2.1.5	CD spectra measurement	56
2.2	Results.....	57
2.2.1	Pseudo-atomic models of the N-terminal disease hot spot	57

2.2.2	Disease mutations can weaken the thermal stability.....	62
2.2.3	Buried disease mutations affect the intersubunit interface	65
2.2.4	Salt-bridge mutations cause relative domain-domain movements	67
2.2.5	Uncharged mutations at the A-B-C interfaces cause local changes	69
2.2.6	The relative orientation of domains B and C	72
2.3	Discussion	74
Chapter 3: The cardiac ryanodine receptor N-terminal domain contains a hot spot loop		
that is perturbed by disease-causing mutations		
80		
3.1	Methods.....	81
3.1.1	Cloning, expression, and purification	81
3.1.2	Crystallization and data collection.....	82
3.2	Results.....	83
3.3	Discussion	89
Chapter 4: The cardiac ryanodine receptor N-terminal region contains an anion-binding		
site that is targeted by disease-associated mutations		
93		
4.1	Methods.....	94
4.1.1	Cloning, purification, and crystallization of RyR2 N-terminal region	94
4.1.2	Data collection, structure solution, and refinement	95
4.1.3	Fluorescence-based thermal shift assays	97
4.2	Results.....	97
4.2.1	Overall structure of the RyR2 N-terminal region	97
4.2.2	Chloride can be exchanged	102
4.2.3	Chloride dissociation constant is below 4mM	103

4.2.4	The R420Q disease-associated mutation affects chloride binding	105
4.2.5	Additional RyR2 disease-associated mutations	108
4.2.6	Putative ligand binding sites	116
4.2.7	Interface 1 contains an additional α helix	118
4.3	Discussion	121
Chapter 5: Conclusion		128
5.1	Pseudo-atomic structures	129
5.2	Models of disease mutation mechanisms	132
5.3	Ligand-dependent modulation	135
5.4	Future directions	137
References		140
Appendices		187
Appendix A		187

List of Tables

Table 2.1: Crystallographic parameters.	55
Table 3.1: Data collection and refinement statistics.	82
Table 4.1: Crystallographic parameters.	96
Table 4.2: Interdomain salt bridges.	99
Table A.1: Summary from functional studies on RyR disease-associated mutations.	187

List of Figures

Figure 1.1: A schematic diagram of the components in E-C coupling.....	2
Figure 1.2: Disease hot spots.....	6
Figure 1.3: An overall structure of RyR.....	18
Figure 1.4: The pore-forming region.....	20
Figure 1.5: Opening and closing.....	23
Figure 1.6: Overview of difference densities observed for insertion studies (left) and protein binding partners (right).....	25
Figure 1.7: Binding partners containing EF hands.....	32
Figure 1.8: Crystal structures of RyR1A and RyR2A.....	35
Figure 1.9: The structure and docking of RyR1ABC.....	37
Figure 1.10: Structures of the RyR2A wildtype and exon 3 deletion mutant.....	38
Figure 1.11: Structure of RyR1 phosphorylation domain.....	40
Figure 1.12: Structural conservation between RyR and IP ₃ R.....	46
Figure 2.1: A linear view of RyR1 and RyR2 disease mutations.....	50
Figure 2.2: Pseudo-atomic models of RyR1ABC in open and closed RyR1.....	58
Figure 2.3: Relative positions between and within N-terminal disease hot spots.....	60
Figure 2.4: RyR1ABC docking results for different cryo-EM maps.....	61
Figure 2.5: Thermal melt analysis.....	64
Figure 2.6: Circular dichroic (CD) spectra of G216E.....	65
Figure 2.7: Buried disease mutations.....	66
Figure 2.8: Disease mutation affecting interdomain ionic pairs.....	68

Figure 2.9: Other mutations at the intrasubunit interfaces between different domains.	70
Figure 2.10: Domain reorientations are not due to pH differences.....	72
Figure 2.11: The clamping action of domain A.....	73
Figure 2.12: Model for the effect of N-terminal disease-associated mutations in RyRs and ligand binding in IP ₃ Rs.	76
Figure 3.1: The RyR2A HS-loop mutant structures.	85
Figure 3.2: The HS-loop of RyR2A wild type and A77V mutant.....	86
Figure 3.3: Chemical shift perturbations (CSPs) on RyR2A caused by the HS-loop mutants.	88
Figure 4.1: Overall structure of the RyR2 N-terminal region.....	98
Figure 4.2: Sequence alignment of RyR2 and RyR1 N-terminal regions.....	99
Figure 4.3: Details of the anion-binding site.	101
Figure 4.4: Structure of RyR2ABC crystallized in 4mM KCl.....	104
Figure 4.5: Structure of the R420Q disease-associated mutant.	106
Figure 4.6: Sequence alignment of various mammalian RyR2 sequences.	107
Figure 4.7: Additional RyR2 disease-associated mutants.....	110
Figure 4.8: The G230C mutation reduces the thermal stability of RyR2ABC.....	112
Figure 4.9: The structure and thermal stability of R414C.	114
Figure 4.10: PEG binding sites.	117
Figure 4.11: The structure of the β 22- β 23 loop at interface 1.	119

List of Abbreviations

4- <i>CmC</i>	4-chloro- <i>m</i> -cresol
ARVD2	Arrhythmogenic right ventricular dysplasia type 2
Ca ²⁺	Calcium (ion)
CaM	Calmodulin
CaMBD	Calmodulin-binding domain
Ca _v s	Voltage-gated Ca ²⁺ channels
CCD	Central core disease
CICR	Ca ²⁺ -induced-Ca ²⁺ release
CLIC-2	Chloride intracellular channel 2
CPVT	Catecholaminergic polymorphic ventricular tachycardia
Cryo-EM	Cryo-electron microscopy
Da (kDa/MDa)	Dalton (kilo-daltons/mega-daltons)
DLS	Dynamic light scattering
DR	Divergent region
E-C coupling	Excitation-contraction coupling
ER/SR	Endo/sarcoplasmic reticulum
FKBP	FK506-binding protein
FSC	Fourier shell correlation
GST	Glutathione- <i>S</i> -transferase
ITC	Isothermal titration calorimetry

IVF	Idiopathic ventricular fibrillation
IP ₃ R	Inositol-1,4,5-triphosphate receptor
IpTx _a	Imperatoxin A
K ⁺	Potassium (ion)
MH	Malignant hyperthermia
MmD	Multi-mini core disease
nm	Nanometer
PEG	Polyethylene glycol
PKA	Protein kinase A
PPS	Porcine stress syndrome
RDCs	Residual dipolar couplings
RMSD	Root mean square deviation
RyRs	Ryanodine receptors
SOICR	Store-overload-induced Ca ²⁺ release
WT	Wild type

Acknowledgements

I thank my supervisor, Dr. Filip Van Petegem, for his guidance and support in pursuing my doctoral thesis projects. I am grateful for the opportunities he has given me to develop my research skills. I also thank my committee members Dr. Edwin Moore and Dr. Franck Duong for their support.

None of the projects described in this thesis could have been tackled single-handedly. The success was possible due to the highly collaborative effort of the members of the Van Petegem lab. I especially thank Ching Chieh (Jett) Tung for his continued support throughout my doctoral studies. It was his dedication and superhuman bench-work skills combined with my supervisor's guidance that got many of our papers into prestigious journals. I also thank Paolo Lobo, the former Masters student, for helping me develop crucial techniques, including crystallography and thermofluor assays, as well as obtaining the preliminary results that provided us with a lot of insights. I thank the rest of the lab members, particularly Dr. Zhinguang (Michael) Yuchi for his mentorship and Kelvin Lau for answering all my computer-related questions, fixing everything from printer to ITC, and sharing the PhD-student life with me.

I also thank Dr. Wayne Chen (University of Calgary), Dr. Mitsu Ikura (University of Toronto), and their research teams for their collaboration in parts of the work presented in this thesis. In addition, my thanks go to Dr. Anna-Carin Carlsson (the Erdelyi Lab, University of Gothenburg) for her collaboration.

I owe special thanks to my family and my newly extended family, who have provided me with both emotional and financial well-being throughout my years of education.

Chapter 1: Introduction

Calcium ions (Ca^{2+}) are important intracellular messenger molecules in nearly every cell type of the human body. Under so-called “resting” states of the cell, the concentration of Ca^{2+} in the cytoplasm is extremely low ($\sim 10^{-7}\text{M}$), but this can rapidly rise ~ 2 orders of magnitude when an appropriate signal is generated. Ca^{2+} can enter the cytoplasm either from the extracellular space or from intracellular compartments through specialized membrane proteins. These “calcium channels” are complex proteins, often consisting of multiple subunits, and are targets for multiple regulatory events. The mobilization of Ca^{2+} from these organelles can trigger many Ca^{2+} -dependent events, such as the contraction of muscle tissue.

A major intracellular Ca^{2+} store is the endoplasmic reticulum (ER), or its specialized form, the sarcoplasmic reticulum (SR) in muscle tissue. There reside ryanodine receptors (RyRs), high-conductance Ca^{2+} -release channels responsible for releasing Ca^{2+} from the intracellular store into the cytoplasm (Figure 1.1). RyRs are involved in various physiological events such as learning and memory, secretion, fertilization, and apoptosis. Their most prominent role, however, is in the contraction of both cardiac and skeletal muscle.

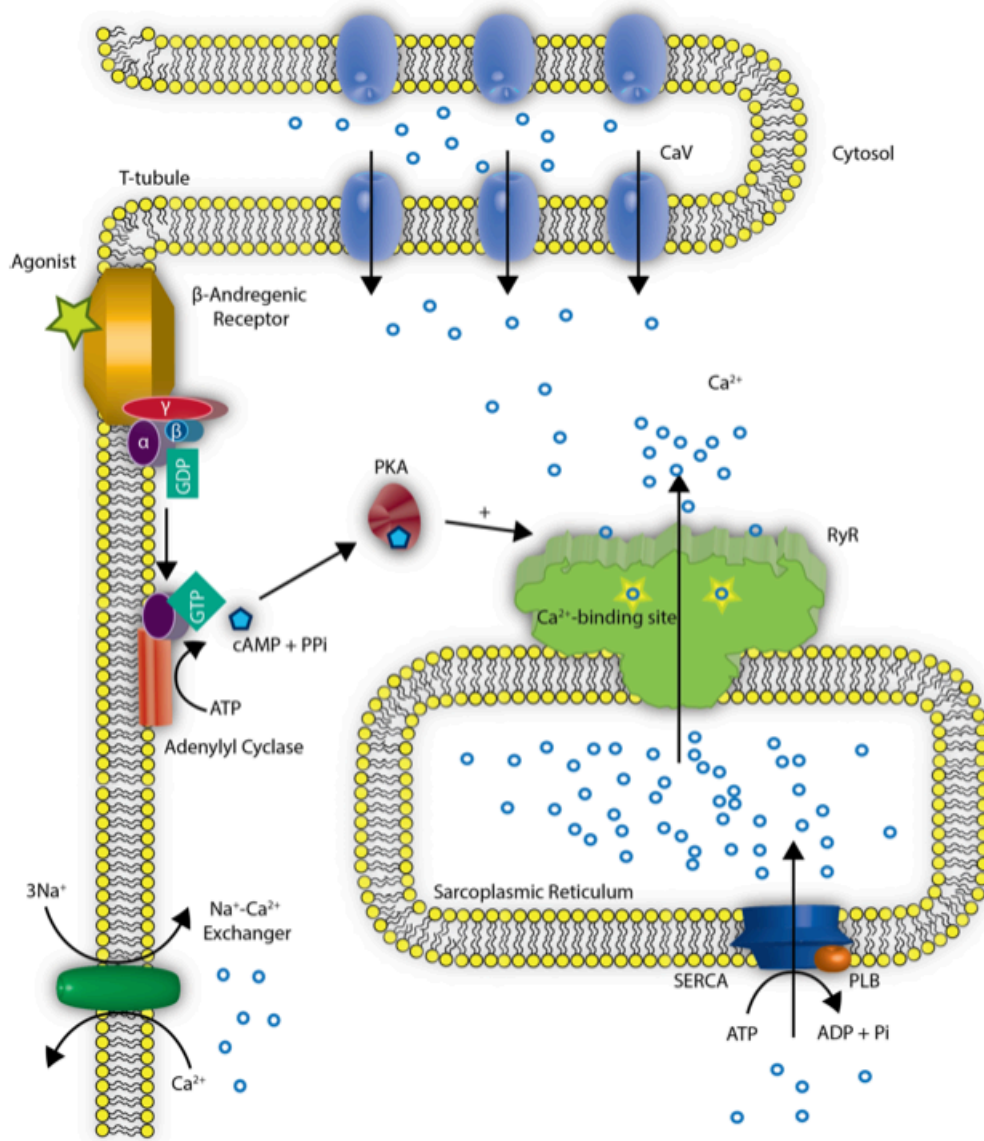


Figure 1.1: A schematic diagram of the components in E-C coupling. Depolarization of the plasma membrane activates the voltage-gated Ca^{2+} (Ca_V) channels, embedded in the T-tubule, which conduct Ca^{2+} influx into the cytoplasm. RyRs in the SR membrane sense this Ca^{2+} signal and amplify it by releasing more Ca^{2+} from the SR store (Ca^{2+} -induced Ca^{2+} release, CICR). This provides enough Ca^{2+} for the muscle contraction to occur. RyRs can also be activated through an overload of the luminal Ca^{2+} in a process known as store-overload-induced Ca^{2+} release (SOICR). SERCA pump in the SR membrane and $\text{Na}^+/\text{Ca}^{2+}$ -exchanger in the plasma membrane restore the resting $[\text{Ca}^{2+}]$. The activity of RyR can be upregulated by the PKA phosphorylation upon the activation of β -adrenergic receptor in the plasma membrane.

The naming of RyRs originates from the ability of the channel to bind the plant alkaloid ryanodine, a toxic compound from the South American plant *Ryania speciosa*(1). Ryanodine binds RyR at nanomolar affinity, which locks the channel in subconductance states at low concentrations and blocks them entirely at higher concentrations(2). RyRs are the largest ion channels currently known and form homotetrameric assemblies measuring approximately 2.3MDa (565kDa/subunit). In mammalian organisms three isoforms have been identified, encoded on different chromosomes. RyR1 is the predominant isoform in the skeletal muscle(3), while RyR2 is enriched in the heart(4). The third subtype (RyR3) was originally identified in the brain(5), but all three isoforms are expressed in multiple cell types. They share about 70% sequence identity, and the sequence variations mainly stem from three divergent regions in the *RYR* genes, referred to as DR1, DR2, and DR3(6).

RyRs are crucial in excitation-contraction (E-C) coupling (Figure 1.1). In myocytes, depolarization of the plasma membrane propagates through invaginations in the sarcolemma (transverse tubules, or T-tubules), where L-type voltage-gated Ca^{2+} channels (Ca_Vs) are located. The activation of these Ca_Vs by membrane depolarization stimulates RyRs in the SR. Thus, Ca_Vs act as the voltage sensors for RyRs(7-9). In the skeletal muscle, RyR1 and $\text{Ca}_V1.1$ interact directly(10,11), and this mechanical coupling is sufficient for the activation of RyR1. On the other hand, in the cardiac muscle, RyR2 is activated by the small influx of extracellular Ca^{2+} through Ca_Vs in a process known as Ca^{2+} -induced- Ca^{2+} release (CICR). In either case, the end result is a massive release of SR Ca^{2+} into the myoplasm through RyRs in response to membrane depolarization, leading to muscle contraction. RyRs, thus, act as the signal amplifiers, increasing the Ca^{2+} message originating from L-type Ca_Vs . The T-tubules and the SR form very close contacts (~12nm) in junctional sites(12). In the skeletal muscle, junctional sites are known as

triads, while they form dyads in cardiac myocytes(13). The proximity between the two membranes allows a rapid and precise communication between the voltage sensor and the signal amplifier.

Mutations in RyRs have been linked to severe disease phenotypes, reflecting their importance in the tight regulation of Ca^{2+} release during muscle contraction(14). More than 300 mutations have been identified in RyR1, and they are associated with malignant hyperthermia (MH)(15), central core disease (CCD), and several other conditions(16). In the cardiac isoform, more than 150 mutations have been linked to catecholaminergic polymorphic ventricular tachycardia (CPVT)(17) and arrhythmogenic right ventricular dysplasia type 2 (ARVD2)(18), two conditions that can lead to sudden cardiac death.

The RyR provides a platform for an abundance of small molecules and protein binding partners, and this is the likely reason for the enormous size of this protein(19)(20-24). The primary regulatory molecule is cytoplasmic Ca^{2+} , which triggers the channel to open. However, higher Ca^{2+} levels can trigger closing, indicating that there is more than one Ca^{2+} binding site: activation sites and inactivation sites. Under conditions whereby the SR is overloaded with Ca^{2+} , RyRs can also open spontaneously in a process known as store-overload-induced Ca^{2+} release (SOICR)(25,26). Some of the auxiliary proteins include, but are not limited to, calmodulin (CaM), FK506-binding proteins (FKBPs), calsequestrin, kinases (PKA, PKG, and CaMKII), and phosphatases (PP1, PP2A, and PDE4D3)(27). The size of this modulatory complex can be up to 7 MDa(20).

The presence of RyRs in the SR has been observed more than 40 years ago, long before their identification. In electron microscopic images, regularly spaced electron-dense protrusions were observed extending from the SR membrane and spanning the gap in the triads(28). Not

knowing the identity of these structures as the Ca^{2+} release channels at the time, these protrusions were later referred to as the “feet” structures(29). Since then, multiple studies have generated 3-dimensional structures of RyRs, which has provided a wealth of information on the molecular mechanisms underlying these complex channels.

1.1 Ryanodine receptors and genetic disease

RyRs are target for plethora of disease-associated mutations, highlighting their importance in the cellular processes and the need for their tight regulation. To date, more than 300 mutations have been identified in RyR1, and over 150 mutations have been found in RyR2. Although there may be a significant amount of sequencing bias(30), many mutations are found in three clusters or “hot spots” (Figure 1.2).

ABC (N-terminal 3 domains)

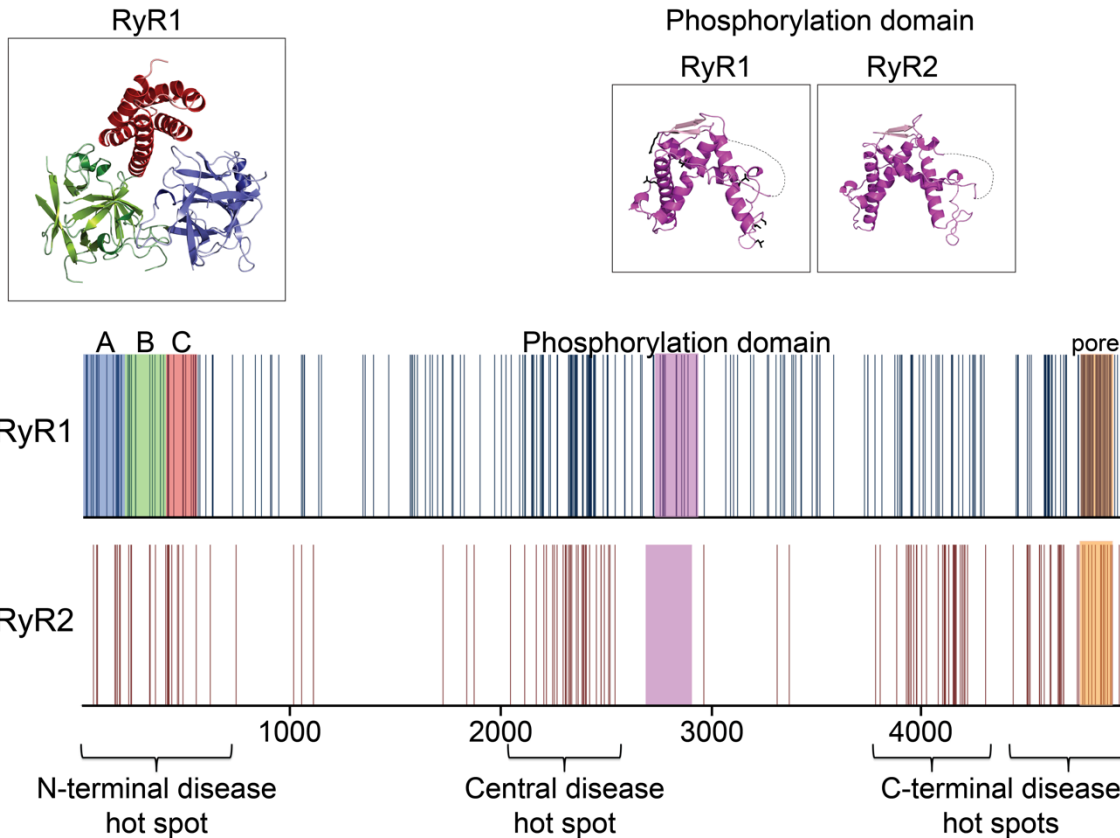


Figure 1.2: Disease hot spots. A linear view of the RyR1 and RyR2 amino-residue sequences, with each vertical line representing a disease mutation. The areas of solid colors correspond to domains A (blue), B (green), C (red), phosphorylation domain (purple), and pore-forming domain (orange). The available crystal structures are shown above the sequences: RyR1ABC (PDB accession code 2XOA) and RyR1 and RyR2 phosphorylation domains (PDB accession codes 4ERT and 4ETV, respectively).

1.1.1 Malignant hyperthermia

Malignant hyperthermia (MH) is a pharmacogenetic disorder, requiring both a genetic mutation and an external trigger to cause a disease phenotype. The condition is mostly linked to mutations in RyR1, but some mutations in the skeletal muscle L-type Ca^{2+} channel ($\text{Ca}_v1.1$) can also cause this disorder(31). It is typically triggered by the use of inhalational anesthetics or a

muscle relaxant, succinylcholine(32). The condition is considered rare, with an incidence of 1:60,000 for adults or 1:15,000 for children(33).

A MH episode is characterized by an abnormal rise in the core body temperature, skeletal muscle rigidity, acidosis, and tachycardia. Most modern surgery rooms monitor for these signs and will make use of dantrolene, which can rapidly reverse the symptoms. Dantrolene acts by decreasing the intracellular Ca^{2+} concentration(34). Several studies suggest a direct interaction between dantrolene and RyR1, and it is thought that dantrolene directly prevents Ca^{2+} release through RyR1(35,36), although some studies failed to observe any effect of dantrolene on purified RyR1, questioning the direct binding between the two(37).

The first link between MH and RyR1 came through a related disorder in pigs, known as porcine stress syndrome (PSS). It was found that the pig RyR1 mutation R615C underlies PSS(38), and soon after, the corresponding mutation in humans was linked to MH(15).

1.1.2 Core myopathies

Central core disease (CCD) is a congenital myopathy, characterized by progressive muscle weakness and the presence of metabolically inactive tissue (or cores) in the center of muscle fibers. These cores lack mitochondria, and the myofibrillar organization is disrupted. The common phenotype of CCD includes muscle atrophy, floppy infant syndrome, and skeletal muscle deformities(39,40). It was established early on that there is a connection between CCD and MH susceptibility(41), and some RyR1 mutations have been found to cause both(40).

Multi-mini core disease (MmD) is another inherited congenital myopathy. Unlike CCD, whose inheritance is autosomal dominant, MmD is usually considered recessive(39). As its name suggests, MmD is characterized by the presence of multiple ill-defined cores in muscle fibers. MmD can cause axial muscle weakness that can lead to severe scoliosis(39). Although MmD is

mainly associated with mutations in RyR1(42), mutations in selenoprotein N1(43), a protein required for RyR1 Ca^{2+} release(44), and α -actin (ACTA1) have also been found to underlie MmD(45).

1.1.3 Catecholaminergic polymorphic ventricular tachycardia

Also known as CPVT, this disorder manifests itself in young individuals, with either syncope or sudden cardiac death as the first symptom. Many affected individuals will develop cardiac arrhythmias that are triggered by physical exercise or emotional stress. CPVT is mostly detected through stress tests, which indicate bidirectional ventricular tachycardia. Typically no morphological abnormalities of the myocardium are detected. The disease is mostly due to mutations in the cardiac RyR2 isoform(17), but mutations in the associated proteins calsequestrin(46), triadin(47), and CaM(48) can also be the cause.

As CPVT is triggered by β -adrenergic stimulation, it can be treated by β -blockers(49). Flecainide, a sodium channel blocker, has also been found to be beneficial for CPVT patients(50).

1.2 Functional studies of RyRs

Although increasing numbers of RyR mutations are identified in patients and their family members, only a handful of them have been validated as causative disease mutations(33). Functional studies are necessary to prove the molecular basis of the mutations as pathogenic, and without such characterizations, the possibility that some of the mutations are the result of polymorphism cannot be ruled out. Moreover, functional studies provide a number of clues on how the mutations affect the channel function. For example, do the mutations facilitate channel opening or do they inhibit the channels? Do the mutations affect the channel sensitivity towards

cytosolic modulators or luminal modulators? In this section, different methods of performing functional studies and their results are highlighted.

1.2.1 Model systems

Variety of model systems for studying the functional effects of RyRs, in physiological and pathogenic states, have been developed over the years. These can be roughly divided into three groups: endogenous and recombinant expression systems and *in vivo* models.

1.2.1.1 Native expression systems

In the early days, before and shortly after the discovery of RyR1 mutations in MH-susceptible pigs and individuals, SR vesicles were prepared from muscle biopsies(51,52). SR vesicles from non-MH-susceptible animals or individuals were also obtained to serve as controls. These are endogenous expression systems since SR vesicles contain native RyRs. SR vesicles can be used as a whole or can be further purified to obtain individual RyR channels.

SR vesicles prepared from biopsies are invasive, since they involve acquisition of native RyRs expressed in patients or knock-in mice carrying mutations. For example, skeletal myotubes have been isolated from MH-susceptible and/or CCD patients(53-56). Both RyR1 and RyR2 can be studied by isolating skeletal myotubes and cardiomyocytes from knock-in mice, respectively(57-59). Flexor digitorum brevis fibers, present in the feet, have also been derived from knock-in mice for the study of RyR1 mutations(60-63).

In some cases, measures have been taken to alleviate some of the affliction on obtaining native RyRs from patients by using less invasive approaches. In one study of a CCD-associated mutation, fibroblasts from a CCD patient were differentiated into muscle by myoD conversion with adenovirus(64). In other cases, immortalized lymphoblastoid cells were generated using B-lymphocytes isolated from blood samples(65,66).

1.2.1.2 Recombinant expression systems

A more commonly used model is a recombinant expression system. By using cells that lack the native expression of RyRs, all results will arise only from the mutant RyRs. One of the most well-used systems are dyspedic myotubes, which are derived from mice that lack RyR1, or RyR1-null mice(67-70).

Also frequently used are human embryonic kidney (HEK)-293 cells. HEK-293 cells not only lack native RyR expression but also lack other components involved in E-C coupling. Yet HEK cells have been demonstrated to express functional channels when they are transfected with RyR cDNA(71-76). Other cell lines used in functional studies include COS-7(77), myoblastic C₂C₁₂(78), HL-1 cardiomyocytes(79,80), and CHO cells(81).

1.2.1.3 *In vivo* systems

Knock-in mice have served as valuable models for functional studies of mutations in RyR1 and RyR2(57-59,82,83). The comparison between mice that are homozygous or heterozygous for the mutation in question has provided clues about the gene dosage effects in different disorders. Studying the effect of mutations on the body as a whole provides insights that are more relevant to clinical phenotypes, such as mutational effects on multiple organs.

1.2.2 Methods

Multiple techniques have been implemented to characterize mutant RyRs in different expression systems. Four commonly used methods are briefly introduced here.

1.2.2.1 [⁴⁵Ca²⁺]-uptake and release assays

One way to measure Ca²⁺ release through RyRs is via [⁴⁵Ca²⁺]-uptake and release assays(84-86). Microsomal vesicles expressing recombinant RyR and SERCA1a are prepared. SERCA1a (sarco/endoplasmic reticulum Ca²⁺-ATPase) is a Ca²⁺ ATPase that pumps back Ca²⁺

from cytosol into the SR/ER lumen. The vesicles are then incubated with [$^{45}\text{Ca}^{2+}$], during which SERCA1a drives [$^{45}\text{Ca}^{2+}$] into the vesicles. By comparing the amount of [$^{45}\text{Ca}^{2+}$] accumulation in the presence or absence of the potent RyR inhibitor Ruthenium Red, the amount of Ca^{2+} release through RyR can be determined.

1.2.2.2 Whole-cell Ca^{2+} fluorescence assays

A more widely used technique is a Ca^{2+} fluorescence assay involving whole cell samples(71-73,75,77,78,87). Cells, usually HEK-293 with recombinant expression of RyR, are loaded with a fluorescent Ca^{2+} indicator, such as fura-2, which diffuses throughout the cytoplasm. By measuring fluorescence with confocal microscopy, the resting [Ca^{2+}] levels in the cytoplasm, as well as the frequency, duration, and extent of Ca^{2+} release from RyR can be calculated. The addition of caffeine to the cell leads to the depletion of the Ca^{2+} store in the ER through RyR, and in this way, the [Ca^{2+}] levels in the ER can also be measured.

1.2.2.3 [^3H]-ryanodine binding assays

Also commonly used is a [^3H]-ryanodine binding assay(72,73,75,76,88,89). SR vesicles containing endogenous or recombinant RyR are incubated with ryanodine containing the radioactive isotope of hydrogen: [^3H]-ryanodine. Since ryanodine binds to RyR in the open state, binding of [^3H]-ryanodine is indicative of the measure of open channels. The extent of RyR activation is then measured by radioactive counting on the [^3H]-ryanodine bound to RyR at the end of the experiment.

1.2.2.4 Single-channel electrophysiology

As opposed to whole-cell measurements, activities of a single channel can be recorded using planar lipid bilayer electrophysiology(66,87,89,90). Recombinant or endogenous RyR from crude SR vesicle preparations or from purified material are fused into an artificial lipid

bilayer formed across two chambers. The current generated by ions passing through the channel is then recorded. This method allows various properties of the single channel to be determined, including the open probability, duration of the open and closed time, and conductance. The two chambers can resemble cytoplasmic and luminal sides of the channel, allowing the studies of Ca^{2+} -induced Ca^{2+} release (CICR) from the cytoplasmic side or store-overload-induced Ca^{2+} release (SOICR) from the luminal side. The planar lipid bilayer technique also allows for additional control because purified auxiliary proteins or pharmacological modulators can be added to either side of the chambers.

1.2.3 Highlights of the results

Functional studies of mutant RyR channels have generated numerous insights into the molecular basis of the RyR channelopathies. Accordingly, complex sets of results have been generated that require careful interpretation and have resulted in debates. For example, many mutations seem to make RyRs more active, but the exact nature of this change is still under scrutiny. In some cases, mutations seem to be more sensitive to cytosolic activators, while other evidence suggests they are more sensitive to luminal Ca^{2+} levels. Others suggest that altered phosphorylation states of the channel or affinity to auxiliary proteins are the causative mechanism. In this section, results of the functional studies are highlighted as mutations that cause RyRs to be either hypersensitive (more prone to opening upon stimulation) or hyposensitive (requiring more stimulus to open). RyR mutations can be pathogenic either through gain or loss of function since alteration in Ca^{2+} homeostasis in either direction can cause aberrant muscle functions. Yet other mutations have exhibited no apparent alterations in the functional studies performed so far. The results are summarized in Appendix A.

1.2.3.1 Gain-of-function mutations

The majority of the mutations in both RyR1 and RyR2 have been shown to make the channels hyperactive. This includes the first disease-associated mutation found in porcine stress syndrome, RyR1 R615C. Functional studies have revealed that RyR1 channels with this mutation have significantly lowered threshold for activation by Ca^{2+} , caffeine, and halothane compared to wild-type channels, while having markedly increased threshold for inactivation by Ca^{2+} , Ruthenium Red, or Mg^{2+} (51,52,77,78,84,85,88,91-93). These results are characteristic of gain-of-function mutations that alter RyRs into hypersensitive channels. RyRs that are hyperactive are often described as “leaky,” and in addition to their increased sensitivity towards activators or reduced sensitivity towards inhibitors, they often exhibit increased resting $[\text{Ca}^{2+}]$ levels in the cytoplasm, reduced SR Ca^{2+} store content, or altered maximal Ca^{2+} release.

1.2.3.2 Loss-of-function mutations

Although less common, some mutations in RyRs have been demonstrated to reduce channel activity. For example, I4898T mutation in the transmembrane region of RyR1, associated with an unusually severe and highly penetrant form of CCD, has been shown to cause complete uncoupling of sarcolemmal excitation from SR Ca^{2+} release, in which activating signals from L-type Ca_v channels to RyR1 are uncoupled(67). Mutations that disrupt signaling between $\text{Ca}_v1.1$ and RyR1 are known as “E-C uncoupling” mutations. It has also been shown that the I4898T mutation leads to a complete loss of Ca^{2+} release induced by caffeine stimulation(94). Many other CCD-associated mutations located at the predicted pore region of RyR1 (G4890R, R4892W, A4894P, I4897T, G4898R, G4898E, and R4913G) have also been shown to abolish E-C coupling and/or exhibit reduced sensitivity to activation by Ca^{2+} , caffeine, or 4-CmC(70,86,95-98).

In RyR2, fewer mutations thus far have been associated with a reduction in activity, suggesting that a loss of function in RyR2 may be less tolerated than in RyR1. A4860G mutation in RyR2 is associated with idiopathic ventricular fibrillation (IVF) and is located at the predicted inner pore helix. It has been shown to diminish response or increase the threshold for activation by SOICR(99,100). Furthermore, RyR2 A1107M mutation in mice (corresponding to T1107M mutation in humans, associated with hypertrophic cardiomyopathy) has been shown to increase the threshold for Ca^{2+} release termination(101,102).

1.2.3.3 Mutations with no discernible functional change

Effects of some disease-associated mutations are less apparent. For instance, single channel measurements of RyR1 A1577T and G2060C mutants produced no discernible change in the activity of the channels compared to that of the wild type(103). Similarly, [^3H]-ryanodine binding assays of RyR1 R2939K expressed in HEK-293 cells failed to show alteration in Ca^{2+} -dependent and caffeine-induced activation compared with wild-type channel(104). RyR1 I404M expressed in dyspedic mice myotubes exhibited resting [Ca^{2+}] levels and SR [Ca^{2+}] content comparable to that of the wild type(68). Furthermore, expressions of RyR1 D3987A and G3939A rabbit cDNA (corresponding to MH-associated mutations D3986E and G3938D in humans, respectively) in HEK-293 cells only showed responses to activation by Ca^{2+} , caffeine, and 4-CmC comparable to that of the wild type(72,75).

For those mutations where no clear functional effect has been observed, it is possible that they are not causative of disease but, instead, simply represent polymorphisms. Alternatively, their effect may only become apparent in the native environment, where particular regulatory mechanisms exist that are not captured by the model systems.

1.2.3.4 Remark on functional studies

Overall, there is an apparent theme between RyR activity and disease phenotype. MH and CPVT are associated with RyR mutations that give an overall gain-of-function phenotype. On the other hand, CCD can be due to either a gain or a loss of RyR1 activity. Loss of function results in impaired Ca^{2+} release and, hence, decreased contractility observed in CCD. The gain of RyR1 activity can lead to a general “leak” of Ca^{2+} , resulting in an overall lowered concentration of Ca^{2+} in the SR. The result is then an insufficient amount of Ca^{2+} being available for an E-C coupling event, again resulting in decreased contractility.

For those mutations with less clear effects, as well as those which have been shown to be causative for aberrant Ca^{2+} homeostasis, combining functional studies with structural investigations would provide further useful insights into the molecular basis of disease-associated mutations in RyRs.

1.3 Structural studies of RyRs

Knowing the atomic details of a macromolecular assembly greatly enhances our insights into a particular protein. Unfortunately, RyRs present major challenges to techniques such as X-ray crystallography because of the enormous size, the integral membrane protein nature, and dynamic features that result in a heterogeneity of functional states. For this reason, electron microscopy of single particles and two-dimensional crystals has been the primary method of choice in the field for many years. In the recent years, however, NMR and crystal structures of several segments of RyRs have started to emerge. These atomic-resolution structures provide details that are key to understanding the molecular mechanisms of the channel function in normal and diseased states.

1.3.1 Cryo-EM studies of closed RyRs

The presence of junctional “feet” structures has been observed almost half a century ago in thin-section or negative stain electron microscopic images. In these studies, images captured square-shaped, electron-dense protrusions from the SR membrane from both native muscle tissues and isolated SR vesicles. For a limited set of examples, see references(10,28,29,105,106). The feet were shown to be composed of four subunits(107), and their identity was confirmed when the electron microscopic images of purified RyRs were able to show the characteristic “feet” structures(108).

An intriguing property of RyRs is their ability to form two-dimensional arrays. It was observed in native tissue preparations that skeletal muscle RyRs form checkerboard-like lattices, touching the neighboring molecules near the corners(12,107,109).

It was later found that this is an intrinsic property, as purified RyR1 was able to assemble into similar patterns and could form two-dimensional crystals(110,111). In the skeletal muscle preparations, tetrads of Ca_v s were found to coincide with the cytoplasmic region of RyR1 in an alternating fashion. This strongly suggested that the two membrane proteins, each being part of a different membrane, physically interact(10). The functional implications of the clustering and RyR- Ca_v interaction will not be discussed here but are reviewed elsewhere(7,14,22).

Numerous efforts have been made to improve the structural details of RyRs in the electron micrographs. Due to its high abundance in the SR membrane and the relative ease of purification, the RyR1 structure has been the most intensively studied. One group obtained a 37Å-resolution structure of RyR1 by generating computer-averaged images from multiple negative stain images(109,112). The resolution was further improved to ~30Å by the use of frozen-hydrated sample preparations in cryo-electron microscopy (cryo-EM)(102,113,114). By

this time, enough details were present to identify globular-shaped domains in the cytoplasmic region of the channel. Further description was given to the RyR structure: regions found at the corners were termed “clamps” as they resembled the shapes of laboratory clamps, whereas the regions that connected these corners were termed “handles”(114)(Figure 1.3).

Comparison between the structures of the three isoforms showed that the overall features are universal among subtypes, which is not surprising given their high sequence homology(115-118). The most striking trait of the RyR is its mushroom shape, composed of two parts: a larger cytoplasmic region forming the cap (~80%) (previously known as the “foot” structure) and a smaller transmembrane region forming the stem (~20%). Both form square prisms that are rotated by ~40° relative to one another, and which are connected via four thick columns ~14Å long. The transmembrane region measures 120 x 120 x 60Å³, whereas the cytoplasmic foot measures approximately 270 x 270 x 100Å³. The latter portion contains numerous globular masses and a series of cavities in which more than 50% of its volume is occupied by solvent. Fifteen globular subregions have been identified so far and arbitrarily assigned numerical labels. Based on segmentation of the highest resolution map(119,120)(Figure 1.3), these subregions can be divided into four units: (i) clamps at each corner (subregions 5, 6, 7a, 7b, 8a, 8b, 9, and 10); (ii) handles connecting two clamp regions (subregions 3 and 4); (iii) a central rim on the cytoplasmic face around the fourfold symmetry axis (subregions 1, 2a, and 2b); and (iv) columns (subregions 11 and 12) that connect the cytoplasmic and transmembrane regions. Some of the subregions have received alternative labeling(121) (Figure 1.3, brackets). The subunit boundary between each monomer was proposed to center around the handle region, containing one whole handle, two halves of the clamp regions on either side, and a quarter of the central rim(120), although there are some discrepancies (see Section 1.3.6.2 and Chapter 2).

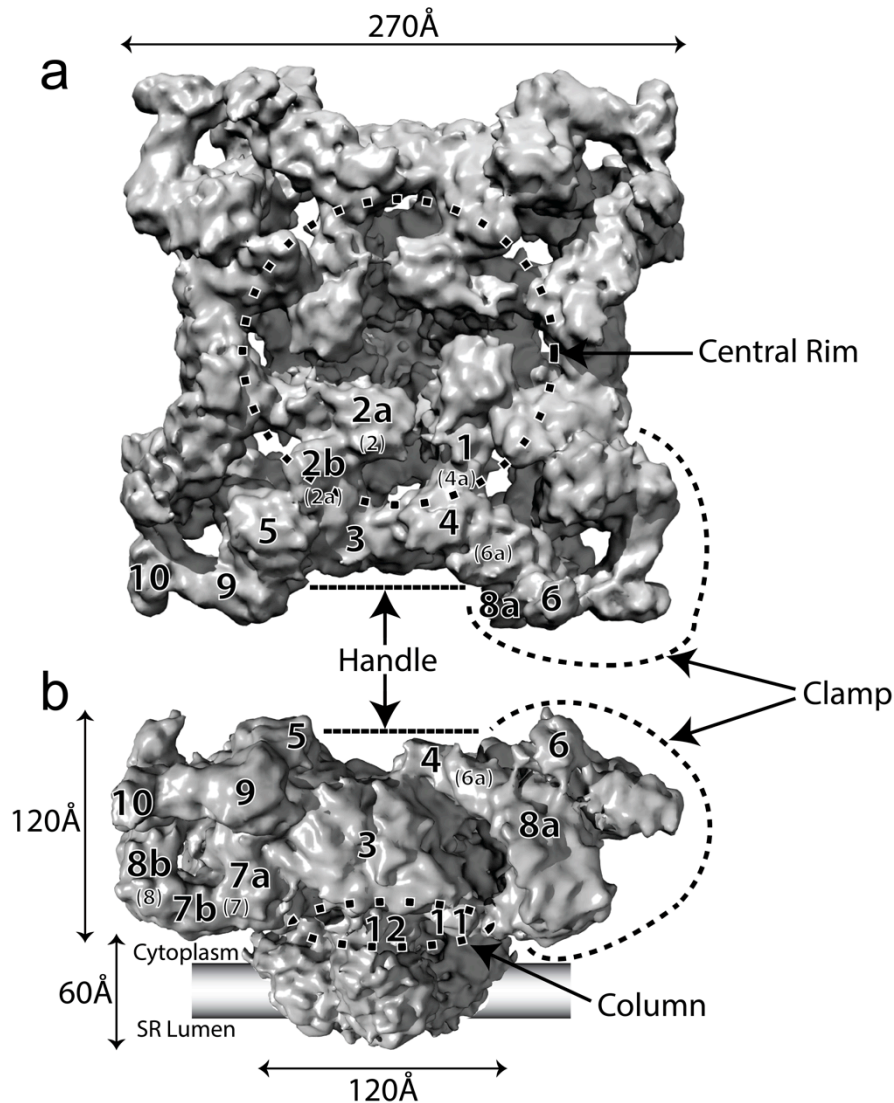


Figure 1.3: An overall structure of RyR. The $\sim 10\text{\AA}$ cryo-EM reconstruction (EMDB accession code 1275) of RyR1 in the closed state. **(a)** Top view from the cytoplasm facing the SR and **(b)** side view from the plane of the SR membrane. Subregions are labeled according to Serysheva *et al.* (120), with respective alternate labeling according to Samso *et al.* (121) shown in brackets.

The major difference between RyR1 and RyR2 seems to be located in the clamp region, where some masses were found to be either larger or smaller in RyR2 than in RyR1 (115). Similarly, comparison between RyR1 and RyR3 has revealed an extra mass in RyR1 that is

missing in RyR3(118). These structural differences likely contribute to distinct functional properties among the three isoforms.

A key question surrounding RyR structure is the transmembrane region. How many helices are present, and what is the architecture of the pore-forming part? In order to analyze the transmembrane assembly, the quality and resolution of the maps are of key importance. Two groups have described the structures of closed RyR1 at resolutions near 1nm, with reported resolutions of 10.2-10.3Å(121,122) and 9.6Å(119). It is noteworthy that both studies used different criteria to report the resolution (Fourier shell correlation or FSC cutoff 0.15 versus 0.5, respectively), adding to the debate of which criterion should be used(123-125). A recent discussion on the validation estimates the highest resolution of RyR cryo-EM reconstructions to fall between ~10Å to ~12Å(126).

The highest resolution currently available for any full-length RyR is at ~10Å for the closed state of RyR1(119,126). At this resolution, five putative membrane-spanning α helices in each subunit could be assigned inside rod-like densities. However, there are likely more secondary structure elements, and it has been suggested that each subunit contains 6 or 8 transmembrane helices(127). Two out of the five putative helices (simply named helices 1 and 2) are located near the 4-fold central axis and resemble the pore-lining and pore helix structures observed in K⁺ channels (Figure 1.4). Helix 1 is about 45Å long and is kinked, bending away from the 4-fold symmetry axis. At the SR luminal side, helices 1 from each subunit together form a large, funnel-like cavity with a diameter of approximately 30Å, which likely forms the channel entrance. The funnel tapers towards the SR membrane, and the narrowest part measures about 15Å in diameter. Helix 1 is the likely candidate for the inner, pore-lining helix. Helix 2 is shorter (~22Å) and is tilted about 50° with respect to the plane of the SR membrane. Helices 2

from each subunit point towards the 4-fold central axis to form an opening of $\sim 7\text{\AA}$ and are, therefore, prime candidates for the pore helices. Putative helices 3, 4, and 5 have lengths of about 18-22 \AA .

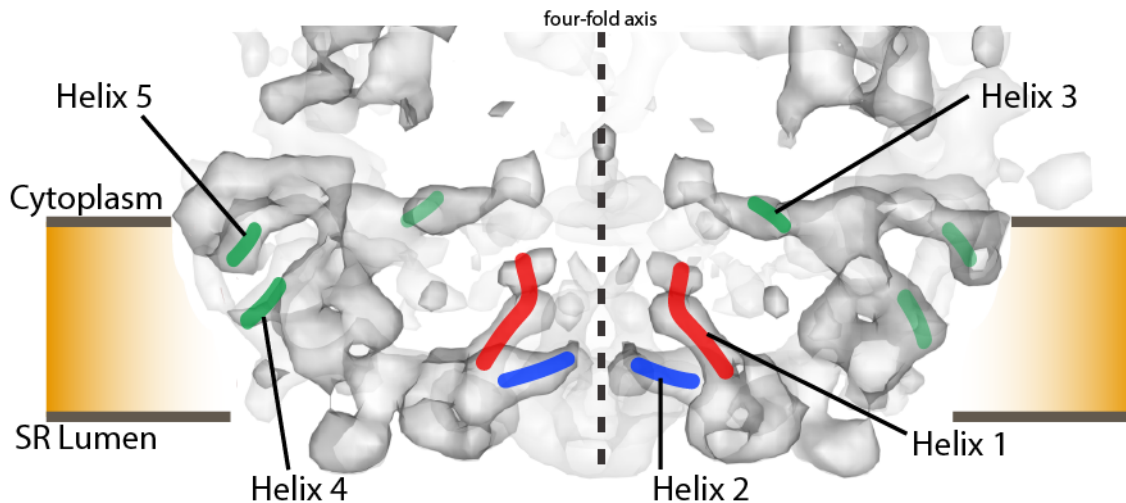


Figure 1.4: The pore-forming region. A close-up of the transmembrane region of the $\sim 10\text{\AA}$ closed RyR1 cryo-EM map from the side view. The putative helices are outlined. The surrounding densities are clipped for clarity.

Because crystal structures are now available for the pore region of several K^+ channels, the helical arrangement can be compared directly with the presumed pore-forming region in the cryo-EM reconstructions. Although the $\sim 10\text{\AA}$ cryo-EM reconstruction is thought to represent RyR1 in the closed state, helices 1 and 2 only poorly match the helices of the closed KcsA K^+ channel structure(128). Instead, a higher correlation was found for MthK channel in the open conformation. Kinking of the inner helices in MthK channel is thought to open this channel(129). Since helix 1 appears to be bent already, kinking of the inner helices in RyRs is likely not sufficient for channel opening(119). A proposed model places a highly conserved glycine (Gly4934) at the hinge position of the inner helix and two rings of negative charges at the luminal and cytoplasmic opening of the pore. Such a charge distribution is commonly observed in cation-selective channels. For a limited set of examples, see references(128,130-134).

In contrast with this, different conclusions have been reported by Samsó and colleagues. In two RyR1 structures in the closed state at reported resolutions 10.2-10.3Å (FSC 0.15 cutoff), manual docking showed a higher correlation between the closed RyR1 and closed KcsA or KirBac1.1 channels(121,122,128,135). Therefore, there are discrepancies in the shape of the transmembrane helices and in the interpretations of possible modes of channel gating. These may be due to overall differences in the conformational purity of the samples, or simply due to differences in resolution (~4Å of difference when the FSC 0.5 criterion is applied to all studies). As the structures originated from detergent-solubilized preparations, it cannot be excluded that there are differences depending on sample handling.

More recently, a feature detection program was used to identify secondary structures in the cytoplasmic region using the ~10Å structure of RyR1(120,136). The authors identified 36 putative α helices and seven putative β sheets in the cytoplasmic foot. In particular, one putative β sheet is located at subregion 12, near the tapered section of the “column” region. This β sheet may play an important role in the gating of the channel since other channels, including Kir and HCN2, share β sheets at the same location(135,137-140).

1.3.2 Opening and closing

Being such a large protein, it is conceivable that opening and closing of the channel is allosterically coupled to the large cytoplasmic foot region. The first open structure of RyR was obtained by Orlova and colleagues at 30Å resolution(141), followed by more structures in the subsequent years(118,122,142). In these studies, the open conformation of RyR was stabilized by the presence of Ca^{2+} and other modulators, such as ryanodine, PCB95, and ATP homologs.

The studies all agree that the closed and open RyRs share similar overall structures. One obvious difference is a widening of the central pore upon opening. The authors also reported

global conformational changes between the two states, especially in the clamps and the transmembrane region. Since structural changes occur far away from the proposed pore region, RyRs are clearly allosteric proteins, and interference with any of the movements is likely to affect channel function.

The highest resolution available for the open-state RyR thus far is at reported 10.2Å (FSC 0.143 cutoff) for RyR1(122). The authors used PCB95, a neuroactive compound, to stabilize the open state. The largest conformational changes were found in the cytoplasmic foot. In the open conformation, subregions 7, 8, 9, and 10 in the clamp move down towards the SR membrane by ~8Å, while subregion 6 moves outwards by ~5Å (Figure 1.5). In addition, subregion 2 in the central rim moves upward towards the T-tubule and outwards away from the 4-fold central axis. Thus, the main conformational change in the cytoplasmic portion upon opening of the channel is an outward movement away from the center.

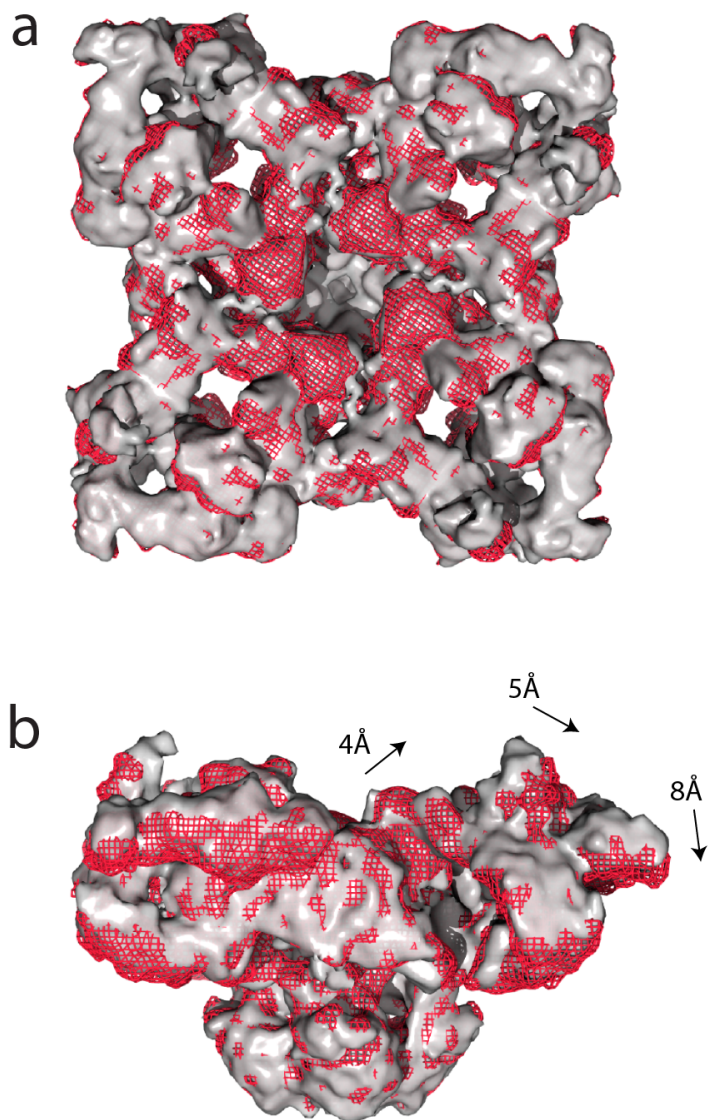


Figure 1.5: Opening and closing. (a) Top and (b) side views of superpositions of the cryo-EM reconstructions of RyR1 in closed (gray, EMDDB accession code 1606) and open (red mesh, EMDDB accession code 1607) states. The extent of some conformational changes is indicated by arrows.

Another large structural change was observed in the transmembrane region. The authors identified at least six membrane-spanning α helices per subunit, based on the number of high-density segments in the transmembrane region. Upon opening, the inner helices seem to kink, as the bottom halves shift 3\AA upward towards the cytoplasmic side, and tilt $\sim 5^\circ$, widening the pore.

This observation is consistent with other studies that reported rotating motions in the transmembrane region and compared the opening and closing of RyR to that of a camera aperture(118,141,142). The motions in the cytoplasmic and transmembrane regions seem to be coupled via the column region, in particular the inner branches, which tilt by $\sim 8^\circ$ upon opening, moving their midpoints $\sim 6\text{\AA}$ away from one another(122).

Manual docking of K^+ channel structures in the open-state map showed that the open RyR1 correlates better with open K^+ channels(122). However, since there have been inconsistent results for correlation between closed RyR1 and K^+ channel structures(119,121,122), care must be taken when interpreting these manual docking results. Although buffer conditions can favor an open or closed state in intact membranes, this does not necessarily extrapolate to conditions following detergent extraction. As differences in sample handling may also contribute to structural changes, the conformational state is best deduced by analyzing the final model rather than assuming a particular state. The discrepancies would be reconciled, for example, if the $\sim 10\text{\AA}$ RyR1 structure(119) represents an open or partially open (*i.e.* subconducting) channel, rather than a fully closed structure. Future experiments will undoubtedly shed more light on this matter.

1.3.3 Insertion studies

Despite the continued improvements into the quality of full-length RyR structures, the cryo-EM reconstructions are of insufficient resolution to locate individual amino acids. In the absence of atomic models, one alternative is to determine the rough location of regions of interest via the use of antibodies or fusion proteins. In both cases, analysis of the difference densities found in cryo-EM reconstructions puts restraints on the position of the insertion site or the antibody epitope. The residual uncertainties of the locations depend on the resolution, the

size of the insert or antibody, and the lengths of flexible linkers and loops at the insertion site. The locations proposed in many of these studies are summarized in Figure 1.6.

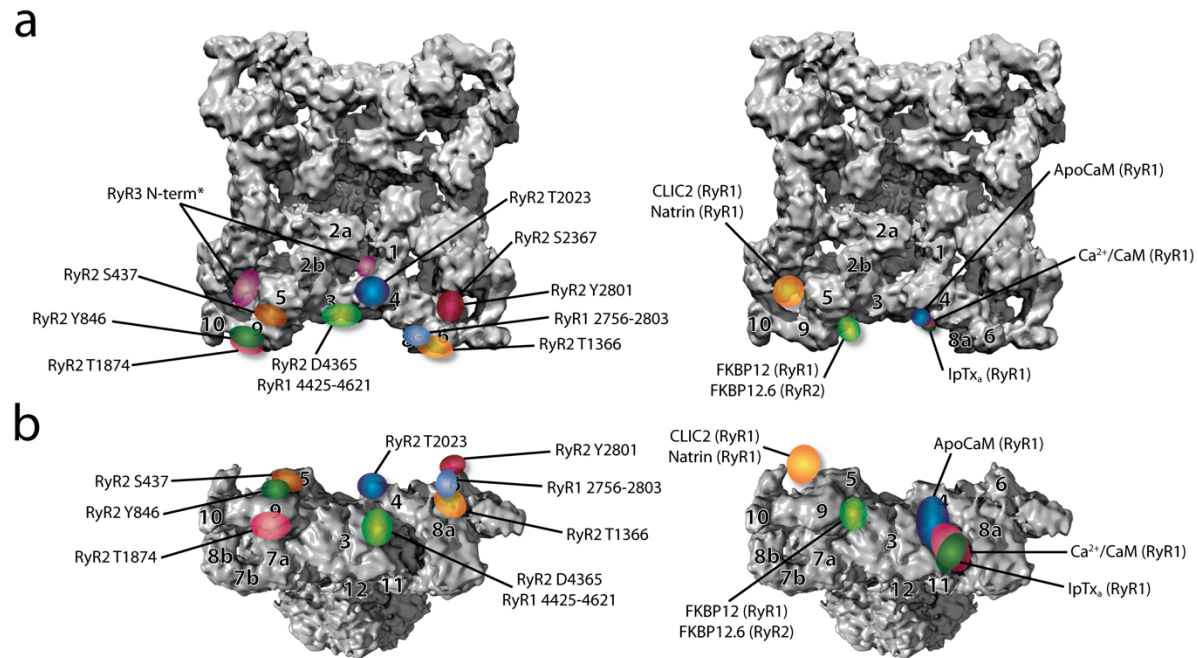


Figure 1.6: Overview of difference densities observed for insertion studies (left) and protein binding partners (right). (a) Top and (b) side views of the cryo-EM reconstruction of RyR1, with observed difference densities indicated in spheres. Although the studies were performed on different RyR isoforms, all are shown here on the RyR1 cryo-EM map to allow a direct comparison.

1.3.3.1 N-terminal region

The three-dimensional localization of the amino terminus of RyR has been of great interest since the N-terminal region (residues 1-614 in RyR1) covers the first of the three hot spots for disease mutations. (See also Section 1.3.5.2.) The 34Å cryo-EM reconstruction of RyR3, N-terminally fused to GST (GST-RyR3), displays an extra mass at the clamp region in the middle of subregions 7-10 and a smaller extra mass between subregions 1, 3, and 4(143). A 33Å structure of RyR2 with GFP inserted after Ser437 presented additional density between subregions 5 and 9(144). These studies led the authors to conclude that the N-terminal disease

hot spot was most likely located in the clamp region. We will go over the location of the N-terminal region in greater detail in Section 1.3.6.2 and Chapter 2, showing that the region is found in the central rim rather than in the clamp region.

Another site of interest in the N-terminal region is residues 590-609 in RyR1 and residues 601-620 in RyR2 which constitute the proposed binding site for dantrolene(35,145). Dantrolene is the only effective treatment for malignant hyperthermia, thus knowing the exact location of its binding site is of considerable interest. Insertions of GFP in the binding site did not yield any well-behaved protein, but the 27Å structure of RyR2 with GFP inserted after Tyr846 showed a major extra mass on the T-tubule side of subregion 9. Along with FRET studies, it was concluded that dantrolene also binds close to subregion 9, near the binding site for FKBP12(146).

1.3.3.2 Central region

The central region (residues 2163-2458 in RyR1) harbors another disease-mutation hot spot. Insertion of GFP near RyR2 Ser2367 showed a significant extra mass in the bridging density between subregions 5 and 6(147). This experiment suggests that it is possible for the N-terminal and central disease hot spots to interact, supporting the zipper hypothesis, which states that the two regions interact and undergo relative conformational changes upon channel opening(148).

A recent study showed that the clamp region of RyR2 under go conformational changes in ligand-dependent manner(149). The study utilized CFP insertion at Ser2367 and YFP insertion at Tyr2801, for which FRET signal was identified in subregion 6 of the clamp region. Conformational changes in the region were detected for activators caffeine, aminophylline, theophylline, ATP, and ryanodine. However, the presence of Ca^{2+} or 4-CmC, despite also being

an agonist, did not induce detectable conformational changes in the clamp region. The authors suggest that RyRs possess multiple ligand-dependent activation mechanisms, each accompanied by distinct conformational changes in the clamp region(149).

1.3.3.3 Divergent regions

The three RyR isoforms share about 70% identity, and the major sequence differences are located in three stretches known as divergent regions DR1, DR2, and DR3(6). These stretches likely underlie functional differences between the isoforms, and, therefore, their three-dimensional location is valuable for understanding the functional mechanisms in RyRs.

DR1 is the largest of the three divergent regions and includes residues 4254-4631 in RyR1 and residues 4210-4562 in RyR2. This region is thought to be responsible for the varying sensitivities towards Ca^{2+} inactivation in different isoforms(150-152). One study took advantage of a monoclonal antibody raised against residues 4425-4621(153). The 34Å structure of RyR1 in complex with the antibody showed an extra mass in subregion 3. In agreement with this observation, an extra mass was observed in the same area after inserting GFP at Asp4365(154).

The second divergent region, DR2, includes residues 1342-1403 in RyR1 and residues 1353-1397 in RyR2. This region is thought to be involved in E-C coupling(155,156). DR2 is absent in RyR3(6). Negative stain electron micrographs of RyR1 in presence of an antibody against DR2 revealed an extra density in the clamp, close to subregion 9(117). Consistent with the result, an extra mass appeared in the neighboring subregion 6 in a 34Å structure of RyR2 with GFP inserted after Thr1366(157).

DR3 includes residues 1872-1923 in RyR1 and residues 1852-1890 in RyR2. This region has been implicated in modulation by $\text{Ca}_v1.1$, Ca^{2+} , and FKBP(158-160), and is the target for

some disease-associated mutations(161). Insertion of GFP after RyR2 Thr1874 leads to an extra density in subregion 9, close to the proposed FKBP12.6 binding site(162).

1.3.3.4 Phosphorylation sites in the central region

RyRs are the target for phosphorylation by protein kinase A (PKA), which is known to activate the channels(163,164). Both Ser2030 and Ser2808 are PKA phosphorylation sites(165-167). The 27Å structure of RyR2 with GFP inserted after Thr2023 showed an extra mass in the T-tubule face of subregion 4(168). Similarly, the 27Å structure of RyR2 fused to GFP after Tyr2801 displayed an extra mass in the bridging density connecting subregions 5 and 6(169). In agreement, an extra mass appeared in the periphery of subregion 6 in the 25Å structure of RyR1 in complex with a monoclonal antibody raised against residues 2756-2803 (RyR2 residues 2722-2769)(169). See Section 1.3.6.4 for pseudo-atomic models of phosphorylation domains.

One hypothesis concerning the effect of PKA phosphorylation on RyR2 is that it causes the dissociation of FKBP12.6, a protein thought to stabilize the closed state of the channel(170-172). PKA phosphorylation would thus lead to enhanced channel opening. However, given the large distance between the FKBP12.6 binding site (see Section 1.3.4.1) and the presumed position of Ser2808, it was concluded that Ser2808 cannot be directly involved in FKBP12.6 binding(169).

1.3.3.5 Remark on insertion studies

In the absence of atomic-resolution structures for the majority of the RyR parts, the use of monoclonal antibodies and protein insertions in conjunction with three-dimensional reconstructions continue to provide approximate locations of RyR components. Care must be taken when interpreting the data, as a piece of difference density can also appear further away

from the insertion site either due to overall conformational changes or due to the use of long flexible linkers.

1.3.4 Binding sites of protein binding partners

Using a similar approach to the insertion studies, the analysis of difference densities is very useful in locating the positions of RyR binding partners (Figure 1.6). The difference densities are either due to the binding partner itself or due to conformational changes that arise because of the binding. In contrast to fusion protein strategies, such results are not dependent on linker lengths, and the confidence about the exact location is, therefore, much higher.

1.3.4.1 FK506-binding proteins

FK506-binding proteins (FKBPs), also known as immunophilins, bind to RyR1 and RyR2 with high affinities and stabilize the closed state. FKBP12, a 12kDa protein as its name suggests, is found predominantly in the skeletal muscle, where it binds to each subunit of RyR1(173). In the cardiac muscle, FKBP12.6, a 12.6kDa protein, preferentially associates with RyR2(174). In early studies, the three-dimensional structures of RyR1-FKBP12 complexes at $\sim 35\text{\AA}$ resolution showed that FKBP12 binds between subregions 3, 5, and 9(175,176). In addition, less significant differences were observed in the bridging densities between subregions 5 and 6, which could indicate conformational changes due to the binding(176). The location was confirmed by a more recent study which showed the structure of the RyR1-FKBP12 complex at 16\AA resolution, whereby a crystal structure of FKBP12(177) was docked into the difference density(178). In another recent study, a 33\AA structure of the RyR2-FKBP12.6 complex highlighted a binding site similar to the one for FKBP12(179). The binding of FKBP12.6 seemed to cause conformational changes, as subregion 6 was more extended towards the T-tubule and the electron dense parts in the transmembrane region splayed apart.

1.3.4.2 Calmodulin

Calmodulin (CaM), or calcium-modulated protein, regulates various cellular processes through binding and unbinding of Ca^{2+} in its two domains, N-lobe and C-lobe, each containing two EF-hand motifs. CaM binds to RyR1 in both the absence (apoCaM) and presence (Ca^{2+} /CaM) of Ca^{2+} . For further functional implication of CaM binding, see Section 1.3.5.1.

The binding site of Ca^{2+} /CaM on RyR1 was first studied using gold-cluster labeled CaM(180) and later confirmed by a 37Å RyR1-CaM complex(176). Ca^{2+} /CaM binds between subregions 3 and 8a, and its association did not seem to cause major alterations in the conformation of RyR1. The Ca^{2+} /CaM binding site is approximately 90Å away from the FKBP12 binding site(176). Similarly, RyR1-apoCaM complex at 28Å resolution showed that the apoCaM binding site is located at the outer surface of subregion 3, just above the binding site for Ca^{2+} /CaM and closer to the T-tubule(181). These studies suggest that binding of Ca^{2+} can cause one or both CaM lobes to hop from one binding site to another, which supports the different functional effects that Ca^{2+} binding and unbinding in CaM have on RyR1(182-184).

1.3.4.3 Chloride intracellular channel 2

Chloride intracellular channel 2 (CLIC-2) is a protein that is widely expressed in the skeletal and cardiac muscle of vertebrates(185), and which exist in a soluble and membrane-bound form(186). This 247-residue protein is homologous to the glutathione-S-transferase (GST) superfamily and was found to inhibit both RyR1 and RyR2(185,187). A 25Å structure of the RyR1-CLIC2 complex showed that CLIC-2 binds between subregions 5 and 6(187). Moreover, CLIC-2 binding seemed to separate subregions 9 and 10, resembling the open conformation despite the fact that the pore appeared to be closed.

1.3.4.4 Toxins

Being strictly required in E-C coupling and many other Ca^{2+} -dependent events, it is not surprising that RyRs are the targets of various toxins. Among these is imperatoxin A (IpTx_a), a 33-residue peptide derived from scorpion venom, that is known to bind to both RyR1 and RyR2 with high affinity, locking the channels in subconductance state(188,189). Because IpTx_a is too small (3.7kDa) for cryo-EM studies, it was N-terminally fused to biotin and bound to avidin. A 29Å cryo-EM reconstruction of the resulting complex with RyR1 showed that IpTx_a binds in the crevice between subregions 3, 7, and 8a(190).

Another toxin known to associate with RyRs is natrin, a 221-residue protein derived from venom of the snake *Naja naja atra*. Natrin belongs to the cysteine-rich secretory protein (CRISP) family and inhibits RyR1(191). A 21Å resolution structure of the RyR1-natrin complex showed that the toxin binds between subregions 5 and 6 on the surface exposed to the cytoplasm(191).

1.3.5 X-ray crystallography and NMR

Being giant eukaryotic proteins, RyRs present major challenges to high-resolution studies. The cryo-EM reconstructions have shown that RyR consists of individual globular regions, which opens up the avenue for a “divide and conquer” approach, or atomic-resolution studies of individual RyR domains.

1.3.5.1 EF-hand proteins in complex with RyR peptides

The first high-resolution structures came from a small region (RyR1 residues 3614-3643) in complex with CaM(192) and S100A1(193)(Figure 1.7).

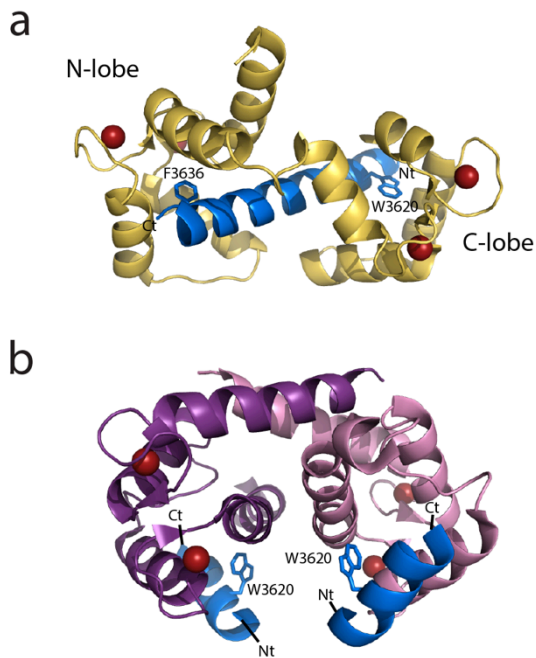


Figure 1.7: Binding partners containing EF hands. (a) Crystal structure of Ca²⁺/CaM (yellow) bound to RyR1 peptide (blue, residues 3614-3643; PDB accession code 2BCX). (b) NMR structure of an S100A1 dimer (purple) bound to two RyR1 peptides (blue, residues 3616-3627; PDB accession code 2K2F). Aromatic anchors providing major contacts are indicated (W3620 and F3636). Red spheres represent Ca²⁺ ions.

1.3.5.1.1 CaM-peptide complex

As described in Section 1.3.4.2, CaM is an EF-hand containing protein that can fine-tune the Ca²⁺-dependent feedback to RyRs. For example, at low cytoplasmic Ca²⁺ concentrations, apoCaM potentiates opening of RyR1, whereas Ca²⁺/CaM inhibits the channel(182-184). In contrast, both apoCaM and Ca²⁺/CaM seem to inhibit RyR2(194,195).

A 2.0Å crystal structure of Ca²⁺/CaM in complex with a peptide from RyR1 (residues 3614-3643) was solved by Mackenzie and coworkers(192). The RyR1 peptide forms an α helix, with both lobes of CaM binding in an anti-parallel arrangement, in which the N-lobe binds to the C-terminal half of the peptide, and the C-lobe binds the N-terminal half (Figure 1.7a). The main

hydrophobic anchors, Trp3620 and Phe3636, have an unusual “1-17” spacing, whereby the CaM lobes do not interact with one another. In the same study, solution NMR ^1H - ^{15}N residual dipolar couplings (RDCs) suggest that the lobes experience independent domain motions in solution, such that the RDCs for the two lobes cannot be fitted simultaneously to the crystal structure. This is compatible with the notion that multiple CaM-binding domains (CaMBDs) are present within RyR, and that individual lobes may associate with distinct CaMBDs(196,197). Since the cryo-EM reconstructions showed only one CaM bound per RyR monomer(176,181), these stretches have to be close for CaM to bridge. Given the large number of possible RyR fragments that can bind CaM(3,198-200), understanding the binding and effects of apoCaM and Ca^{2+} /CaM on RyRs involves solving a complex puzzle.

1.3.5.1.2 S100A1

S100A1 is an EF-hand containing protein from the S100 protein family. It exists as homodimers, with each monomer containing a low- and high-affinity EF hand. It enhances the opening of both RyR1 and RyR2(201-204).

An NMR structure has shown the interaction between Ca^{2+} /S100A1 and RyR1 (residues 3616-3627)(193)(Figure 1.7b). Interestingly, some residues (including Trp3620) are involved in binding both CaM and S100A1, showing that both proteins compete for the same binding site. It is, therefore, possible that the effect of S100A1 is due to a competition with CaM: at high Ca^{2+} levels, S100A1 can compete with Ca^{2+} /CaM and, thus, abolish its inhibitory effect on the channel.

1.3.5.2 N-terminal region

The N-terminal region, covering the first ~600 amino acid residues, harbors many disease-associated mutations in both RyR1 and RyR2. Several crystallographic and NMR studies have focused on this region.

1.3.5.2.1 Domain A of RyR1 and RyR2

The first atomic-resolution structure of a RyR domain was reported by Ikura and coworkers, covering the first domain of RyR1 (residues 1-205)(205). This was soon followed by another study, describing the same domain in both RyR1 and RyR2(206). In both studies, the N-terminal domain (referred to as “domain A” from here on) consists of a β -trefoil core, built by 12 β strands, and a single α helix (Figure 1.8). In line with the high degree of sequence conservation, only minor differences are present between domains A of RyR1 and RyR2. However, a recent NMR structure of RyR2 domain A revealed a second α helix that is unique to RyR2(207). This unique α helix is dynamic and is located in proximity to the column region in the intact RyR2, suggesting an important role in the communication between the N-terminal and transmembrane regions(207).

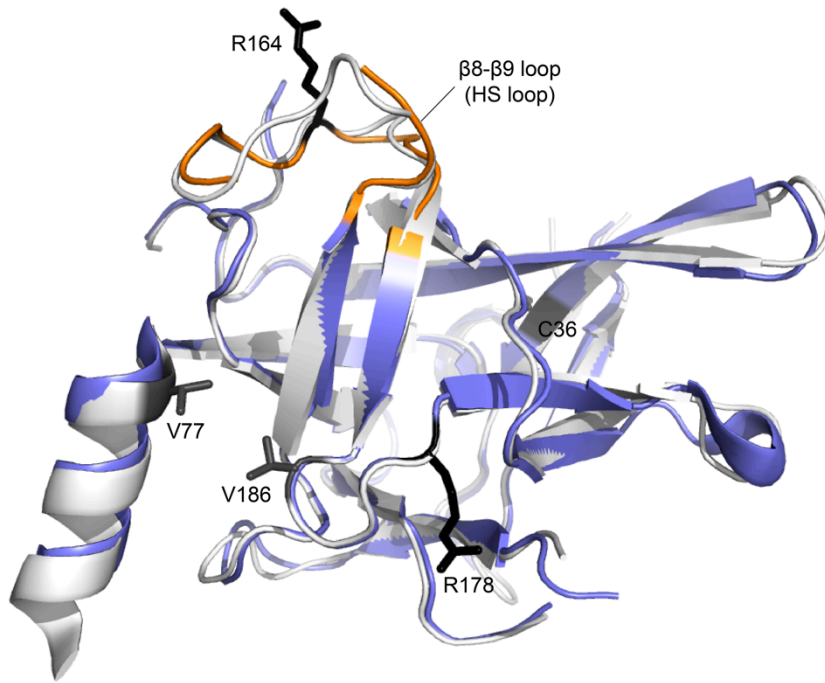


Figure 1.8: Crystal structures of RyR1A and RyR2A. Superposition of RyR1A (blue; PDB accession code 3ILA) and RyR2A (white; PDB accession code 3IM5) chains A. β 8- β 9 loop (HS loop) from RyR1A is highlighted in orange. Residues targeted by disease-associated mutations and for which the structural studies have been performed are shown in stick representations (RyR1 in black(205); RyR2 in gray(206)).

Both isoforms contain several disease mutations, many of which are located in a loop connecting the strands β 8 and β 9 (or β 8- β 9 loop), also referred to as a HS (hot spot) loop(205). Neither NMR nor crystallographic studies of mutant forms of this domain showed any significant differences in the stability or structure(205,206). Because the mutations appeared to be at the surface of domain A, it was assumed that they were located at interfaces for other RyR domains or auxiliary proteins. In Chapter 3, we show that point mutations at β 8- β 9 loop in RyR2 domain A may cause structural instability of the loop.

1.3.5.2.2 Domains ABC of RyR1

A recent study has depicted the 2.5Å crystal structure of the first 559 residues of RyR1, a region that covers the bulk of the N-terminal region(208). The structure folds up as three independent domains (A, B, and C) that interact with one another in a compact form (Figure 1.9a). Domains A and B both fold up as β -trefoil cores, whereas domain C consists of a bundle of 5 α helices. The domain-domain interactions are mainly hydrophilic in nature and inherently weak.

In RyR1 and RyR2 combined, over 75 disease-associated mutations could be located on the structures. A significant portion of those are located at the interface between domains A, B, and C, likely destabilizing the domain-domain interactions. These include mutations that abolish ionic pairs across the domains(209) or abolish the anion binding(210). Detailed structural and biochemical studies of these mutants are covered in Chapters 2 and 4.

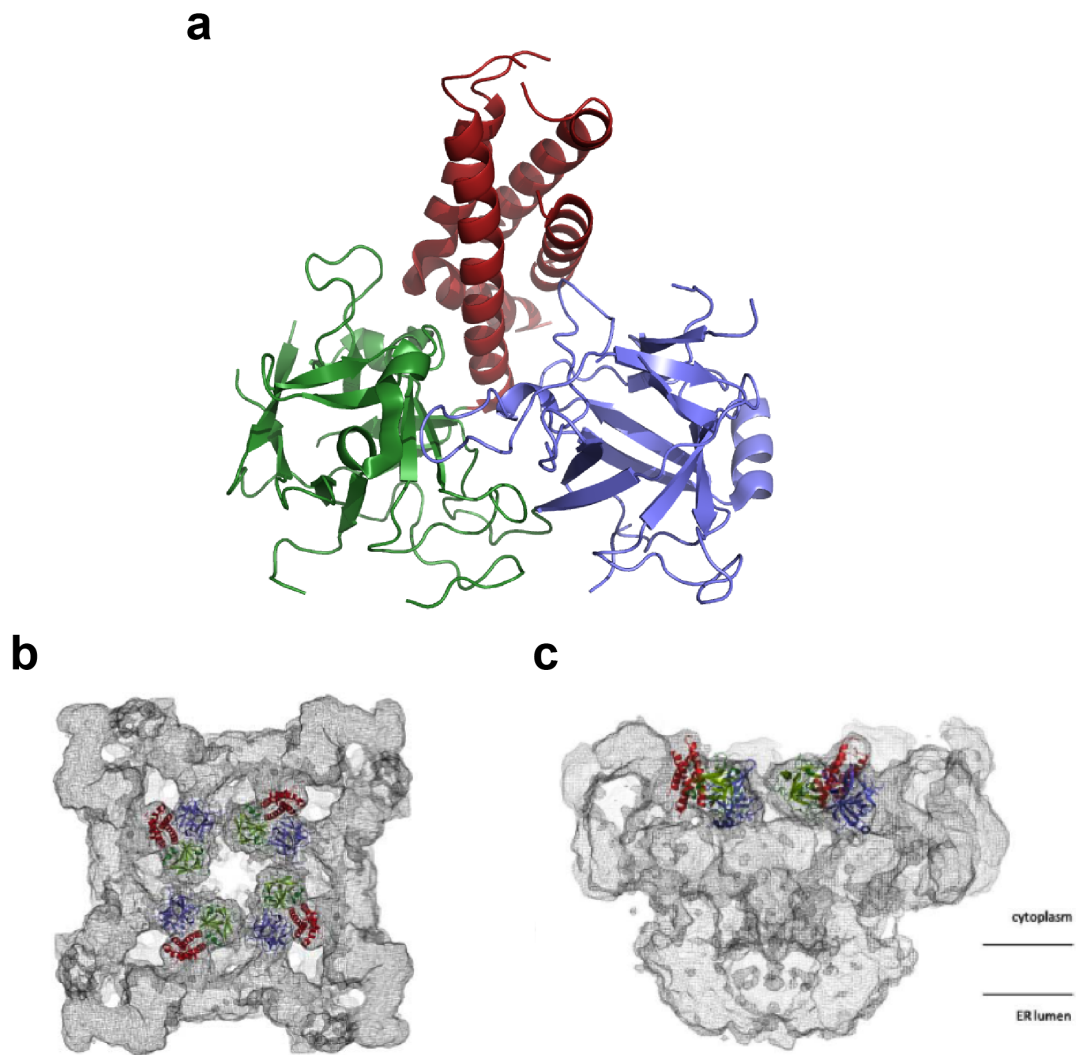


Figure 1.9: The structure and docking of RyR1ABC. (a) Overall structure of rabbit RyR1 for amino acid residues 1-559. This portion of RyR1 consists of domain A (blue; residues 1-205), domain B (green; residues 206-394), and domain C (red; residues 395-532). The remaining 27 residues are not visible in the electron density. (b,c) Docking of RyR1 ABC in the $\sim 10\text{\AA}$ RyR1 cryo-EM map (EMDB accession code 1275). A view from the cytoplasmic side towards the endoplasmic reticulum (b), and a side view showing a vertical cut through the cryo-EM map at the four-fold axis (c).

1.3.5.2.3 Exon-3 deletion in domain A of RyR2

A very severe form of CPVT is due to the deletion of a 35-residue segment (exon 3) in the N-terminal domain (domain A) of RyR2. The deletion ablates an α helix and a β strand that is part of the domain A β -trefoil core. However, the exon-3 deletion in RyR2 domain A unexpectedly did not cause misfolding of the protein, and even more surprisingly, the deletion enhanced the thermal stability of the domain(206). A recent crystal structure of RyR2A with exon 3 deleted highlights a very unusual “structural rescue,” in which a flexible loop (exon 4), unique to RyR2, takes over the deleted β strand(211) (Figure 1.10b). A recent NMR structure revealed that exon 4 forms a dynamic α helix unique to RyR2, located close to the column region of an intact channel(207)(Figure 1.10a). This switch from α helix to β strand suggests that alternative splicing, allowing either exon 3 or exon 4 to insert itself in the β -trefoil core, enables fine-tuning the activity of RyR2.

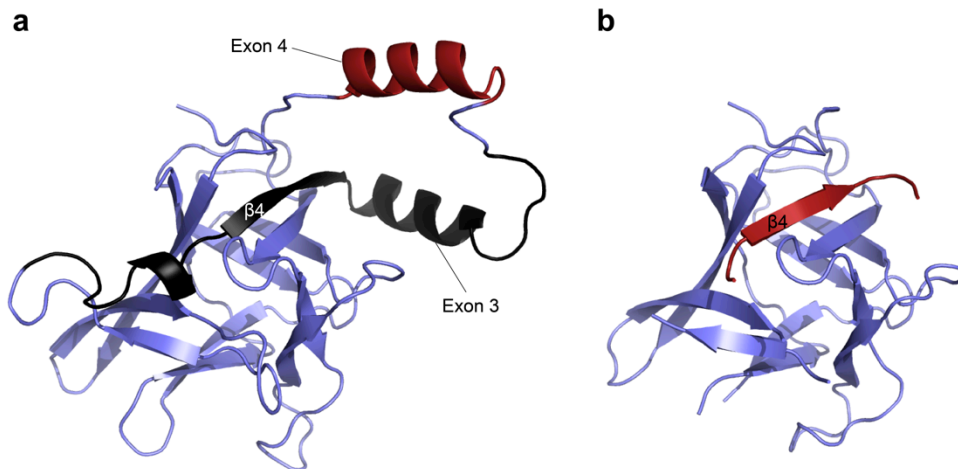


Figure 1.10: Structures of the RyR2A wildtype and exon 3 deletion mutant. (a) The X-ray crystallography-resolution NMR hybrid structure of RyR2A wildtype (PDB accession code 2MC2). Exon 3 is colored in black, and exon 4 is colored in red. The β strand in exon 3 (β_4) is labeled. (b) The crystal structure of the RyR2A exon-3 deletion mutant (PDB accession code 3QR5). The coloring is the same as in (a).

1.3.5.3 Phosphorylation domain in the central region

RyRs are regulated by several kinases (PKA, PKG, CaMKII) and phosphatases (PP1, PP2A, PDE4D3)(27). In particular, phosphorylation of RyR2 by PKA provides a link between physiological stress and RyR function: stress activates β -adrenergic receptors, which then consequently activates PKA and ultimately RyR. For this reason, PKA phosphorylation of RyR2 has gained a large amount of interest.

Several phosphorylation sites have been identified in the cytoplasmic portion of RyRs: Ser2843 in RyR1 and Ser2030 and Ser2808 in RyR2. Some groups believe that the hyperphosphorylation of RyR2 is the leading cause of heart failure via dissociation of FKBP12.6(165,172,212). Nonetheless, this proposed mechanism is still under debate since other groups could neither detect PKA hyperphosphorylation in heart failure nor confirm FKBP12.6 dissociation by PKA phosphorylation(80,213,214).

Two recent studies report the crystal structures of a phosphorylation domain in RyR1(215) and in all three isoforms(216): RyR1 residues 2734-2940 (rabbit numbering), RyR2 residues 2699-2904 (mouse numbering), and RyR3 residues 2597-2800 (human numbering). This single domain consists of two symmetric halves, each half containing two α helices, one or more short 3_{10} helices, and a C-terminal β strand (Figure 1.11).

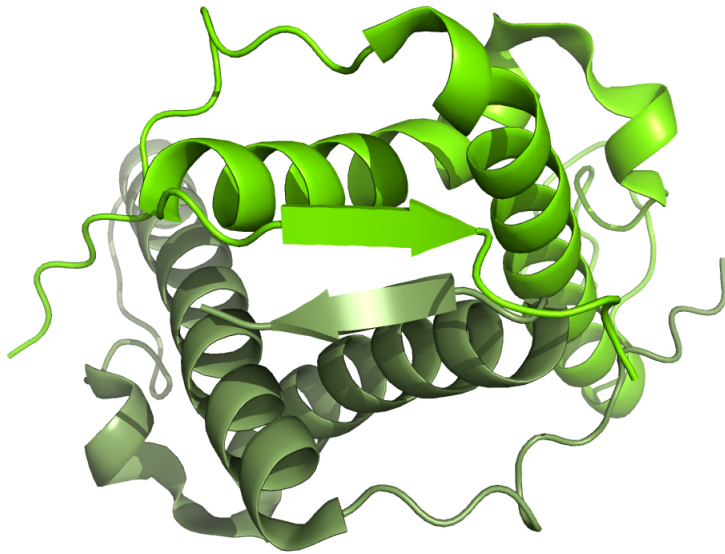


Figure 1.11: Structure of RyR1 phosphorylation domain. The crystal structure of RyR1 phosphorylation domain (rabbit residues 2734-2940; PDB accession code 4ERT). The symmetric two halves are colored in different shades of green for clarity.

Multiple phosphorylation sites were identified in RyR2, and most of them cluster in a long, flexible loop(216). Although RyR2 has no reported mutation in this domain thus far, the corresponding domain in RyR1 contains up to 11 mutations. Several of these are located close to the phosphorylation sites, on the same face of the domain. This indicates that phosphorylation and disease mutations target the same interface and may have the same effect on the channel(216).

Several disease-associated mutations in the phosphorylation domain have been studied. L2867G mutation in RyR1 drastically reduced the thermal stability of the domain by more than 10°C, and the same mutation caused aggregation of the domain at room temperature(216). Crystal structures of several RyR1 mutants (E2764K, S2776M, and R2939S) showed that these mutations alter the surface properties and salt bridges within the domain(216), which may affect

interfaces between binding partners (such as PKA) or neighboring domains (such as the FKBP binding site).

1.3.6 Pseudo-atomic models

The cryo-EM images of the entire receptor currently cannot locate the positions of individual amino acids. Concurrently, high-resolution structures of individual portions provide limited information when their locations in the full-length proteins are unknown. With both techniques combined, however, it is feasible to start constructing pseudo-atomic models by docking high-resolution fragments into the cryo-EM maps.

1.3.6.1 Remark on docking reliability

Several algorithms exist to dock fragments, making use of six-dimensional searches (three translational and three rotational parameters) along with a scoring function. Crucial parameters for a successful experiment include the quality and resolution of the cryo-EM reconstruction, as well as the relative size of the fragment compared to the intact protein. When only small fragments are used, a simple cross-correlation coefficient may not suffice to provide a reliable position(217,218). In those cases, it may be advantageous to make use of a Laplacian filter, which enhances the features of the surface. Although the latter may increase high-frequency noise, the ideal method for any particular case can be identified through a statistical analysis of the correlation coefficients, whereby a correct solution has a correlation coefficient that is significantly higher than the second best solution. In the absence of such a docking contrast, the reliability of the top solution may be questionable.

1.3.6.2 N-terminal region: domains ABC

Prior to the availability of high-resolution structures, some homology-based models were prepared for the N-terminal region, and these were docked in the clamp region(120,219).

However, using the crystal structure of the N-terminal domains, a high-contrast solution places the N-terminal region in the central rim, forming a vestibule around the fourfold symmetry axis(208)(Figure 1.9b,c). Using the segmentation described by Serysheva *et al.*(120), domain A occupies subregion 1, whereas domains B and C occupy subregions 2a and 2b, respectively. The different results with the prior docking studies are most likely due to discrepancies between the homology based models and the crystal structure, and due to the use of different docking algorithms. The docking is also at odds with the proposed subunit boundaries(120).

The N-terminal domains, thus, seem to form interactions with the same region in a neighboring subunit, mostly involving contacts between domains A and B. This interface contains the largest concentration of disease mutations in the region. A side view shows that the area is located far away from the transmembrane region, but is connected to the pore-forming region via electron dense columns (Figure 1.9c). All mutations at the periphery of the N-terminal region were found to be located at one of six different interfaces with other RyR domains. No mutation was found to be located in the exposed surface area, consistent with the fact that no protein-binding partner has been found in this region.

The location of the N-terminal region shows apparent discrepancies with the cryo-EM analysis of fusion proteins containing GFP inserted near residue Ser437 in RyR2(144), or with GST fused to the N-terminal of RyR3(143). However, when the length of the linkers is taken into account, together with the inherent length of the loop region containing Ser437, these studies can be reconciled(208). In addition, the GST-RyR3 fusion construct displayed two main regions of difference density, suggesting that the fusion created conformational changes. One of these is located right next to the N-terminus of the docked RyR1ABC domains.

The cryo-EM studies comparing RyR1 in the open and closed states have shown significant movements in the central rim where the N-terminal region is located(122). Together with the distribution of the disease mutations, it is plausible to assume that most or all of the domain-domain interfaces involving the region are labile and subject to movement. This creates an energetic penalty to open the channel, therefore, assigning the role of a “brake” to the N-terminal region. When disease mutations perturb any of these interfaces, the energetic penalty is reduced, making it easier for the channel to open. This is consistent with the fact that most mutations characterized so far lead to a gain of function, including increased sensitivity to modulators and leakage of Ca^{2+} (14). Combining the mutations with another event (increased temperature, binding of halogenated anesthetics, phosphorylation, *etc.*) is then sufficient to open the channels. The perturbation of domain-domain interfaces by the disease-associated mutations is described in greater detail in Chapter 2 and Chapter 4.

1.3.6.3 N-terminal region: residues 850-1060

In a recent study, homology models of RyR1 residues 850-1056 and RyR2 residues 861-1067 were built based on sequence homology with the crystal structure of RyR1 2733-2940 phosphorylation domain(220). The homology models were docked into the cryo-EM reconstruction of RyR1, where they were found to be located in subregion 5, connecting the central vestibule (where domains ABC are located) and the clamp region (where phosphorylation domain is located)(220). Furthermore, subregion 5 is positioned adjacent to the proposed FKBP binding site. Thus, the end of the N-terminal region may hold a key role in bridging multiple regulatory mechanisms within the channel: phosphorylation, FKBP binding, and conformational changes accompanying channel opening. However, care must be taken when interpreting

homology models, as they may not always reflect the true structure. Also, pseudo-atomic models from a small fragment may not give a reliable docking result, as discussed in Section 1.3.6.1.

1.3.6.4 Phosphorylation domain

Two recent studies have used the crystal structures of the phosphorylation domain to dock into the cryo-EM reconstruction of RyR1(215,216). Both docking studies resulted in the phosphorylation domain fitted in subregion 10 in the clamp region. Due to the two-fold-symmetry of the domain, two alternative orientations within subregion 10 are possible(216). In one of the orientations, the side of the domain containing the phosphorylation-site loop and disease-associated-mutation interface is facing an inner cavity within the channel. In the alternate orientation, the same side is now exposed on the outer surface of RyR1. Future docking experiments using a larger fragment or a cryo-EM map with much higher resolution would enable the identification of the correct orientation of the domain within the channel.

The clamp region of RyR1 has previously been shown to undergo large motions upon channel opening, with the corners bending down towards the ER membrane by $\sim 8\text{\AA}$ (122). A recent study has also shown that the same region of RyR2 is subject to conformational changes in ligand-dependent manner(149). Thus, phosphorylation and mutations in this area may affect allosteric motions in the region that normally accompany channel gating(216). The phosphorylation domain may also be involved in the formation of RyR lattices, as the neighboring subregion 6 has been shown to mediate intermolecular contact between adjacent RyRs(110,111,221,222).

1.3.7 Analogies with the inositol-1,4,5-triphosphate receptor

Inositol-1,4,5-triphosphate receptors (IP₃Rs) are another family of Ca²⁺ release channels, predominantly present in the ER membrane. Sizing $\sim 1\text{MDa}$, IP₃R is the “little brother” of the

RyRs, and a significant amount of homology (~30% sequence identity) is found between the two channels. Not surprisingly, a great deal of structural homology is present as well, and IP₃R have been studied by both electron microscopy and X-ray crystallography.

Several cryo-EM reconstructions of IP₃Rs have been performed, but since most seem at odds with one another, it has been difficult to directly compare these with RyR reconstructions(223-228). In a recent study, however, a ~14Å cryo-EM reconstruction of IP₃R reveals an overall mushroom shape, sharing the same hallmark feature of RyR, while the cytosolic cap is considerably smaller than that of RyR(229,230).

Three IP₃R domains have been investigated with X-ray crystallography. Crystal structures are available for the N-terminal suppressor domain (equivalent to domain A of RyR)(231,232), and for the following two domains known together as the IP₃ binding core (equivalent to domains BC of RyR) in complex with IP₃(233). A structure describing all three domains together had been elusive until recently. Since then, crystal structures of the IP₃RABC domains, in absence of the ligand and in complex with IP₃, have become available(234,235). IP₃RABC domains were docked in the central rim of the cryo-EM reconstruction of IP₃R, very much like the N-terminal domains of RyR(234)(Figure 1.12).

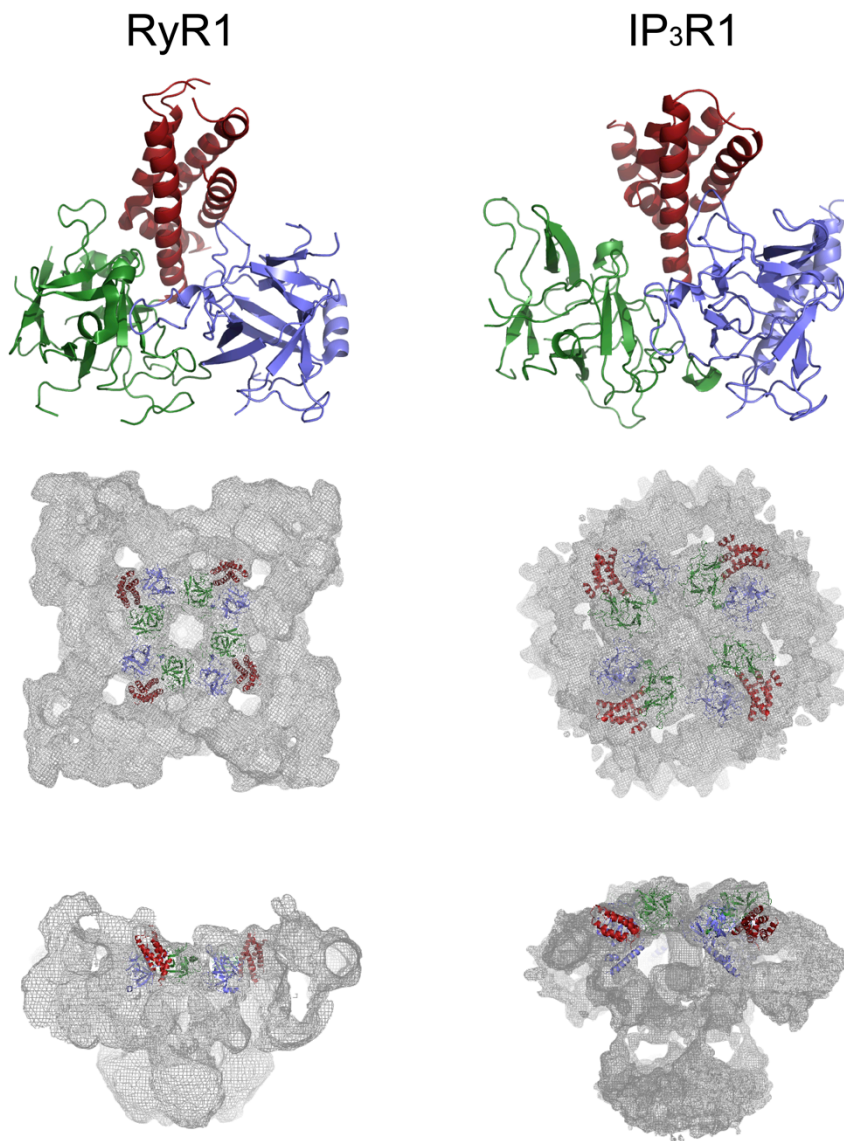


Figure 1.12: Structural conservation between RyR and IP₃R. **(Left)** The structure of RyR1ABC (domain A in blue, domain B in green, and domain C in red; PDB accession code 2XOA) and the top and side views of the docking in the RyR1 cryo-EM reconstruction (EMDB accession code 1606). The density of the cryo-EM reconstruction is clipped for clarity. **(Right)** The structure of apo IP₃R1ABC (PDB accession code 3UJ4) in the same coloring scheme as in RyR1ABC and similar views of the docking in the IP₃R1 cryo-EM reconstruction (EMDB accession code 5278).

The RyR ABC domains have a surprisingly large amount of structural homology with the IP₃R N-terminal domains, a feature that was predicted before the RyR1ABC crystal structure was determined(120). The secondary structure elements in the two β-trefoil domains and the α-helical bundle in domain C superpose very well (Figure 1.12). The structural conservation underlines the evolutionary relationship between the two channels, and the interactions between the suppressor domain and the IP₃ binding core have been suspected to be similar as well(208,236). Indeed, the crystal structure of IP₃RABC shows rearrangement of the three domains upon binding of IP₃(234,235), much like the rearrangement seen in RyR1ABC mutants(209) (See Chapter 2 for detail). The movement in the N-terminal domains may be a common theme among the Ca²⁺ release channels, where channel opening is facilitated through targeting the ABC domain-domain interface via ligand binding or disease mutations(27,209).

1.3.8 Research question

Despite the efforts of numerous functional studies in understanding the molecular mechanism behind RyR-linked diseases, such knowledge remains elusive largely due to the lack of high-resolution structures of the channel. High-resolution structures of RyR domains and biochemical studies provide great details on the mutations. For example, do disease-associated mutations cause complete unfolding of the protein, or do they cause distinct structural changes? Do the structural changes destabilize domain interfaces, or do they cause permanent reorientations of the domains? Which side chains are involved? Are there new contacts caused by the mutations?

One important step in uncovering the mechanisms of mutations is to locate their positions in the full-length channel. By combining crystal structures of individual domains and

cryo-EM reconstructions of the full-length RyR, pseudo-atomic models can be obtained. These models give important clues, such as interfaces affected by the disease-associated mutations.

We combine X-ray crystallography, cryo-EM docking studies, and thermal melt assays to analyze the folding and stability of the N-terminal regions of RyR1 and RyR2.

Chapter 2: Disease mutations in the ryanodine receptor N-terminal region couple to a mobile intersubunit interface

Mutations in ryanodine receptors (RyRs) can result in severe disease phenotypes. More than 300 have been identified in RyR1, associated with malignant hyperthermia (MH)(15), central core disease, and related conditions(16). In the cardiac isoform, more than 150 mutations have been linked to catecholaminergic polymorphic ventricular tachycardia(17), arrhythmogenic right ventricular dysplasia type 2, and idiopathic ventricular fibrillation(18). Many mutations cluster in three distinct “hot spots” within the sequence, but several others, especially for RyR1, are increasingly found outside of these clusters (Figure 2.1).

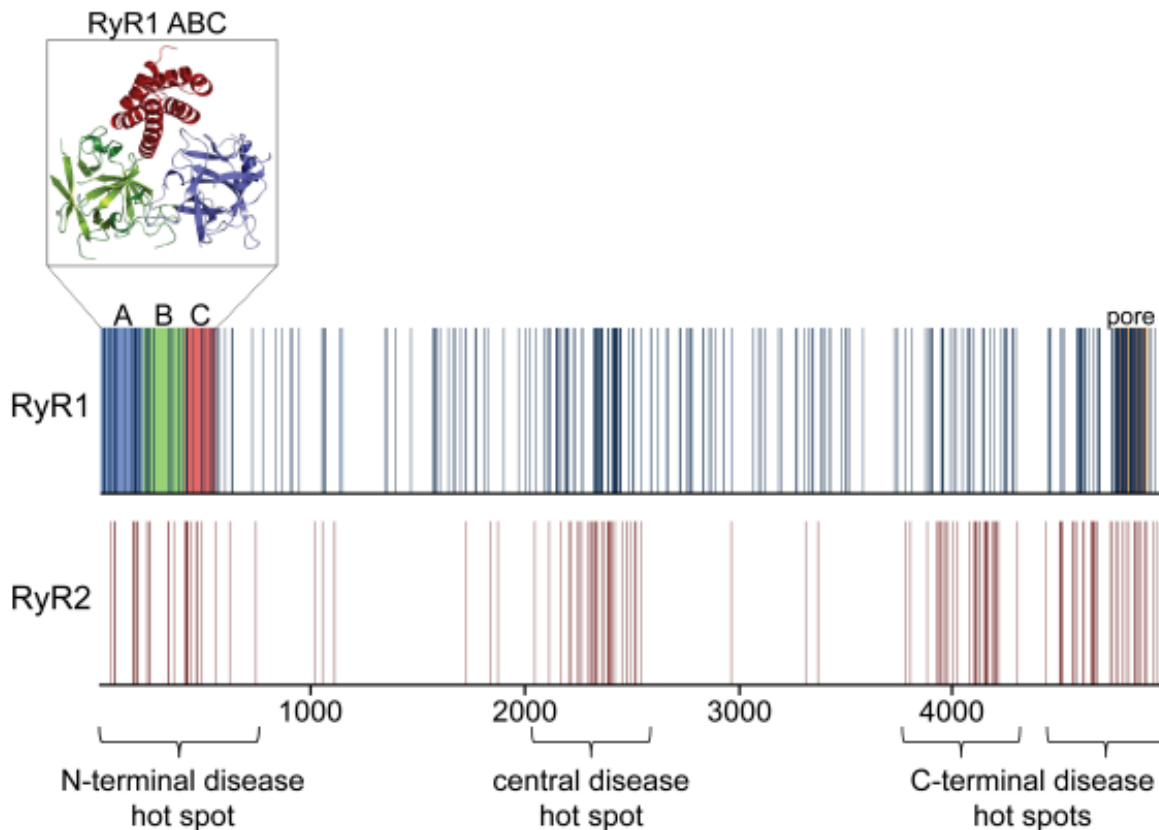


Figure 2.1: A linear view of RyR1 and RyR2 disease mutations. Amino acid residue numbers are shown below. Vertical lines indicate disease-associated mutations. There is still a clear clustering of mutations in RyR2, but several mutations are increasingly found outside of the initially proposed hot spots for RyR1. The RyR1 N-terminal ABC domains and the pore-forming region are highlighted. The crystal structure of wild-type RyR1ABC (PDB accession code 2XOA) is shown above.

The primary trigger for RyR opening is Ca^{2+} , the same ion it permeates. RyRs can be activated by either cytoplasmic or luminal Ca^{2+} ions(26,237), but higher cytoplasmic Ca^{2+} concentrations can inhibit RyRs(2). In the skeletal muscle, RyR1 can also be triggered to open through conformational changes in the L-type calcium channel $\text{Ca}_v1.1$, which is thought to interact directly with RyR1(11). In addition, a host of regulatory proteins and small molecule

ligands can alter the sensitivity to these primary triggers. The precise mechanisms by which Ca^{2+} or $\text{Ca}_v1.1$ alter channel gating are still unknown.

Several high- and low-resolution studies have shed light on the RyR structure(238). Cryo-electron microscopy (cryo-EM) studies depict a mushroom-shaped structure with the stem forming the transmembrane region, and the cap located in the cytoplasm(2,11). A study comparing the open and closed states suggests that channel opening is the result of inner transmembrane helices that bend, in agreement with high-resolution studies on other ion channels(122). However, helix bending in RyRs is still a contentious issue(119). Channel opening also coincides with many movements in the cytoplasmic area(122), showing that RyRs are *bona fide* allosteric proteins. As a result, RyR-interaction partners that bind far away from the pore region can influence channel opening. For example, any partner that preferentially stabilizes the open state can facilitate channel opening. The overall open probability is, thus, the result of the integrated effect of ligands with positive and negative input. Similarly, any mutation that selectively affects one of the states may facilitate or inhibit channel opening.

Several crystallographic studies have shed light on RyR domains(205,206,208). The N-terminal region (RyR1 residues 1-532), containing the bulk of the proposed N-terminal disease hot spot, is built up by three domains (A, B, and C) (Figure 2.1) and forms a cytoplasmic vestibule(208). This position was recently confirmed via a cryo-EM reconstruction, whereby green fluorescent protein was inserted in RyR2 domain B(239). For simplicity, we refer to the three domains together as the N-terminal disease hot spot. In the related inositol-1,4,5-triphosphate receptor (IP_3R), the corresponding region forms the binding site for IP_3 , which triggers channel opening(234,235). However, a direct functional role for the RyR N-terminal domains is unknown.

Most mutations studied so far seem to confer a gain-of-function phenotype, whereby channel opening is facilitated(27). However, some mutations associated with central core disease and idiopathic ventricular fibrillation, mostly located in the transmembrane area, can confer a loss-of-function(70,99). How can N-terminal disease mutations, located $>100\text{\AA}$ away from the transmembrane inner helices, facilitate channel opening? Most of them are found at domain-domain interfaces, suggesting that perhaps some or all of these interfaces undergo changes during channel opening, and that disease mutations directly interfere with such events. Here we compare pseudo-atomic models of the N-terminal area in the open and closed states, and look at crystal structures of disease mutations that affect domain-domain interactions. We present a model whereby neighboring N-terminal hot spots interact through an interface that is disrupted upon channel opening.

2.1 Methods

Throughout the section, all numbering corresponds to the amino-acid sequence of rabbit RyR1.

2.1.1 Cryo-EM docking

The RyR1ABC crystal structure (PDB accession code 2XOA) was docked into open and closed RyR1 cryo-EM reconstructions described by Samsó *et al.*(122) (EMDB accession codes 1607 and 1606, respectively). The full structure was placed four times in the four-fold symmetric map using extensive six-dimensional searches using the colores program in the Situs 2.6 package(240). Contrast plots, showing the correlation coefficients of the top solutions were prepared based on this docking. The positions of all twelve individual domains were further refined by rigid-body refinement, taking steric clashes into account as implemented in the collage program of Situs 2.6(240). A Laplacian filter was applied during all stages.

2.1.2 Cloning and crystallization of disease mutants

RyR1ABC proteins (wild type and mutants) were expressed and purified as described previously(208), with the difference that most constructs encompassed residues 1-536 instead of 1-559, because the C-terminal 27 residues were found to be unstructured. The exception is the R45C mutant, where the 1-559 construct was used for crystallization. All thermal melts were performed on the 1-536 constructs.

The RyR1BC construct (residues 217-536) was cloned in the same pET28HMT vector as described before(208) and purified using a similar strategy as for RyR1ABC, with the following differences. After cleavage with Tobacco Etch Virus (TEV) protease and collecting the PorosMC flowthrough, the sample was run on a ResourceQ column (GE Healthcare) in 20mM Tris-Cl pH 8.0, 14mM β -mercaptoethanol (β -ME), with a gradient from 50 to 350mM KCl, and on a Phenyl Sepharose column (GE Healthcare) in 20mM Tris-Cl pH 8.0, 14mM β -ME, with a gradient from 50 to 1500mM KCl. The sample was then run on a preparative Superdex 200 as for the RyR1ABC proteins.

Before crystallization, the proteins were exchanged to 50mM KCl, 10mM Na-HEPES pH 7.4, 10mM dithiothreitol (DTT) and concentrated to 10mg ml⁻¹ using a 10,000 MWCO concentrator (Amicon, Millipore). All crystals were obtained using the hanging drop method at 4°C. L14R and D61N were crystallized in 1.4-1.6M ammonium sulphate (AS) and 0.1M HEPES pH 8.0 or 0.1M Bicine pH 9.5, respectively. V219I was crystallized in 1.4M AS, 12% glycerol, and 0.1M Bicine pH 9.0. G249R and I404M were crystallized in 1.3-1.5M AS, 12% glycerol, and 0.1M Tris pH 8.0. To refute an impact of pH on the structures, we also crystallized wild-type RyR1ABC in AS at three different pH values (pH 8.0, 9.0, and 9.5). C36R was crystallized in 1.2M lithium sulphate and 0.1M Bicine pH 9.5. R45C and R402G were crystallized in 20-22%

PA5100 sodium salt (PA5100), 0.02M MgCl₂, and 0.1M HEPES pH 7.0 or 0.1M Bis-Tris pH 6.5, respectively. RyR1BC crystals were obtained in 0.1M Tris-Cl pH 7-8, 100-250mM KCl, and 20-30% PEG 3350. All crystals were flash frozen in the corresponding mother liquor containing 25-30% glycerol.

2.1.3 Data collection and refinement

Data were collected at beamline 9-2 of the Stanford Synchrotron Radiation Laboratory (Menlo Park) and 08ID of the Canadian Light Source (Saskatoon). The data were processed using the HKL2000 package (HKL Research) and XDS(241). All structures were solved using molecular replacement implemented in Phaser(242), using individual domains of RyR1ABC(208) (PDB accession code 2XOA) as search models. Refinement consisted of successive rounds of manual modeling in COOT(243) and refinement in REFMAC5(244) with TLS restraints applied to individual domains. Data collection and refinement statistics are available in Table 2.1. Coordinates and structure factors for all described structures are available in the Protein Data Bank: L14R (PDB accession code 4I7I), C36R (4I0Y), R45C (4I6I), D61N (4I3N), V219I (4I8M), G249R (4I1E), R402G (4I37), I404M (4I2S), and RyR1BC (4I96). Superpositions and RMSD calculations were performed using ProFit (<http://www.bioinf.org.uk/software/profit>). The structures of wild-type RyR1ABC at pH 8, 9, and 9.5 were identical, indicating that the observed structural differences for the mutations were not due to differences in pH (Figure 2.10).

Table 2.1: Crystallographic parameters. Values in parentheses are for the highest-resolution shells. RMSD = root mean square deviation.

	L14R	C36R	R45C	D61N	V219I	G249R	R402G	I404M	RyR1BC
Data									
collection									
Space group	R32	R32	P6 ₃ 22	R32	R32	R32	P6 ₃ 22	R32	P3 ₁ 21
Cell									
dimensions									
a=b, c (Å)	171.40, 300.48	170.38, 302.11	118.16, 246.95	168.63, 301.65	169.27, 305.60	167.49, 304.70	118.26, 243.93	171.37, 299.43	68.45, 131.89
Resolution (Å)	50-2.9 (3.1-2.9)	50-2.8 (3.0-2.8)	50-2.5 (2.6-2.5)	50-2.95 (3.1- 2.95)	50-2.8 (3.0-2.8)	50-2.4 (2.5-2.4)	50-2.95 (3.1- 2.95)	50-2.5 (2.6-2.5)	50-2.7 (2.8-2.7)
R_{sym} or R_{merge}	14.7 (212.7)	11.1 (152.9)	16.0 (151.2)	15.0 (151.5)	12.9 (130.9)	6.7 (100.0)	12.9 (64.5)	9.7 (101.9)	13.0 (81.4)
R_{pim}	3.1 (45.3)	3.4 (47.1)	5.0 (46.4)	4.6 (46.6)	4.5 (45.9)	3.1 (46.5)	7.4 (37.2)	3.7 (39.3)	4.1 (25.5)
$I/\sigma I$	14.6 (1.8)	18.0 (1.9)	13.4 (1.9)	12.6 (1.8)	15.6 (2.0)	16.0 (1.8)	10.0 (2.1)	12.9 (1.9)	15.5 (3.4)
Completeness (%)	100.0 (100.0)	100.0 (100.0)	100.0 (100.0)	100.0 (100.0)	100.0 (100.0)	100.0 (100.0)	99.8 (100.0)	100.0 (100.0)	100.0 (100.0)
Redundancy	22.7 (22.8)	11.4 (11.5)	10.9 (11.1)	11.4 (11.5)	9.1 (9.1)	5.7 (5.7)	3.9 (4.0)	7.6 (7.6)	10.8 (11.1)
Refinement									
Resolution (Å)	50-2.9	50-2.8	50-2.5	50-2.95	50-2.8	50-2.4	50-2.95	50-2.5	50-2.73
No. reflections	35972	39670	34297	33250	39637	61106	20871	55655	9595
Rwork/Rfree	22.8/24.9	24.3/24.6	26.0/27.7	22.7/25.7	23.5/25.3	23.9/25.8	25.1/28.9	23.2/24.9	22.4/24.1
No. atoms									
Protein	3521	3495	3297	3546	3575	3603	3409	3598	1968

	L14R	C36R	R45C	D61N	V219I	G249R	R402G	I404M	RyR1BC
Ligand/ion	6	6	0	6	6	0	0	6	0
Water	16	17	56	14	36	99	27	70	16
B-factors (Å ²)									
Protein	61.7	24.1	22.3	39.2	31.3	31.5	18.9	21.4	26.4
Ligand/ion	132.7	104.2	n/a	91.1	107.8	n/a	n/a	95.7	n/a
Water	49.5	21.6	20.3	26.8	21.9	28.3	13.2	21.0	18.9
RMSD									
Bond lengths (Å)	0.006	0.006	0.005	0.006	0.005	0.005	0.007	0.006	0.011
Bond angles (°)	1.013	0.975	0.902	0.992	0.902	0.892	1.004	0.942	1.314

2.1.4 Thermal melt analysis

The protein melting curves were measured by means of thermofluor experiments(245). Samples for melting curves contained 50µl of 0.2mg ml⁻¹ protein and 1× SYPRO Orange solution (Invitrogen) using the manufacturer's instructions. The melts were obtained in a DNA engine opticon 2 real-time PCR machine (Bio-Rad), using the SYBR green filter option. The temperature was changed from 20 to 95°C in 0.5°C steps. At every step, the temperature was kept constant for 15s. The melting temperatures were obtained by taking the midpoint of each transition.

2.1.5 CD spectra measurement

CD spectra of RyR1ABC WT and G216E were measured in buffer containing 50mM KCl and 10mM Na₃PO₄ pH 7.4. Concentrations were determined using the calculated extinction coefficient at 280nm in the presence of 6M guanidine. CD spectrum measurements were performed using a Jasco J810 CD spectropolarimeter on samples at a concentration of 2µM. CD

spectra of the samples and buffer alone were collected over a spectral window of 195-280nm at 22°C.

2.2 Results

2.2.1 Pseudo-atomic models of the N-terminal disease hot spot

The opening of RyRs is allosterically coupled to the cytoplasmic cap, which undergoes large conformational changes(118,122,141,142). This includes movements in the central rim, a region surrounding the four-fold symmetry axis on the cytoplasmic face, where the N-terminal disease hot spot was found to be located(208,239). We, therefore, docked the crystal structure of the RyR1 N-terminal domains (RyR1ABC) in the open- and closed-state cryo-EM maps of RyR1, previously compared in a systematic study at reported 10.2Å(122). Consistent with previous results in three other RyR1 cryo-EM maps(208), RyR1ABC docks around the four-fold symmetry axis with a high docking contrast, whereby the top solution clearly stands out from the next solutions down the ranking (Figure 2.2a). As it is possible that the individual domains A, B, and C also undergo relative movements during channel opening, we further refined their positions in both maps by allowing a positional refinement of each individual domain. Figure 2.2b shows their final refined positions. A direct superposition of these pseudo-atomic models shows that there are substantial shifts up to 8Å (Figure 2.2c-f). The major rearrangement in the models can be described as “tilting,” whereby all domains move upward and outward, as if pivoting around a hinge outside the hot spot.

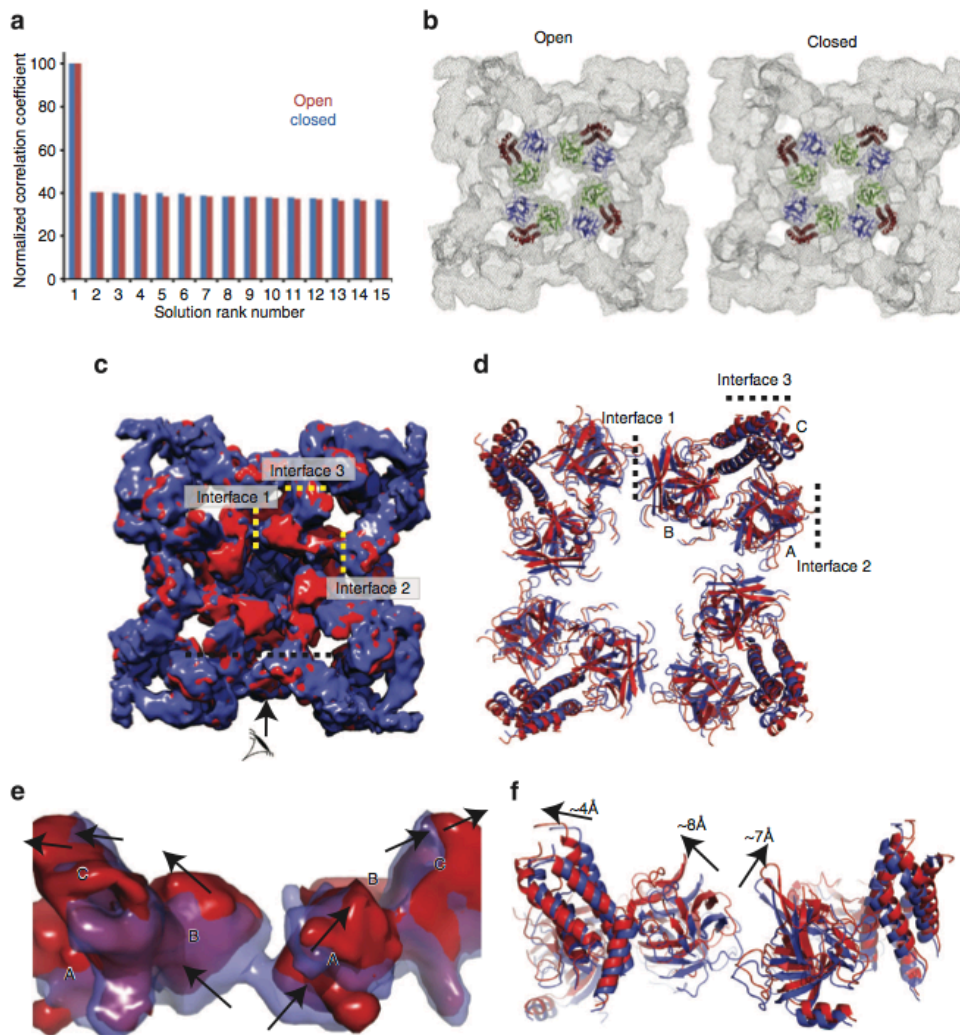


Figure 2.2: Pseudo-atomic models of RyR1ABC in open and closed RyR1. (a) Docking contrasts for RyR1ABC docking, before refinement of the individual domain positions, in the open (red) and closed states (blue), showing the Laplacian-filtered cross-correlation coefficients for the top 15 unique positions. The correlation coefficients are normalized to the highest score. (b) Positions of RyR1ABC (PDB accession code 2XOA) docked in the open (left, EMDDB accession code 1607) and closed (right, EMDDB accession code 1606) RyR1 cryo-EM maps. Different colors indicate the individual domains (A: blue, B: green, and C: red). (c,d) Top view (cytoplasmic face) of a superposition of the entire cryo-EM maps and the docked RyR1ABC domains after refinement of the individual domain positions in closed (blue) and open (red) RyR1. The arrow and black dotted line in c indicate a cross-section used for the side view in e. (e,f) Side view of the cryo-EM maps and the docked RyR1ABC domains. The portion of the maps shown is based on segmentation through Segger, as a plug-in for Chimera(246).

These overall shifts are also visible when comparing the corresponding density in the open- and closed-state cryo-EM maps(122) (Figure 2.2c,e). A key observation is that the changes are concerted: where density is systematically disappearing “below” the domains, extra density appears “above” (Figure 2.2e). Such concerted movements are highly improbable as a result of poor resolution or noise in the maps, as this would only cause random scatter in both directions.

Although these pseudo-atomic models do not allow a detailed description of interactions across subunits, they imply that domains A and B of neighboring subunits are juxtaposed, likely forming interactions in the closed state (“interface 1”). However, in the open-state model, the intersubunit gap is extended by $\sim 7\text{\AA}$, a distance that is undoubtedly large enough to break or alter many interactions (Figure 2.3a). Incidentally, the largest concentration of disease mutations in the N-terminal region is found facing the intersubunit boundary (20 for RyR1 and RyR2 combined). The bulk of the mutations are clustered in only three loops that are juxtaposed. One of these loops is located in domain A (connecting β strands 8 and 9), and was previously found to contain a dense cluster of mutations(205,206). The two other loops reside in domain B and are inherently flexible in the absence of their binding partner (Figure 2.3a, red dotted lines). How could these mutations affect channel opening? Mutations in the $\beta 8$ - $\beta 9$ loop were previously found not to cause any major structural or stability differences(205,206). This implies that the only way they can have an impact is by being directly involved in a functional interface, and we propose that they form part of intersubunit interactions that are disrupted upon channel opening. Any mutation that weakens these interactions will lower the energetic barrier to open the channel, and thus facilitate channel opening.

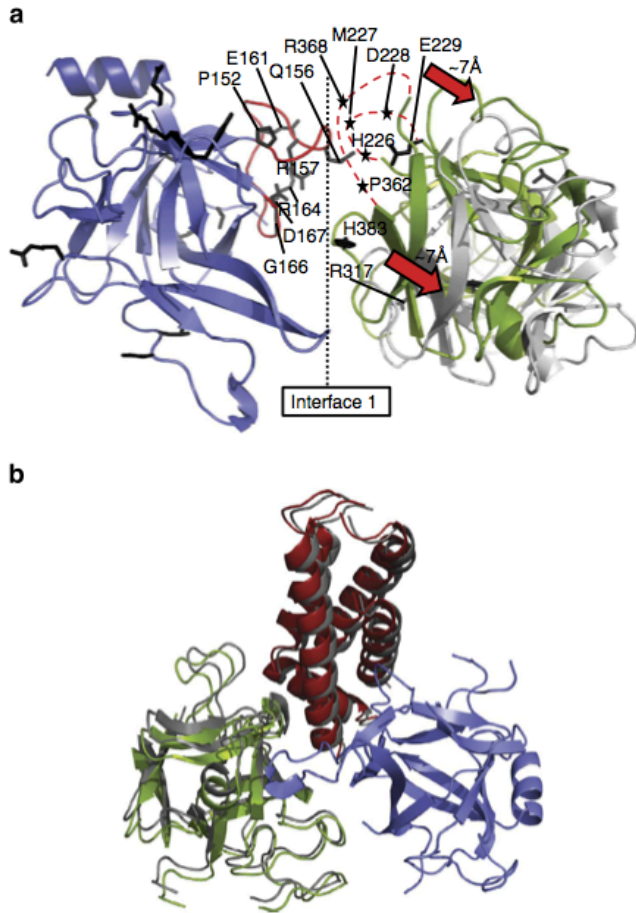


Figure 2.3: Relative positions between and within N-terminal disease hot spots. (a) Superposition of domain A (blue) in the open- and closed-state models, showing the relative position of domain B in a neighboring subunit (closed: green; open: grey). Disease mutations are shown as black sticks. Select mutations in three juxtaposed loops are labeled. The $\beta 8$ - $\beta 9$ loop in domain A is shown in red. Two flexible loops in domain B that contain multiple disease mutations are shown as red dotted lines, with disease mutations indicated by black asterisks. This interface is subject to a total of 20 disease mutations: P152S*, Q156K, R157Q*, E161G, R164C, R164L, R164Q*, G166R, D167N, D167G, H226R, M227K, D228V, E229K*, R317L, R317W*, P362M*, R368L, R368Q, and H383N, where asterisks indicate mutations found in RyR2 (all in rabbit RyR1 residue numbering). (b) Superposition of the closed (colors) and open (grey) RyR1ABC models, based on domain A (blue), indicating the relative positions of domains B (green) and C (red). These conformational changes are too small to be interpreted at the resolution of the cryo-EM maps, so that channel opening does not seem to induce major conformational rearrangements within each hot spot.

The study by Samsó *et al.*(122) is the only one that systematically compared the open and closed states at a resolution $\sim 10\text{\AA}$. Comparing the docking in two other cryo-EM maps near $\sim 10\text{\AA}$ (119,121) also supports the idea that channel opening coincides with a widening of the intersubunit gap (Figure 2.4).

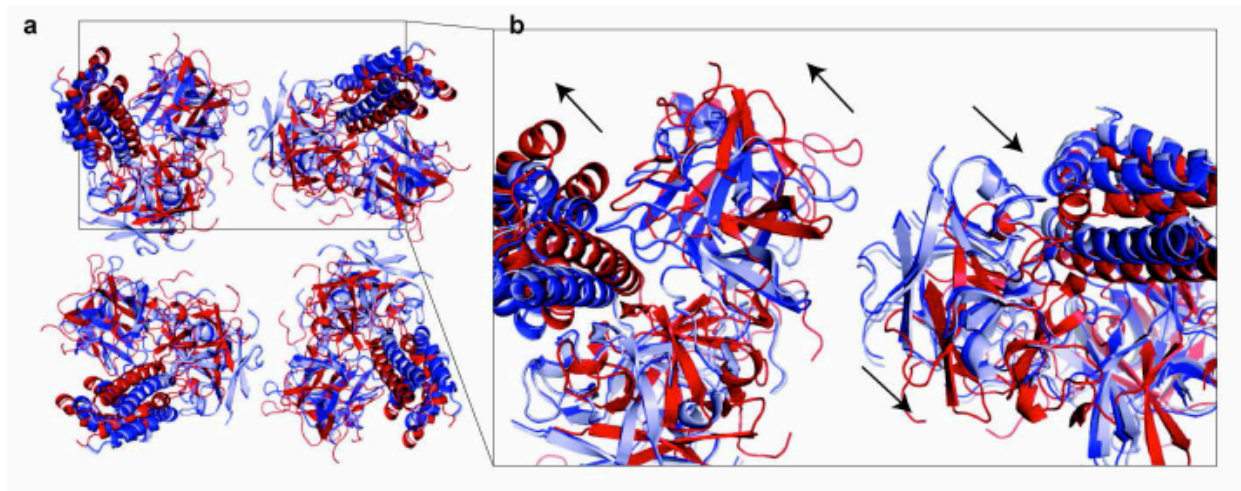


Figure 2.4: RyR1ABC docking results for different cryo-EM maps. (a) Comparison of docking results for RyR1ABC into two different closed RyR1 maps(121,122) (EMDB accession code 1606 – dark blue; EMDB accession code 5014 – light blue) shows a near perfect superposition, indicating that the results for the closed maps are consistent, with near identical intersubunit arrangements. The result for docking into the $\sim 10\text{\AA}$ map(119) (EMDB accession code 1275 – red) shows increased intersubunit distances like in the open RyR1 map(122) (EMDB accession code 1607) (Figure 2.2). Initially presumed to represent a closed state, it was later suggested that EMDB1275 may rather represent an open RyR1, or a mixture of different states(122). The increased intersubunit distances for docking in EMDB1275 would support this assumption. **(b)** Close-up view with arrows indicating the shifts that the models undergo from EMDB1606 to EMDB1275.

Many mutations were previously found at interfaces involving domains A, B, and C within a single subunit(208). Could these interfaces also be disrupted as part of channel opening, and could those disease mutations, therefore, also facilitate channel opening? A direct superposition of domain A of the open- and closed-state models shows that the intrasubunit

domain-domain movements would be subtler (Figure 2.3b), with shifts of domains B and C relative to domain A of $\sim 2\text{-}3\text{\AA}$, which are too small to be interpreted at the given resolution of the cryo-EM maps. Because there do not seem to be major relative movements at the intrasubunit interfaces upon opening, we decided to further investigate disease-associated mutations at the various intrasubunit interfaces between domains A, B, and C.

2.2.2 Disease mutations can weaken the thermal stability

MH is the result of increased sensitivity of RyR1 to halogenated anesthetics. In addition, many mutations in RyR1 have also been associated with increased temperature sensitivity and may underlie environmental heat stroke(57,247-253). We prepared nine different disease-associated mutants of RyR1ABC, all of which are associated with a gain-of-function phenotype (Table 2.2). They are located at interfaces between domains A, B, and C or are buried within individual domains (Figure 2.5a). Other RyR1 mutations located at the periphery of the hot spot were not included, as their effect would only become clear in the presence of neighboring domains. Thermal stability measurements show that wild-type RyR1ABC has a melting temperature of $\sim 47^{\circ}\text{C}$, and several (but not all) mutations lowered the thermal stability, with a maximum effect of $>9^{\circ}\text{C}$ destabilization for the C36R mutant (Figure 2.5b,c). The lowered stability of some RyR1 mutations may directly underlie a temperature-sensitive phenotype. For example, the R402C mutation (rabbit RyR1 numbering), which is similar to the R402G mutation that destabilizes the hot spot by $>5^{\circ}\text{C}$, has been associated with rhabdomyolysis triggered by exercise in hot weather(254).

Table 2.2: Summary of functional characterizations of the mutants studied. Summary of functional characterizations of the mutants studied in this report, along with references for identification and characterization. All mutants are associated with malignant hyperthermia (MH), which is known to cause gain-of-function phenotype in RyR1. Not all mutants have been functionally characterized (indicated by “n/a”). Residue numbering is for rabbit RyR1. CCD = central core disease. MmD = multi-minicore disease.

Mutation	Disease phenotype(s)	Primary identification references	Functional characterizations	Functional studies references
L14R	MH	(255)	Abnormally enhanced Ca ²⁺ -induced Ca ²⁺ release.	(255)
C36R	MH	(256)	Increased sensitivity to activation by caffeine and halothane.	(71,74,256)
R45C	MH	(257)	Increased sensitivity to activation by caffeine and 4-CmC.	(257,258)
D61N	MH/CCD	(40,259)	Assumed increased sensitivity to activation by halothane, due to MH phenotype.	n/a
G216E	MH/CCD/MmD	(260,261)	Assumed increased sensitivity to halothane, due to MH phenotype.	n/a
V219I	MH	(255)	Enhanced Ca ²⁺ -induced Ca ²⁺ release.	(255)
G249R	MH	(262)	Increased sensitivity to activation by caffeine, halothane, 4-CmC, and Ca ²⁺ . Decreased sensitivity to inactivation by Mg ²⁺ .	(71,74,97)
R402G	MH	(40)	Assumed increased sensitivity to halothane, due to MH phenotype.	n/a
I404M	MH/CCD	(263)	Increased sensitivity to activation by caffeine, halothane, and depolarization.	(68,71,74)

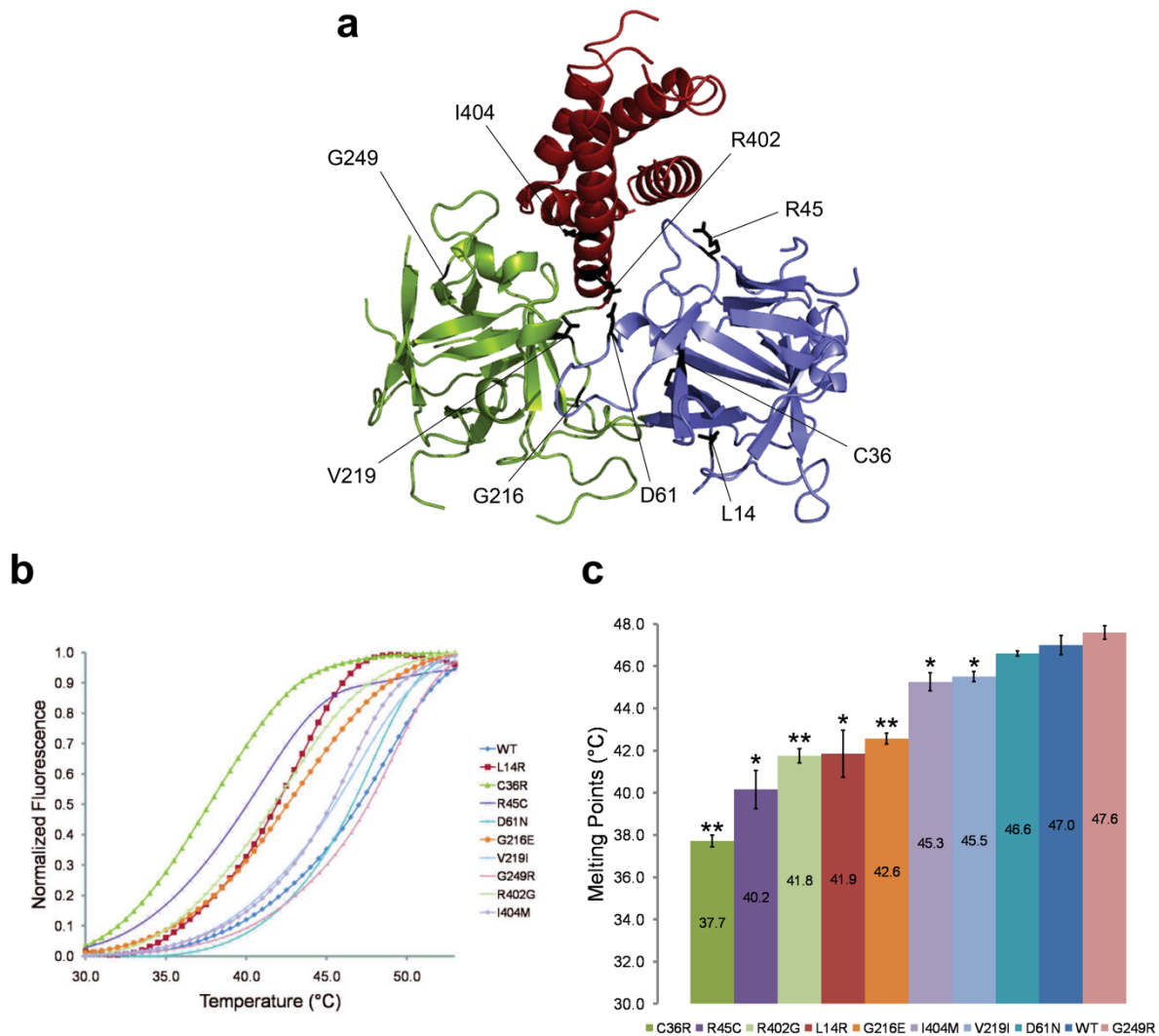


Figure 2.5: Thermal melt analysis. (a) Overview of the positions of the nine different mutations included in the thermal melt study. (b) Melting curves for the wild-type RyR1ABC and disease-associated mutants using thermofluor experiments. The curves are the average of four measurements. The melting temperatures are defined as the midpoints of each transition. (c) Average melting temperatures (n=4). The error bar indicates the standard deviation. Statistical analysis was performed using two-tailed, paired Student's *t*-test. **p* < 0.02 and ***p* < 0.001. The actual *p*-values (for comparison with wild type) are: C36R (3.3×10^{-5}), R45C (0.0016), R402G (8.2×10^{-4}), L14R (0.0029), G216E (6.2×10^{-4}), I404M (0.0073), V219I (0.019), D61N (0.20), and G249R (0.17).

2.2.3 Buried disease mutations affect the intersubunit interface

A small number of disease mutations are buried within individual domains. We analyzed the effect of three such mutations (L14R, G216E, and G249R) on the structure of the N-terminal disease hot spot. The G216E mutant expressed well with an intermediate destabilization (Figure 2.5b,c) but did not crystallize. The Gly216 C_α atom is buried within domain B, and a Glu216 side chain would clash with a neighboring β strand (β16). The inability to crystallize suggests that the structural changes are quite substantial. However, as circular dichroic (CD) spectra of wild type and mutant are clearly identical (Figure 2.6), the changes do not seem to involve secondary structure content but instead may include relative domain movements or increased flexibility.

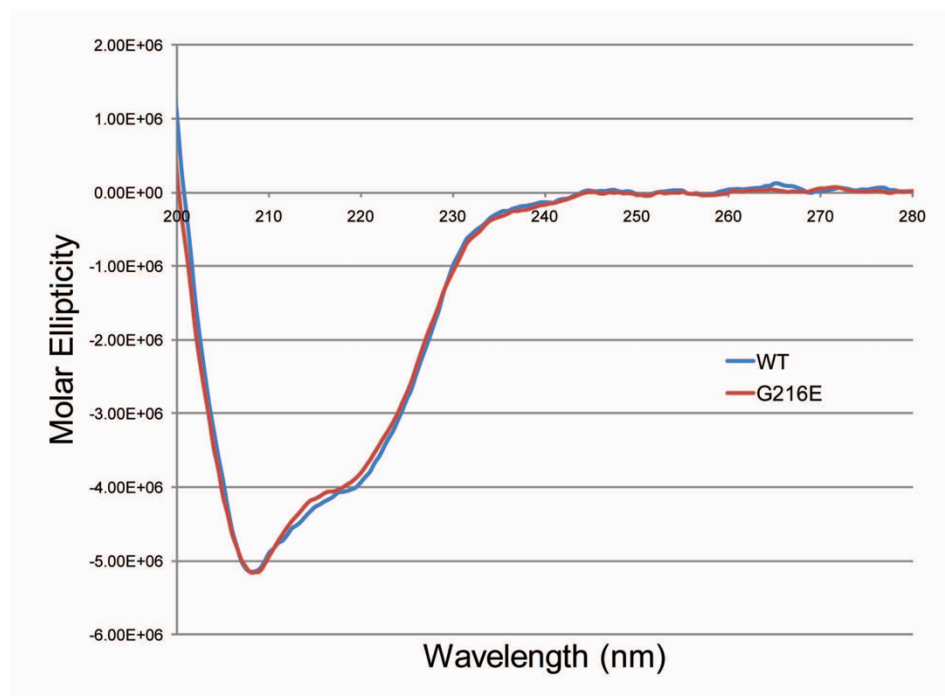


Figure 2.6: Circular dichroic (CD) spectra of G216E. The CD spectra for wild type and G216E RyR1ABC are very similar, suggesting that the disease mutation does not lead to changes in the overall secondary structure content. This suggests that the inability of G216E to crystallize is likely due to relative domain movements or a generally increased flexibility of the domains relative to one another.

The G249R mutant introduces a bulky Arg side chain within a buried region of domain B (Figure 2.7a). Its thermal stability is not altered significantly (Figure 2.5b,c), but the mutant displaces the neighboring side chains of Glu229 and Leu372. In addition, the neighboring loop 226-229 (Figure 2.7a, red), which is partially disordered in the wild-type structure has an altered conformation and is now completely visible. This loop harbors the positions of four different disease mutations (including Glu229) in RyR1 and RyR2 combined and is located at the intersubunit interface 1 between two neighboring ABC structures.

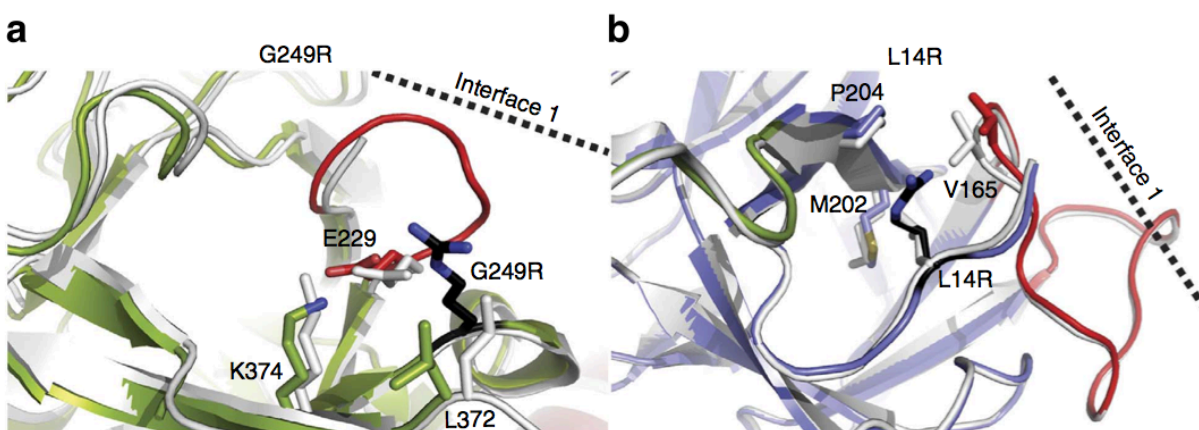


Figure 2.7: Buried disease mutations. Superposition of the wild-type (white) and mutant (colors) structures for (a) G249R (PDB accession code 4I1E) and (b) L14R (PDB accession code 4I7I). Domain A (blue) and domain B, (green). The mutated residues are shown in black. Loops directly located at interface 1 are shown in red.

L14R introduces a charged residue in a small hydrophobic core near the very amino terminus, including Val165, Met202, and Pro204 (Figure 2.7b). The mutation displaces the main chain and side chain of Val165, which is located on the $\beta 8$ - $\beta 9$ loop of domain A, also located at interface 1. Although L14R and G249R represent buried mutations, they both seem to affect an interface that is altered upon channel opening.

2.2.4 Salt-bridge mutations cause relative domain-domain movements

Three RyR1 mutants (R45C, D61N, and R402G) target ionic pairs between domains A and C. They cause the largest structural changes, evoking relative domain-domain movements. R45C breaks a salt bridge with Asp447 on domain C. This causes the Asp447 side chain to become unstructured, and domain C to pivot with displacements up to $\sim 3\text{\AA}$ near the cytoplasmic side of the helical bundle (Figure 2.8a,b).

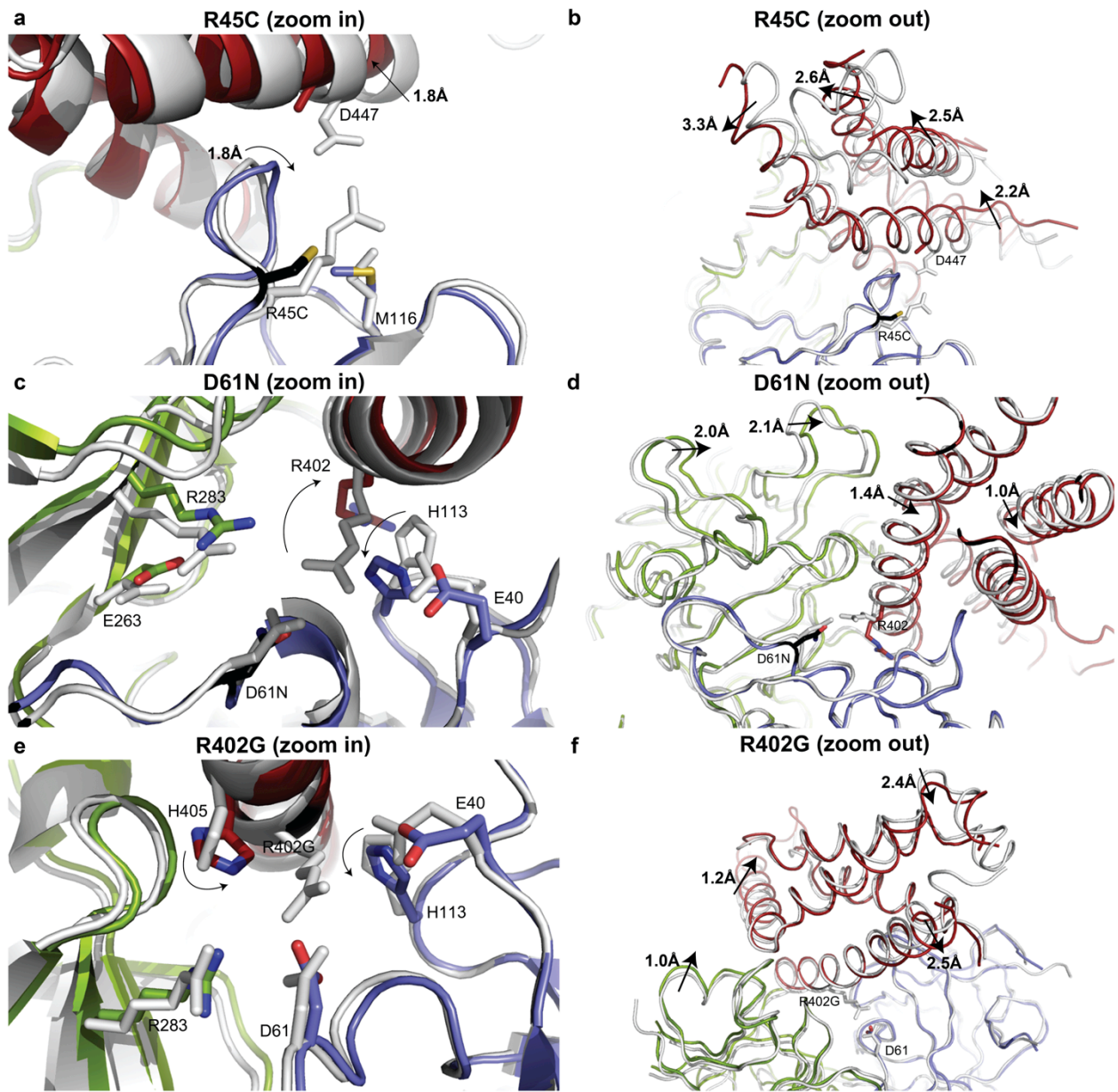


Figure 2.8: Disease mutation affecting interdomain ionic pairs. (a,b) R45C (PDB accession code 4I6I). (c,d) D61N (PDB accession code 4I3N). (e,f) R402G (PDB accession code 4I37). Domain A (blue), domain B (green), and domain C (red). Superpositions with the wildtype structure (white). All superpositions are based on domain A. Arrows indicate changes relative to the wild-type structure. R45C and R402G are in comparison with the wild-type structure crystallized in PA5100.

Both Asp61 and Arg402 are involved in a salt bridge, together with Glu40. The D61N mutation is isosteric, neutralizing a negative charge (Figure 2.8c). This causes a complete disruption of the ionic pair network, with Arg402 swinging away, breaking the interactions with both Asn61 and Glu40, and causing a relative change in the orientation of domain C with displacement close to 1Å. In domain B, Arg283 is no longer attracted to the negatively charged Asp61, causing a relative reorientation of the domains with shifts ~2Å (Figure 2.8d). The R402G mutation disrupts the same ionic pair network. His113 and His405 close the gap created by taking away the long Arg side chain (Figure 2.8e), and the domain C backbone has shifted by up to ~2.5Å relative to domain A (Figure 2.8f).

Although domains A, B, and C interact through multiple ionic pairs, disruption of even single ones is sufficient to cause relative domain reorientations. This shows how mutations located at the interfaces between domains A, B, and C can affect regions at the periphery of the hot spot. Keeping domain C fixed, for example, the mutations would affect the positions of domain A and B, and hence, again, the intersubunit interface 1.

2.2.5 Uncharged mutations at the A-B-C interfaces cause local changes

We looked at the effect of three additional mutants at the intrasubunit interfaces between domains A, B, and C that do not disrupt ionic pairs (C36R, V219I, and I404M). The C36R mutant caused the largest effect on the melting temperature (Figure 2.5b,c). Cys36 is located at the surface of domain A and has only minor effects on the structure of domain A in isolation(205). However, it is buried at the interface between domains A and B, and a direct placement of an Arg residue would clash with domain B. The mutation has several profound effects on the structure. First, a neighboring loop in domain A (residues 52-60) moves ~2Å to allow the Arg36 side chain to fit in a folded, rather than an extended, conformation (Figure 2.9a).

This prevents a direct clash with domain B, but the moving loop contains several contact points with domain B in the wild-type structure, and thus affects the domains A-B interface. The Gln23 and Asn203 side chains move towards the Arg36. The altered Asn203 side-chain conformation, together with the longer Arg36 side chain, cause the neighboring domain B loop to be displaced by $\sim 1\text{\AA}$. All together, these significantly affect the A-B interface, destabilizing the RyR1ABC protein by $>9^\circ\text{C}$ (Figure 2.5b,c).

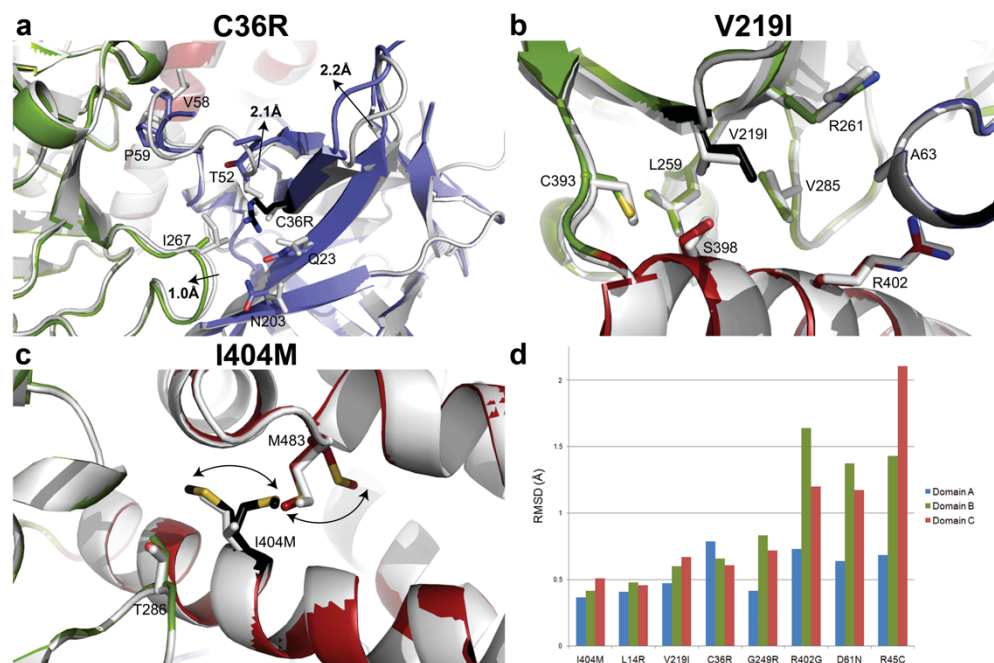


Figure 2.9: Other mutations at the intrasubunit interfaces between different domains. (a) C36R (PDB accession code 4I0Y). **(b)** V219I (PDB accession code 4I8M). **(c)** I404M (PDB accession code 4I2S). Superposition with the wildtype and color scheme as in Figure 2.8. For I404M, dual conformations were observed in the electron density. Arrows indicate changes relative to the wild-type structure. **(d)** RMSD values for superposition of the mutants with the wild-type structure. The superposition is performed based on domain A, so the values for domains B and C are the sum of intrinsic structural differences within the domains and relative domain reorientations compared with the wild-type structure. R402G and R45C are in comparison with the wild-type structure crystallized in PA5100.

The V219I mutation is located at the B-C interface and is very subtle, as it only introduces a single methyl group. It is surrounded by mostly hydrophobic residues, but no appreciable effect is seen on the structure (Figure 2.9b). The only effect could be that the hydrophobic packing is less-than-ideal, but as expected, the effect on the thermal melting is also minimal (Figure 2.5b,c).

The I404M mutation is near the B-C interface. This mutation causes a clash with Met483 in domain C. As a result, both Met404 and Met483 adopt dual conformations. (Figure 2.9c). The branched C_γ atom of Ile404 is in the van der Waals contact with Thr286 on domain B in the wild-type structure. These changes result in a relatively small drop (~2°C) in the melting temperature (Figure 2.5b,c).

Figure 2.9d shows the root mean square deviation (RMSD) values for each domain, after superposing the modeled C_α atoms in domain A. The values for domains B and C thus also indicate their degree of movement relative to domain A. Overall, the V219I and I404M mutants are predicted to have the smallest functional impact, as these mutants do not cause large structural changes and have only modest effects on the melting temperatures. Most mutants crystallized in the same condition reported for wild-type RyR1ABC(208), but two of them, R45C and R402G, crystallized in different conditions involving a polyacrylic acid (PA5100). We also crystallized the wild-type protein in PA5100, which was at lower resolution (3.5Å) but allowed us to investigate the relative domain orientations. The RMSD values and figures for the R45C and R402G superpositions are based on comparison with the wild-type protein in PA5100, showing that the conformational changes are due to the mutations, and not the crystallization conditions. None of the observed conformational differences are due to pH changes (Figure 2.10).

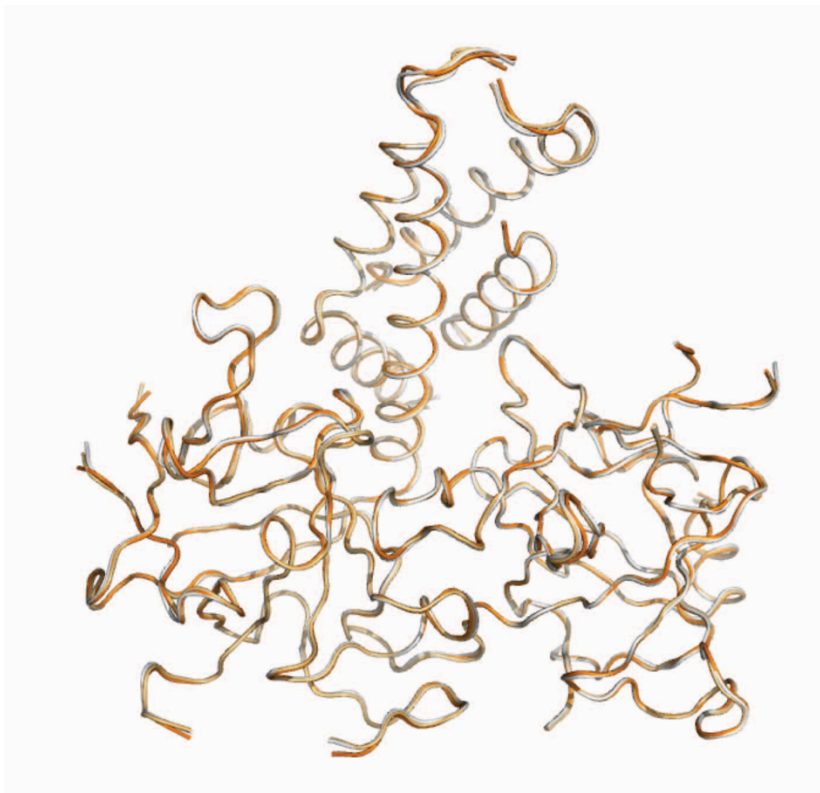


Figure 2.10: Domain reorientations are not due to pH differences. RyR1ABC wild-type structures crystallized at pH 8.0 (white), pH 9.0 (cream), and pH 9.5 (orange) are superposed, based on domain A. The positions of domains B and C relative to domain A are unchanged, indicating that the changes observed for the disease-associated mutants are not due to pH differences in the crystallization conditions.

2.2.6 The relative orientation of domains B and C

As breaking favorable interactions between domains A-B or A-C causes relative domain reorientations, we wondered whether the destabilization simply allows a preferred relative orientation between domains B and C. In this scheme, domain A would act as a “clamp” that prevents the most favorable interactions between domains B and C. This situation is then analogous to IP₃ receptors, where domain A, also known as the suppressor domain, decreases the ligand-binding affinity by clamping domains B and C in a conformation that disfavors IP₃ binding(231,234-236). We, therefore, solved the structure of domains B and C in the absence of

domain A. Superposition of domain B shows that the relative orientation of domain C differs appreciably between the RyR1ABC and RyR1BC crystal structures (Figure 2.11). In the absence of domain A, domain C swings towards the position of domain A, showing that domain A prevents a more favorable interaction between domains B and C through steric hindrance. The results suggest that weakening the A-C interaction through disease mutations allows more favorable B-C interactions to occur. However, the disease mutations cannot cause the exact same B-C reorientation because domain A still provides steric hindrance.

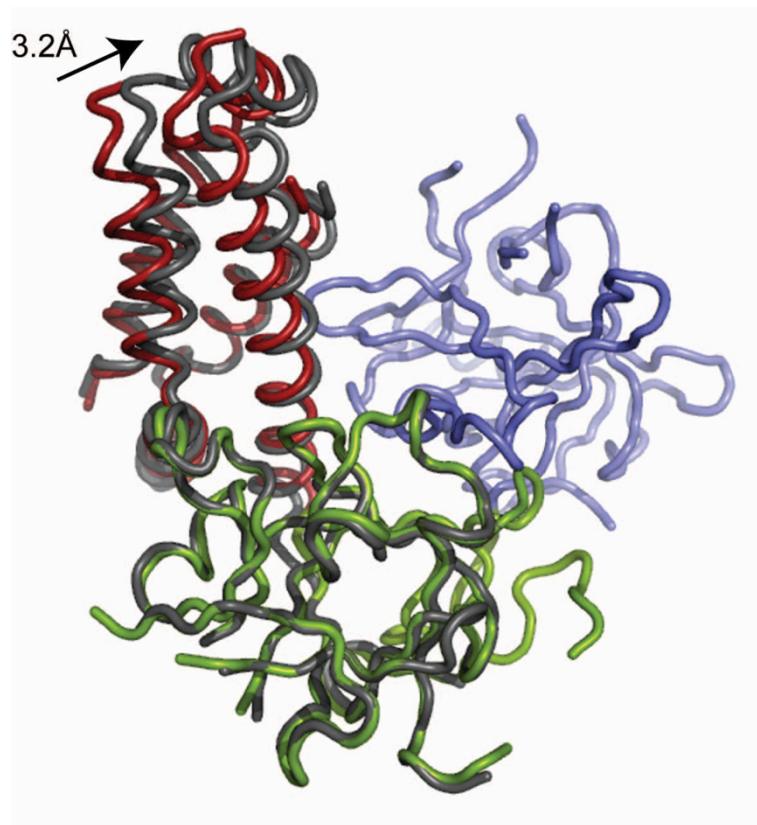


Figure 2.11: The clamping action of domain A. Superposition of domains B of the RyR1BC and RyR1ABC crystal structures, showing the relative conformational changes of domain C (arrow). Gray: RyR1BC (PDB accession code 4I96). Colors: RyR1ABC domains A (blue), B (green), and C (red).

2.3 Discussion

RyRs are allosteric membrane proteins, whose major function is to release Ca^{2+} from the endoplasmic or sarcoplasmic reticulum. Primary triggers for channel opening include cytoplasmic and luminal Ca^{2+} , as well as voltage-dependent conformational changes in the L-type calcium channel $\text{Ca}_v1.1$. These likely cause channel opening by stabilizing the open-state or destabilizing the closed-state conformations of the cytoplasmic portion.

Disease-causing mutations in RyR1 and RyR2 interfere with channel gating. With some exceptions, most mutants have been associated with a gain-of-function, for example, by lowering the threshold for activating ligands. Several theories have been put forward to explain their effect. In the “zipper hypothesis,” it was postulated that the N-terminal and central disease hot spots interact, and that disease mutations are located at their interface(148). However, it is now clear that most disease mutations in the N-terminal region are already involved with other domain-domain interfaces, and only a small fraction could remain available for binding the central hot spot(208). It was also postulated that the mutations may affect the binding of FK506-binding proteins (FKBPs), and that the resultant dissociation facilitates channel opening(171,264-266). One group suggested that the N-terminal region might interact directly with FKBPs(120), but our isothermal titration calorimetry (ITC) experiments failed to detect any appreciable binding. This is in agreement with cryo-EM studies showing that FKBPs bind at the periphery of the cytoplasmic foot (for example, see Samso *et al.*(178), far away from the docked position of the N-terminal disease hot spot.

Here we built pseudo-atomic models of the N-terminal region in the open and closed states of RyR1, which suggest that channel opening results in $\sim 7\text{\AA}$ widening of an intersubunit contact area at the central rim. A recent study also supports this result, where FRET experiments

between domains B and C of the full-length RyR2 validated the docked positions and revealed dynamic conformational changes within the N-terminal region(239). One likely interpretation of the widening of the intersubunit interface is that there are direct contacts between domains A and B of the neighboring subunits in the closed state, and that those contacts are disrupted or drastically altered as the channel opens. The interaction thus serves as a “brake” on channel opening, imposing an energetic barrier that needs to be overcome to allow channel opening (Figure 2.13). This energy would be delivered by binding of triggering agents, such as Ca^{2+} , which likely cause long-range conformational changes that couple allosterically to the N-terminal region. This also implies that the contacts must be extremely weak: a high-affinity interaction would require an extremely high energetic penalty for the disruption, as the effective concentration of two juxtaposed segments within a macromolecule can be in the molar range(267). Indeed, using various approaches (pull-down experiments, cross-linking, gel filtration chromatography, dynamic light scattering, and ITC), we failed to observe any interactions between individual RyR1ABC monomers in solution, implying that they do not drive tetramerization. The latter was shown to be mediated by the C-terminal area, which contains coiled-coil region(268). The proposed intersubunit interactions in the N-terminal region can, therefore, only arise in the context of a high effective concentration. The same applies to interactions between domain A and domains BC within a subunit, as the two separately purified constructs also failed to show any interaction in solution, despite their unambiguous contacts in the crystal structures.

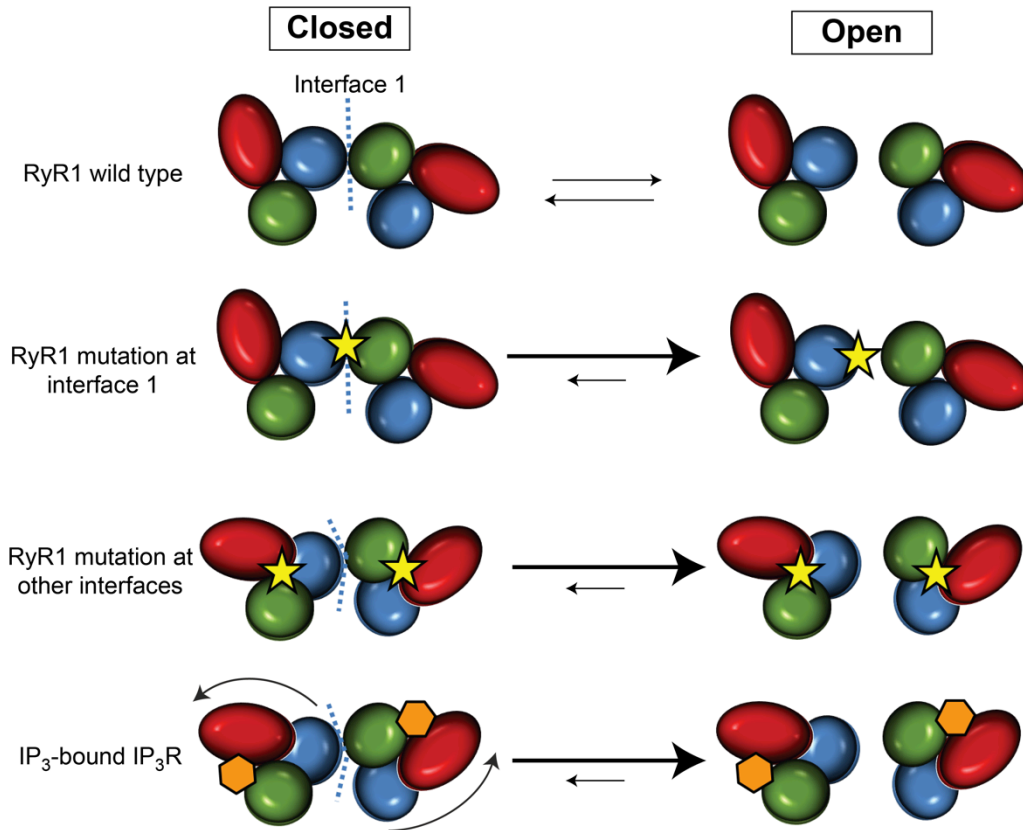


Figure 2.12: Model for the effect of N-terminal disease-associated mutations in RyRs and ligand binding in IP₃Rs. In wild-type RyR1, channel opening requires breaking the interaction along interface 1 between two neighboring N-terminal disease hot spots. This involves an energetic penalty. Disease-associated mutations directly at interface 1 weaken the interaction, which reduces the energetic penalty and facilitates channel opening. Some disease-associated mutations within a hot spot can change the relative domain-domain orientations, thus affecting other interfaces at the periphery of the hot spot, such as interface 1. These long-range structural changes, therefore, also facilitate channel opening. In IP₃R, binding of IP₃ (hexagon) results in relative domain reorientations, which also affects interface 1 and facilitates channel opening.

Incidentally, the intersubunit contact area between domains A and B contains the largest cluster of disease mutations within the N-terminal region (20 for RyR1 and RyR2 combined) (Figure 2.3a), all of which are associated with gain-of-function phenotypes (MH and CPVT)(208). How could these affect channel opening? Mutations in the domain A β 8- β 9 loop,

one of the loops located at the contact region, were previously found not to cause any structural or stability differences(205,206). This implies that their only possible involvement is to be located at a functional interface, and we propose that they form part of intersubunit interactions that are disrupted upon channel opening. When a random disease mutation is introduced, there is a much higher probability that the mutation will weaken, rather than strengthen intersubunit contacts. Such mutations will lower the energy barrier to open the channel, which in turn facilitates channel opening (Figure 2.13). Important to point out is that they do not cause channel opening on their own. They simply weaken the “brake” on channel opening, and some amount of energy, albeit less, is still needed through binding of triggering agents. This can, for example, explain the shift in Ca^{2+} dependence and voltage dependence of channel opening(269,270).

Many mutations are not located at the intersubunit interface. However, we previously observed that most mutations in the N-terminal disease hot spot are located at the domain-domain interfaces, including the interfaces between domains A, B, and C within individual subunits(208). We found that several mutations that disrupt salt bridges between domains A and C can cause relative domain movements. Therefore, such mutations cause long-range structural changes, which automatically affect the interfaces at the periphery of these domains. One straightforward interpretation is that this domain “misalignment” also affects the intersubunit interface 1, and thus also lowers the energetic barrier to open the channel (Figure 2.13). In full-length RyRs, the relative domain orientation could be stabilized by the surrounding domains. However, even if the ABC domains have the wild-type orientation in full-length RyR mutants, there is now an additional strain on the other interfaces to keep the ABC domains in a wild-type orientation, away from their favored orientation in isolation, thus reducing the stability of the closed state. Upon channel opening, the mutant ABC domains can then relax back to their

favored orientation. The closed state is thus destabilized relative to the open state, resulting in facilitated channel opening.

Mutations that are buried (G249R and L14R) also seem to affect the intersubunit interface through conformational changes that couple within the protein. These results highlight the overall importance of this interface in channel opening.

Finally, some mutations did not seem to cause any large structural changes, but only had an effect on the thermal stability (V219I and I404M). The largest effect was observed for the C36R mutation, destabilizing the RyR1ABC protein by $>9^{\circ}\text{C}$ (Figure 2.5b,c). The altered melting temperatures imply that there may be temperature-dependent conformational changes, which could then also affect one or more individual domain interactions.

The RyR N-terminal region shares $\sim 21\%$ sequence identity with the corresponding region in IP₃Rs, suggesting that both channels may have adopted similar allosteric strategies(236). In IP₃Rs, the N-terminal domain A is also known as the “suppressor” domain, which lowers the affinity for IP₃ by clamping domains B and C in a conformation that is unfavorable for IP₃ binding(231). Importantly, domain-domain reorientations have also been observed in IP₃RABC through binding of IP₃(234,235), suggesting a common theme in both types of calcium-release channels (Figure 2.13). In RyRs, the relative domain orientation can be altered permanently through a disease mutation, whereas in IP₃Rs, the reorientation is reversible through binding and unbinding of IP₃(234,235). The IP₃RABC domains also dock near the four-fold symmetry axis of a reported 9.5Å IP₃R cryo-EM map(229), making intersubunit contacts that are very similar to the RyR1ABC interactions(234). It has been suggested before that IP₃ binding may also rearrange the intersubunit interface(234). Future cryo-EM studies comparing open and closed IP₃Rs may show a similar widening of the intersubunit gaps. Whether an activator can bind the

RyR N-terminal region and cause domain rearrangements similar to IP₃ in IP₃Rs remains to be discovered.

Chapter 3: The cardiac ryanodine receptor N-terminal domain contains a hot spot loop that is perturbed by disease-causing mutations

Dysfunction of ryanodine receptors (RyRs) through mutations has devastating consequences, leading to life-threatening diseases. RyR2 is the target for over 150 mutations, many of which are associated with catecholaminergic polymorphic ventricular tachycardia (CPVT) that can result in sudden cardiac death(17). Other conditions linked to mutations in RyR2 include arrhythmogenic right ventricular dysplasia type 2 (ARVD2) and idiopathic ventricular fibrillation(18). Most disease-associated mutations render gain of function, increasing the sensitivity of the channel towards stimuli, such as cytosolic or luminal Ca^{2+} .

Several structural studies of RyRs have provided insights into how disease-associated mutations affect the channel function(238). In particular, the crystal structure of the N-terminal region of RyR1 (RyR1ABC), that comprises of three domains and forms a cytoplasmic vestibule in an intact channel, has shown that the mutations are either clustered at interfaces or are buried, rather than exposed to the surface of the full-length channel(208). Further investigation of RyR1ABC docked in the closed and open cryo-EM maps led to a model of channel gating whereby an intersubunit interface, normally serving as a brake, is broken upon channel opening(209). This interface between domains A and B across the subunit (“interface 1”) harbors the largest number of disease-associated mutations in the N-terminal region, further highlighting its key role in the channel gating. In particular, the $\beta 8$ - $\beta 9$ loop found at interface 1, also called the “hot spot” loop (HS-loop), is the target for over half the mutations found within domain A. Crystal structures have been solved for domain A in both RyR1(205,206) and RyR2(206). The

structural effect of two mutants in the HS-loop of RyR1A (R164C and R178C, rabbit RyR1 numbering) have been probed through solution NMR, which showed no overall structural perturbation(205). Despite being the prime target for disease-associated mutations and its critical location at interface 1 that acts as a brake in channel opening, no structural insight has been available for the HS-loop mutants in RyR2. Here, we provide the crystal structures of three HS-loop mutants in RyR2A: P164S, R169Q, and R176Q (mouse RyR2 numbering).

3.1 Methods

3.1.1 Cloning, expression, and purification

Mouse RyR2 (residues 1–217) was cloned into a modified pET28 vector containing, in tandem, a His-tag, maltose binding protein (MBP), and a tobacco etch virus (TEV) cleavage site, followed by the construct of interest(271). The HS-loop mutants (P164S, R169Q, and R176Q) were made using the Quikchange protocol (Stratagene). Proteins were expressed at 37°C in *E. coli* Rosetta (DE3) pLacI strains (Novagen), induced at OD₆₀₀ of ~0.6 with 0.2mM IPTG, and then harvested after 4 hours. Cells were lysed via sonication in buffer A (250mM KCl and 10mM HEPES pH7.4), supplemented with 25mg mL⁻¹ DNaseI and 25mg mL⁻¹ lysozyme. The resulting lysate was applied to a PorosMC column (Tosoh Biosep), washed with 5 column volumes (CV) of buffer A and 5CV of buffer A and 10mM imidazole, and eluted with buffer B (250mM KCl and 500mM imidazole pH7.4). The protein was dialyzed overnight against buffer A, while cleaved simultaneously with recombinant TEV protease. The sample was then run on another PorosMC column in buffer A, and the flowthrough was collected and dialyzed against buffer C (10mM KCl and 20mM Tris-Cl pH8.8), applied to a ResourceQ column (GE Healthcare), and eluted with a gradient from 0% to 40% buffer D (1M KCl and 20mM Tris-Cl pH8.8). Finally, the protein was run on a Superdex200 (GE Healthcare) gel filtration column in

buffer A. The protein sample was exchanged to 10mM KCl and 5mM HEPES pH7.4, concentrated to 10-20mg mL⁻¹ using Amicon concentrators (10K MWCO; Millipore), and stored at -80°C.

3.1.2 Crystallization and data collection

All crystals were obtained by hanging drop vapor diffusion using 0.1M malonate (pH 4.6–4.9) and 5%-20% saturated (NH₄)₂SO₄. Crystals were transferred to paratone oil and flash-frozen in liquid N₂ prior to data collection. The datasets were collected at the Stanford Synchrotron Radiation Lightsource (SSRL) beamline 11-1 and the Canadian Light Source (CLS) beamline 08ID-1 and were processed using the HKL2000 package (HKL Research). Molecular replacement was performed using Phaser(242) with a modified structure of RyR2A A77V (PDB accession code 3IM7) as a starting model, in which the HS-loop was deleted to remove bias. The models were completed by successive rounds of manual model building in Coot(243,272) and refinement with PHENIX(273). The coordinates and structure factors have been deposited in the Research Collaboratory for Structural Bioinformatics database with PDB accession codes 4KEI (P164S), 4KEJ (R169Q), and 4KEK (R176Q). Data collection and final refinement statistics are available in Table 3.1.

Table 3.1: Data collection and refinement statistics. Values in parentheses are for the highest resolution shell.

	P164S	R169Q	R176Q
Data collection			
Space group	<i>I</i> 41	<i>I</i> 41	<i>I</i> 41
Cell dimensions			
<i>a=b, c</i> (Å)	111.75, 37.82	112.86, 38.09	100.27, 37.99
<i>α=β=γ</i> (°)	90	90	90
Resolution (Å)	50-2.40 (2.49-2.49)	50-2.55 (2.64-2.55)	50-2.15 (2.19-2.15)

	P164S	R169Q	R176Q
R_{sym} or R_{merge}	5.9 (44.9)	9.3 (49.3)	6.1 (43.1)
I/σ	32.1 (2.5)	24.9 (2.3)	33.3 (2.1)
Completeness (%)	99.8 (98.4)	98.8 (90.0)	98.1 (86.0)
Redundancy	7.2 (5.5)	6.6 (3.3)	4.9 (2.4)
Refinement			
Resolution (Å)	50-2.40	50-2.55	50-2.15
No. reflections	8805	7484	9885
R_{work}/R_{free}	24.2/27.3	23.6/29.7	25.0/29.0
No. atoms			
Protein	1256	1264	1233
Ligand/ion	0	0	5
Water	15	19	14
B -factors			
Protein	61.6	47.3	51.1
Ligand/ion	N/A	N/A	61.8
Water	52.2	37.8	47.8
R.m.s. deviations			
Bond lengths (Å)	0.002	0.003	0.002
Bond angles (°)	0.554	0.696	0.649

3.2 Results

In order to investigate the structural impact of disease-associated mutations located within the hot spot (HS-)loop of RyR2, or the β 8- β 9 loop (residues 164-179 in mouse RyR2 numbering), we solved the crystal structures of RyR2A mutants (P164S, R169Q, and R176Q) to resolutions between 2.15 and 2.55Å (Table 3.1). Because the conformation of the loop might be affected by crystal contacts and the wild-type RyR2A structure was solved in a different space

group (C2), we compared these structures with the previously published A77V mutant(206), which crystallized in the same space group as the three HS-loop mutants in this study. The A77V mutation only affects the surface and is distantly located from the HS-loop, thus unlikely to impact the conformation of the loop.

The P164S and R169Q mutations are linked to CPVT, while the R176Q mutation is associated with ARVD2. Pro164 is located at the beginning of the HS-loop and presumably provides a degree of conformational rigidity to this loop. Mutating this residue to serine likely results in partial flexibility, as a portion of the loop exhibits weak electron density (Figure 3.1a,b). The side chain of Arg169 also appears inherently flexible with poorly defined electron density and was not modeled in the A77V structure. In the R169Q mutant structure, several residues, including Gln169, were not visible in the electron density, consistent with the higher degree of flexibility (Figure 3.1c,d). The R176Q mutation facilitates the formation of a new hydrogen bond between Gln176 and Arg169. This interaction also positions Arg169 for a salt bridge with Asp179 (Figure 3.1e,f). However, several neighboring residues still showed missing electron density, suggesting that the R176Q mutation, despite the formation of new interactions, destabilizes the loop.

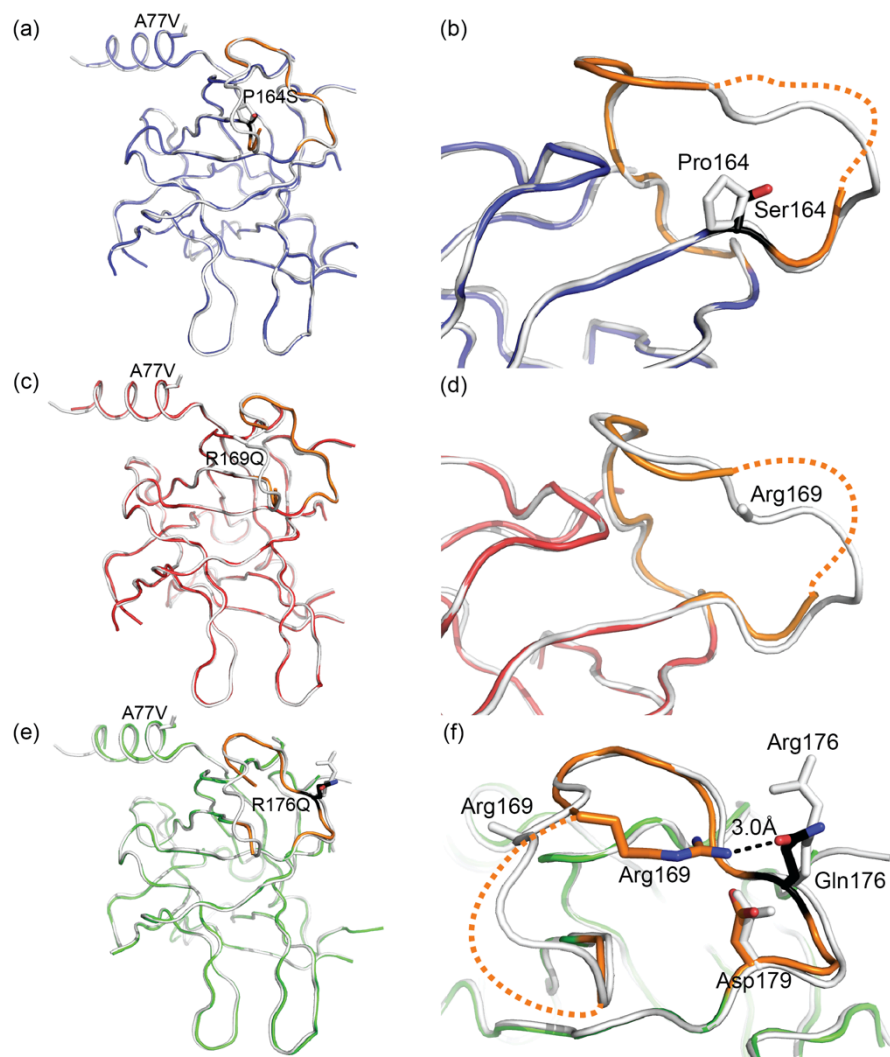


Figure 3.1: The RyR2A HS-loop mutant structures. Structures of mutants (colors) are superposed onto the RyR2A A77V structure (white). The HS-loop (residues 164-179) is highlighted in orange (respective mutant) and white (A77V). The site of mutation is shown in black. The dashed line indicates the portion of the loop that could not be modeled due to flexibility. **(a,b)** P164S (PDB accession code 4KEI). **(c,d)** R169Q (PDB accession code 4KEJ). **(e,f)** R176Q (PDB accession code 4KEK).

Although the HS-loops in the mutant structures appear partially flexible, as indicated by the poor electron density, crystal contacts may have affected the resolution of the loops. For example, in the wild-type RyR2A structure, which was crystallized in a different space group, the loop position is different from that of the A77V mutant structures(206) (Figure 3.2).

Although crystal contacts usually do not impart huge structural changes, the conformations of loops that are inherently flexible can be particularly sensitive. Therefore, we performed more detailed solution NMR experiments, in collaboration with the laboratory of Dr. Mitsuhiro Ikura (University of Toronto), to circumvent any effects by crystal contacts on the HS-loop properties.

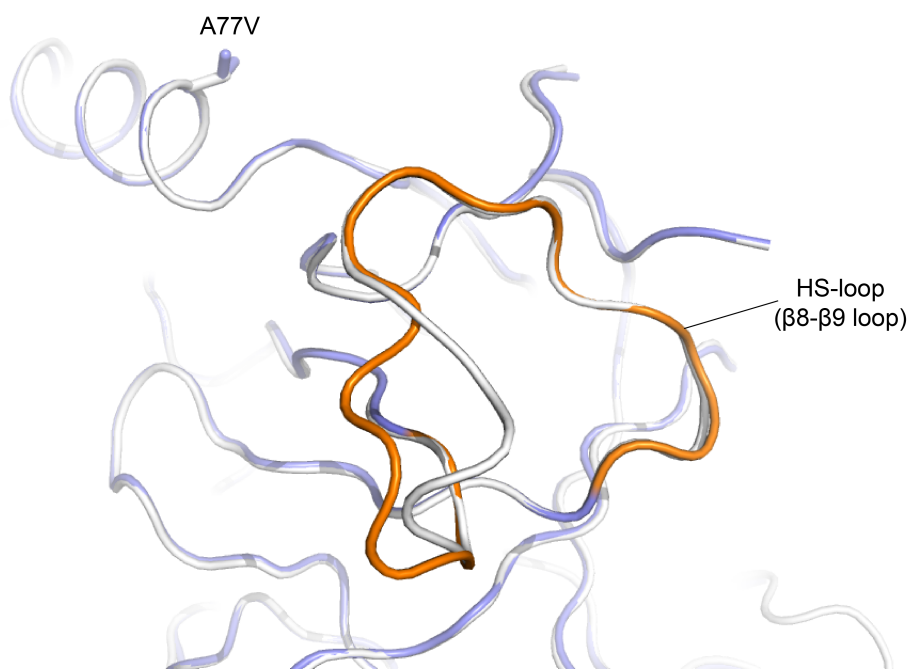


Figure 3.2: The HS-loop of RyR2A wild type and A77V mutant. The superposition of the RyR2A wild type chain B (white) (PDB accession code 3IM5) and RyR2A A77V (blue) (PDB accession code 3IM7) structures. The HS-loop of the A77V mutant is colored in orange for clarity. The structural difference in the loop is due to the different crystal contacts between the wild-type (space group $C2$; two molecules in the asymmetric unit) and A77V (space group $I41$; one molecule in the asymmetric unit) structures and not due to the mutation since the A77V mutation only alters the surface of the mutation site, and residue 77 is not involved in contact with the HS-loop.

The spectra of the P164S, R169Q, and R176Q mutants were assigned by transference from wild-type RyR2A and using ^{15}N -resolved nuclear Overhauser enhancement (NOE) spectroscopy-TROSY data for peaks that did not coincide sufficiently between spectra. We examined the effect of the three HS-loop mutations on the structural fold of RyR2A by

monitoring the chemical shift perturbations (CSPs) (Figure 3.3a). Plotting the CSPs on the hybrid structure of RyR2A revealed distinct magnitudes of structural perturbations caused by each mutation (Figure 3.3b). The P164S mutation resulted in the largest CSPs for residues throughout the HS-loop and for residues immediately adjacent to the loop. The R169Q mutation had a moderate conformational effect on the HS-loop and the core structure, while the perturbation of R176Q was limited to the immediate vicinity of the substituted residue. Taken together, the data suggest that P164S, R169Q, and R176Q cause local structural perturbations within or near the HS-loop, overall consistent with the crystal structures.

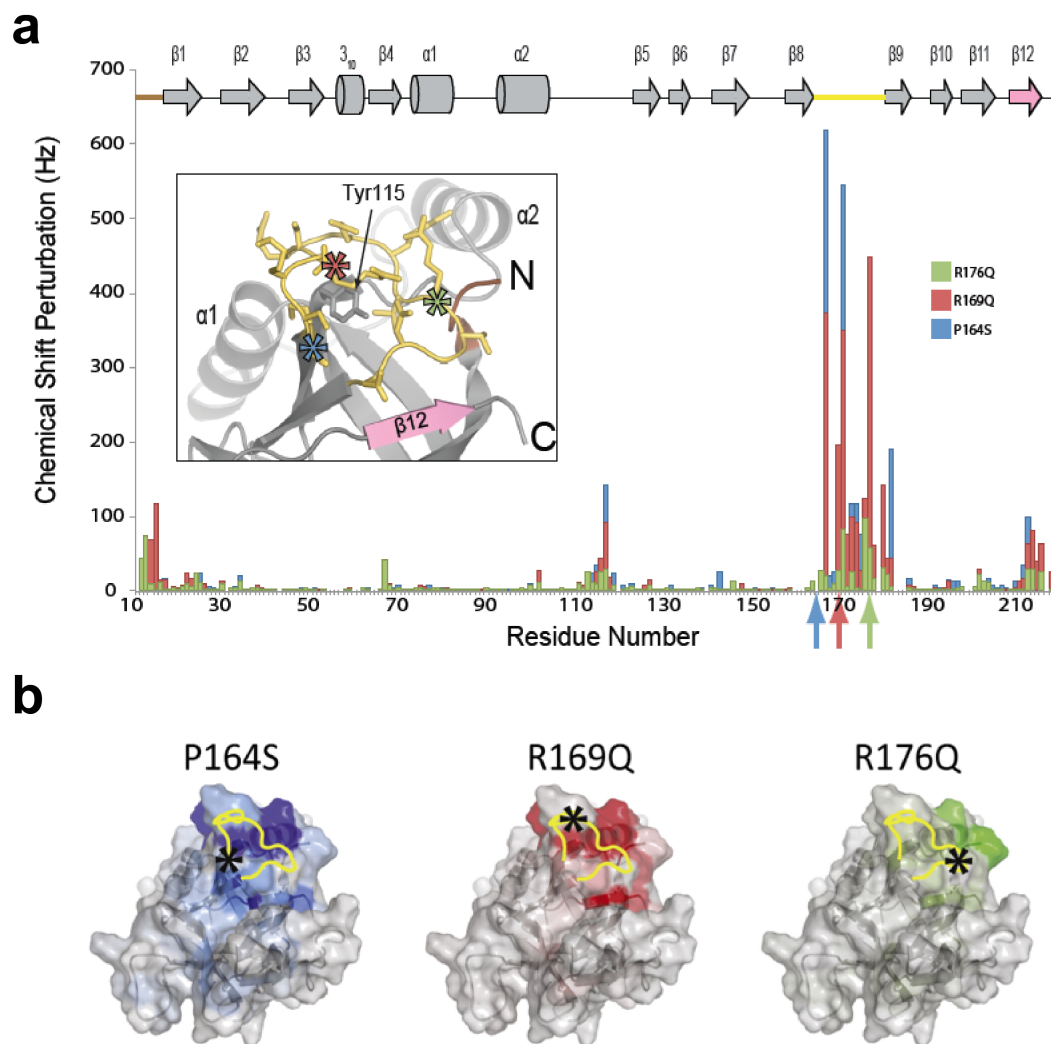


Figure 3.3: Chemical shift perturbations (CSPs) on RyR2A caused by the HS-loop mutants. (a) CSPs of RyR2A TROSY-HSQC. CSP values in Hz are plotted for each mutant. Colored arrows indicate the site of mutations in the sequence. Secondary structural elements for RyR2A are shown above the plot. Regions outside the HS-loop showing significant CSPs are the N-terminal region and β 12, colored in brown and pink, respectively. The boxed inset is a close-up view of the HS-loop region showing the site of mutations (in asterisks) and perturbed structural elements including Tyr115, which fits into a cleft of the HS-loop, as well as the aforementioned N-terminus and β 12. **(b)** CSPs generated by each HS-loop mutant are mapped onto the hybrid model of RyR2A. The P164S, R169Q, and R176Q perturbations are shown in blue, red, and green, respectively. The HS-loop is outlined in yellow. An asterisk shows the site of each mutation. Image provided by the Ikura Lab.

3.3 Discussion

RyRs are large tetrameric Ca^{2+} release channels located in the membranes of the SR or ER. Previous low-resolution structural studies of the channel revealed an overall mushroom shape, comprised of many globular domains(238). Some of the domains are involved in the binding of modulatory proteins or ligands, while others are coupled to conformational changes connecting the movements in the transmembrane area to the cytoplasmic region(27). Each subunit consists of many domains that have individual functions(27). RyRs are the target for over 500 disease-associated mutations. In particular, the N-terminal region of RyR1 and RyR2 has been described as a “hot spot” for mutations that cause MH, CCD, CPVT, and other conditions, although the number of mutations identified outside of the hot spots are increasing, especially for RyR1 (Figure 1.2). Understanding of the mechanisms of these disease-associated mutations, as well as the exact nature of the conformational changes that regulates the channel opening, has been hampered due to the lack of high-resolution structures of RyRs.

The first crystal structures to be solved for RyRs were that of the very N-terminal domain of RyR1 and RyR2, or RyR1A and RyR2A(205,206). The domain consisted of a β -trefoil core and an α helix at one side of the domain. The structures of two disease-associated mutations in RyR2A (A77V and V186M) only altered the surface of the protein and, thus, the most likely role of these mutations was predicted to affect the binding interface with other parts of the channel(206). Similarly, solution NMR of RyR1A disease-associated mutations (C36R, R164C, and R178C) showed that mutations do not perturb the global structure, again indicating that they likely cause local structural changes that would affect the binding interface(205). Nonetheless, a single domain construct was insufficient for reliably docking onto the full-length cryo-EM map

of RyR, and, therefore, which interfaces are targeted by disease-associated mutations remained elusive.

Since then, the crystal structure of a larger N-terminal region of RyR1, comprising of three domains (RyR1ABC), allowed for a definitive positioning of the N-terminal region within the full-length RyR1, where four subunits of RyR1ABC form a cytoplasmic vestibule around the four-fold symmetry(208). RyR is an allosteric channel, where its opening coincides with coordinated conformational changes throughout the channel(122). In particular, the N-terminal region goes through significant conformational change during the channel opening. Interface 1, formed between domains A and B across subunit, have been identified as the key interface for channel gating and is the target for a large proportion of disease-associated mutations found in the region(209). At this interface, the β 8- β 9 loop harbors the largest cluster of disease-associated mutations and was previously termed the hot spot loop, or the HS-loop(205,206).

In the initial investigations of crystal structures of RyR1A and RyR2A, the HS-loop was fully visible, forming a rigid structure(205,206). Mutations in the HS-loop (R164C and R178C, rabbit RyR1 numbering) did not cause an overall structural perturbation, and the effect of mutations in the loop remained unclear. In RyR1ABC, the HS-loop was once again revealed as a rigid structure. The close proximity of domain B from the adjacent subunit in the full-length channel would further imply that the mobility of the loop is restricted. Furthermore, two buried disease-associated mutations adjacent to the intersubunit interface have been shown to alter the structures of loops located at the interface, including the HS-loop, suggesting that the conformation of the loops at the interface is important in channel regulation(209).

Here, we show the crystal structures of three HS-loop mutants in RyR2A: P164S, R169Q, and R176Q. The mutations did not cause structural change in the overall domain, but the loop in

each mutant became partially flexible (Figure 3.1). This observation differed from the previous structures of the wild-type RyR1A, RyR1ABC, and RyR2A, in which the loop formed a rigid structure(205,206,208). The increased mobility of the loop in the HS-loop mutants was also confirmed through solution NMR, where chemical shift perturbations were significantly higher only at the loop and its vicinity in the mutants compared with the wild type (Figure 3.3).

Thus, mutations in the HS-loop perturb the structure of the loop and its vicinity. The loop is located at the interface involved in conformational changes upon channel opening. This interface (interface 1) likely works as a brake, whereby interactions formed at the interface stabilize the closed state. Incidentally, interface 1 is the prime target for disease-associated mutations in the N-terminal region, with the HS-loop harboring the largest number of mutations in domain A. Taken together, structural changes induced by disease-associated mutations in the HS-loop would likely disrupt the intersubunit interface and lead to increased channel opening.

Two of the mutations in this study, P164S and R169Q, are associated with CPVT, while R176Q is linked to ARVD2. Yet all three mutations are located on the same loop, and they all cause perturbation of the loop to a similar extent. In RyR1, many mutations cause gain of function and target the cytoplasmic portion, while others confer loss of function and are mainly located near the transmembrane region(27). This difference in the function and location of the mutations may explain why some are associated with MH and others with CCD. In some cases, nonetheless, the same mutations have been linked to both diseases, and the reason for different phenotypes are still unclear. Could R176Q mutation in RyR2 differ from the other two mutations in this study due to its formation of new hydrogen bond and salt bridge within the HS-loop? This question remains to be answered.

The previous structure of RyR2A wild type was crystallized in space group that differs from mutant structures, both in the earlier and current studies(206,207). The comparison of the wild type structure with that of the A77V mutant shows that the HS-loop conformation differs between the two, although A77V is located away from the loop and only alters the surface structure (Figure 3.2). Therefore, the loop conformation is affected by the crystal contact, and the exact conformation of the loop in the crystal structures, as well as the extent of increased mobility due to mutations, are uncertain. However, the solution NMR of the HS-loop mutants confirms that the mutations increase the flexibility of the loop. The existence of multiple conformations of the loop and the increased flexibility in the disease-associated mutants strongly suggest that the HS-loop plays a crucial role at the intersubunit interface in the physiological context, in which the motion of the loop contributes to the regulation of channel opening. Future experiments involving the HS-loop in the natural conformation formed by tetramerization of the N-terminal region would shed further light on the effect of the HS-loop mutants.

Chapter 4: The cardiac ryanodine receptor N-terminal region contains an anion-binding site that is targeted by disease-associated mutations

Several high- and low-resolution studies have shed light on the ryanodine receptor (RyR) structure(238). Cryo-electron microscopy (cryo-EM) reconstructions show that the RyR has an overall mushroom shape(119,121,122), with the stalk crossing the membrane and the large cap located entirely in the cytosol. In addition, several crystal structures of cytoplasmic domains or domain clusters have been solved(205,206,208,209,211,215,216). In some cases, these can be docked reliably into the available cryo-EM maps. This includes the N-terminal region of RyR1, an area consisting of three domains (A, B, and C), which was found to be located near the four-fold symmetry axis, forming a cytoplasmic vestibule(208). Opening and closing of RyRs result in many allosteric motions within the cytoplasmic cap(122). This includes movements in the N-terminal region, and an attractive model suggests that intersubunit contacts, mediated by domains A and B from neighboring subunits, can be disrupted upon channel opening(209). As such, it appears that the N-terminal region acts as a “brake” on channel opening.

RyRs are targets for hundreds of disease-associated mutations. Over 150 mutations have been found in RyR2 that are mostly associated with catecholaminergic polymorphic ventricular tachycardia (CPVT), a condition that leads to triggered cardiac arrhythmias and can result in sudden cardiac death(17). In addition, some mutations are associated with arrhythmogenic right ventricular dysplasia type 2 (ARVD2) and idiopathic ventricular fibrillation(18). In RyR1, mutations can lead to several disorders, including malignant hyperthermia (MH)(274) and central core disease (CCD)(263,275). Based on the crystal structure of the RyR1 N-terminal region, it

was found that disease mutations are mostly found at interfaces between domains and are capable of altering relative domain orientations(209). Although many mutations have been mapped onto the RyR1 crystal structure, our high-resolution insights into the corresponding region of RyR2 have been limited to the very N-terminal domain(206). Here, we describe the crystal structure of the N-terminal region of RyR2 (residues 1-547), an area encompassing 29 distinct disease-associated mutations. The protein folds up in three individual domains (“RyR2ABC”), which are, unlike RyR1, held together via a central chloride anion that shields repulsive positive charges. This anion-binding site is the target for disease mutations that cause CPVT. The results suggest that anion binding affects relative domain orientations and may regulate RyR2.

4.1 Methods

4.1.1 Cloning, purification, and crystallization of RyR2 N-terminal region

Mouse RyR2 residues 1-547 (RyR2ABC) was cloned and expressed as previously described for the RyR1 constructs(208). All point mutants were prepared using the QuikChange protocol (Stratagene). The delta exon 3 variant of RyR2ABC was cloned using a full-length construct as a template (gift from the laboratory of Dr. Wayne Chen, University of Calgary). The proteins were purified similarly to the corresponding RyR1 construct, except that following a ResourceQ column (GE Healthcare), they were run on a Phenyl Sepharose column (GE Healthcare) in 10mM Tris-Cl pH 8.0 and 14mM β -ME, with a gradient from 50 to 1500mM KCl. The samples were then run on a preparative Superdex 200 (GE Healthcare).

Protein crystals were produced by exchanging the samples to 250mM KCl, 10mM Na-HEPES pH 7.4 and 5mM dithiothreitol (DTT) and concentrating them to 10mg ml⁻¹ using 10,000 MW cutoff concentrators (Amicon, Millipore). All crystals were obtained at room temperature

using the hanging drop method. Wild-type proteins were crystallized in 0.1M Tris pH 8.15, 5-10% PEG3350, and 1% EtOH. Bromide-bound protein and the R420Q mutant crystallized in similar conditions, except that seeding using wild-type crystals was necessary. All crystals were flash-frozen in the corresponding mother liquor containing 40% PEG200 or 35% glycerol. Crystals in complex with bromide were obtained by exchanging KCl for KBr through dialysis.

4.1.2 Data collection, structure solution, and refinement

Data were collected at beamlines 08ID of the Canadian Light Source (CLS, Saskatoon) and 9-2 of the Stanford Synchrotron Radiation Laboratory (SSRL, Menlo Park). The data were processed using XDS(241). The RyR2ABC wild-type structure was solved using molecular replacement implemented in Phaser(242) with the individual domains of RyR1ABC structure as search models. An improved structure was then generated through autobuilding using Arp/wArp(276). Refinement consisted of successive rounds of manual modeling in COOT(243) and refinement in REFMAC5(244) with translation, libration, and screw-rotation (TLS) restraints applied to individual domains. The RyR2ABC R420Q and R414C mutant structures were solved using the individual domains of RyR2ABC as search models and refined as described for wild-type RyR2ABC. Data collection and refinement statistics are available in Table 4.1. Coordinates and structure factors for the RyR2ABC wild-type and R420Q mutant structures have been deposited in the RCSB Protein Data Bank with the accession numbers 4L4H and 4L4I, respectively. Anomalous maps for the bromide-grown crystal were obtained using calculated phases from the RyR2ABC structure and using anomalous differences from a data set collected at the peak absorption of bromide.

Table 4.1: Crystallographic parameters. Values in parentheses are for the highest-resolution shell. RMSD = root mean square deviation.

	WT	R420Q	R414C
Data collection			
Space group	P4 ₂ 2 ₁ 2	P4 ₂ 2 ₁ 2	P4 ₂ 2 ₁ 2
Cell dimensions			
<i>a</i> , <i>b</i> , <i>c</i> (Å)	78.04, 78.04, 248.38	78.22, 78.22, 248.65	79.49, 79.49, 250.43
<i>α</i> , <i>β</i> , <i>γ</i> (°)	90, 90, 90	90, 90, 90	90, 90, 90
Resolution (Å)	50-2.00 (2.05-2.00)	50-2.15 (2.27-2.15)	50-2.15 (2.19-2.15)
<i>R</i> _{sym} or <i>R</i> _{merge}	9.1 (173.2)	10.3 (188.8)	6.8 (84.7)
<i>I</i> / <i>σI</i>	15.6 (2.0)	20.2 (2.4)	47.5 (2.2)
Completeness (%)	99.6 (99.9)	99.7 (99.7)	99.7 (98.9)
Redundancy	5.7 (5.8)	14.3 (14.7)	13.7 (9.9)
Refinement			
Resolution (Å)	50-2.00	50-2.15	50-2.15
No. reflections	50190	40856	44761
<i>R</i> _{work} / <i>R</i> _{free}	22.03/25.11	22.83/26.29	19.65/21.95
No. atoms			
Protein	3564	3553	3580
Ligand/ion	18	6	7
Water	83	64	146
B-factors			
Protein	45.4	21.6	63.8
Ligand/ion	51.9	58.5	91.7
Water	44.6	23.1	59.4
RMSD			
Bond lengths (Å)	0.021	0.013	0.007

	WT	R420Q	R414C
Bond angles (°)	1.809	1.430	0.981

4.1.3 Fluorescence-based thermal shift assays

Protein melting curves were measured using thermofluor assays(245). A total of 10 μ l of 1mg ml⁻¹ protein was mixed into a 40 μ l solution containing 1 \times SYPRO orange dye (Invitrogen), 150mM KCl, 10mM HEPES pH 7.4, and 14mM β -ME. Melting curves were obtained using a DNA Engine Opticon 2 real-time PCR machine (Bio-Rad), using the SYBR filter option. The temperature was increased from 25°C to 95°C with 0.5°C steps, with the temperature held constant for 15s before data acquisition. Melting temperatures were obtained by taking the maxima of the first derivatives of the melting curves.

4.2 Results

4.2.1 Overall structure of the RyR2 N-terminal region

We solved the structure of mouse RyR2 residues 1-547 (RyR2ABC) at 2.0Å resolution. The structure consists of three individual domains (A, B, and C) that form a compact arrangement (Figures 4.1a and 4.2). Domains A and B display β -trefoil folds, whereas domain C forms an α -helical bundle typical of armadillo repeats. Domain A contains an α -helix, previously observed for the structure of the individual domain(206) and RyR1ABC(208), but in this case the helix was disordered, suggesting there is some intrinsic flexibility to this secondary structure element. The domains are held together by a number of ionic interactions (Table 4.2). In the corresponding RyR1ABC structure, ionic interactions are also responsible for the compact domain arrangement, and the overall domain orientations between the two isoforms are similar (Figure 4.1b). We compared the thermal stabilities of RyR1ABC and RyR2ABC via thermofluor

assay. The RyR2ABC protein appeared less stable than RyR1ABC (rabbit residues 1-536), with an approximately 5°C difference in melting temperature, although the melting transition occurred later and was steeper (Figure 4.1c).

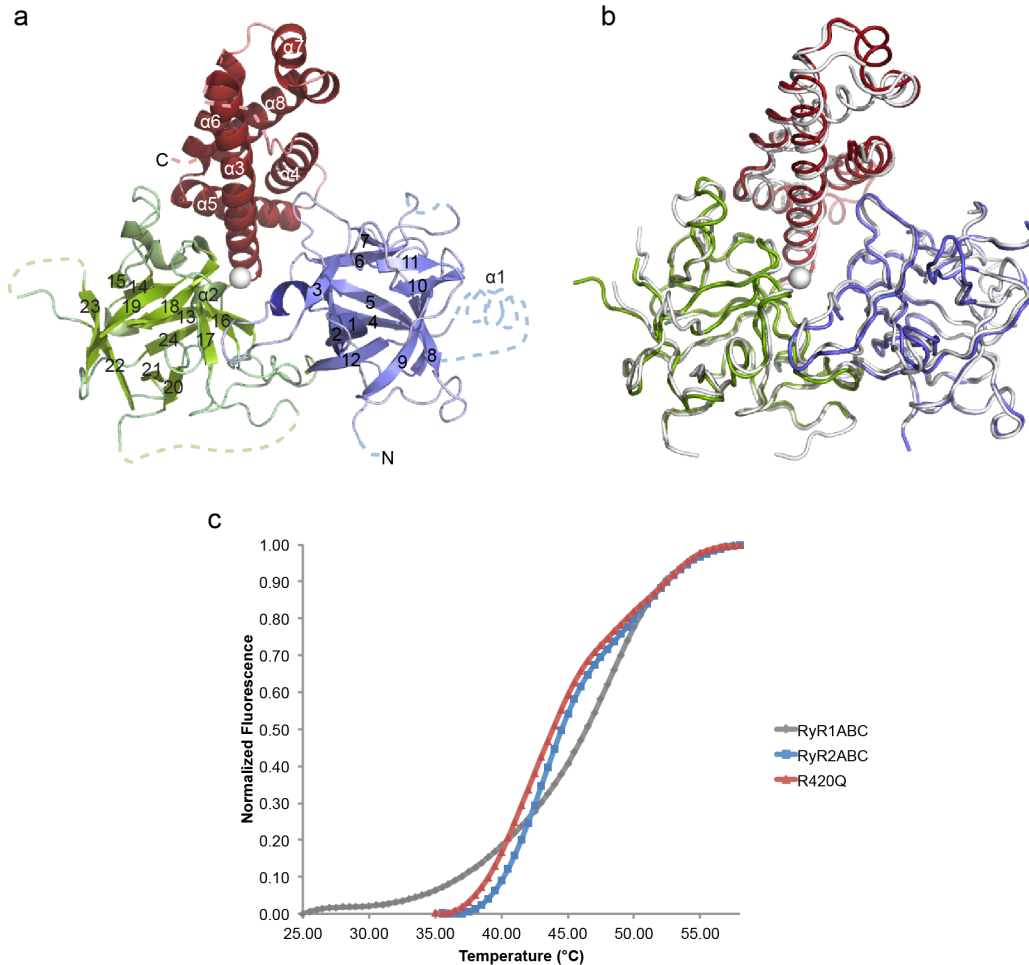


Figure 4.1: Overall structure of the RyR2 N-terminal region. (a) Cartoon representation of mouse RyR2 residues 1-547 (RyR2ABC). Blue, domain A; green, domain B; and red, domain C. Select secondary structure elements are labeled. **(b)** Superposition of RyR1ABC (gray) and RyR2ABC (colors). **(c)** Thermal melt curves indicating thermal stability. The melting temperatures, obtained by the maxima of the first derivatives, are 48.0°C ± 0°C (RyR1ABC), 43.1°C ± 0.4°C (RyR2ABC), and 42.3°C ± 1.4°C (RyR2ABC R420Q), where errors indicate standard deviation of the mean. The RyR2ABC wild-type (WT) and mutant melting curves show two transitions, but due to the shallow nature of the second transition, a melting temperature for this portion could not be obtained reliably.

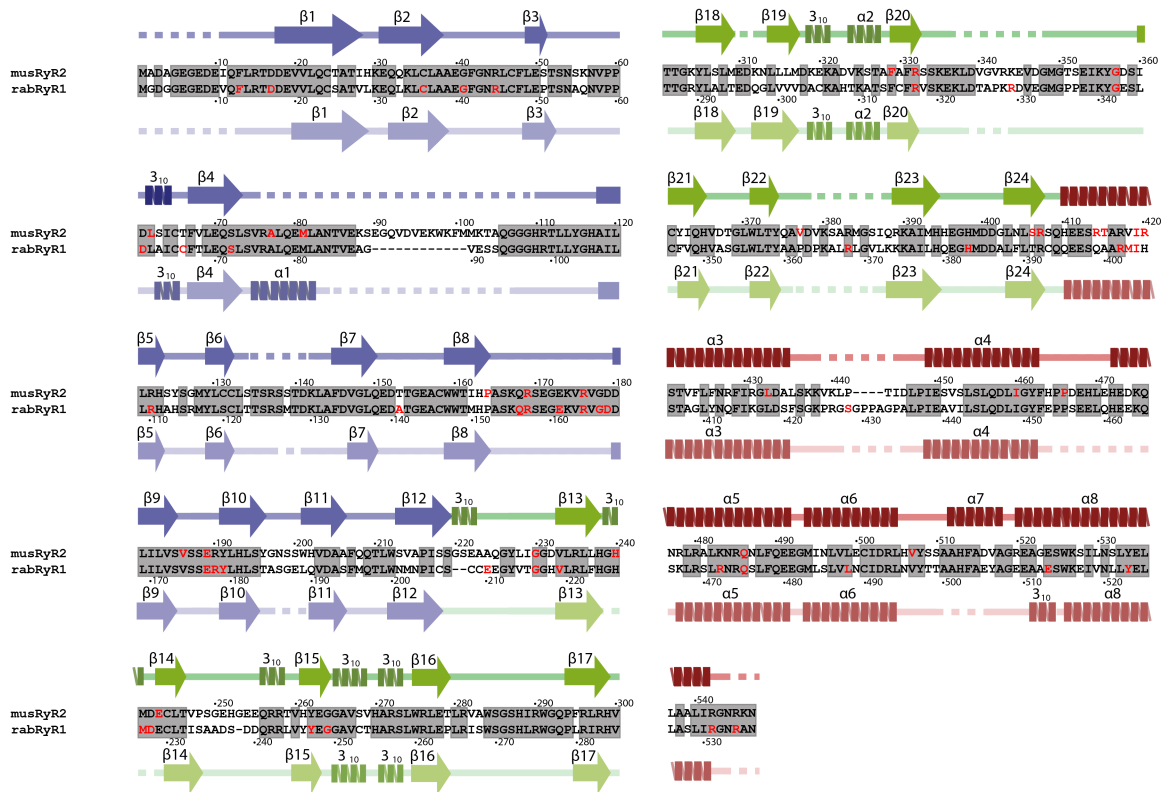


Figure 4.2: Sequence alignment of RyR2 and RyR1 N-terminal regions. Sequence alignment of the N-terminal regions of mouse RyR2 and rabbit RyR1, showing the secondary structure obtained from each crystal structure above and below, respectively. Coils represent α helices, while arrows represent β strands. Portions present in the crystallized construct but not modeled due to flexibility are indicated by dashed lines. Gray boxes highlight residues conserved between the two isoforms, and residues shown in red are targets of disease-associated mutations.

Table 4.2: Interdomain salt bridges. Ionic pairs between domains in RyR1ABC and RyR2ABC structures. The “x” marks ionic pairs that do not exist in RyR2ABC.

Domains involved	Rabbit RyR1	Mouse RyR2
B-C	Arg242-Glu481	Arg257-Glu492
B-C	Arg221-Glu397	Arg235-Glu412
B-A-C-A (network)	Arg283-Asp61-Arg402-Glu40	Arg298-Asp61xArg417xGlu40
A-C	Arg45-Asp447	Arg45-Asp458

Despite the similarity in the overall domain arrangement, a closer inspection of the domain-domain interactions reveals a crucial difference. In RyR1, there is an ionic-pair network consisting of four residues that are located in all three domains (Table 4.2 and Figure 4.3a): Arg283 (domain B) forms a salt bridge with Asp61 (domain A), which also forms an ionic pair with Arg402 (domain C), which finally forms a further salt bridge with Glu40 (domain A). Such networks of interactions are more stable than individual pairs, and this is, therefore, a major stabilizing element for the RyR1ABC structure. The latter three residues in the network also form multiple hydrogen bonds with one another, further adding to the stability. In RyR2, however, this network is disrupted (Figure 4.3b). Although the four residues involved in the network are conserved, there is a substitution of RyR1 His405 (domain C) by Arg420 in RyR2. Instead of a four-residue network, only a single ionic pair remains, formed by Arg298 and Asp61, and all hydrogen bonds within the network are lost.

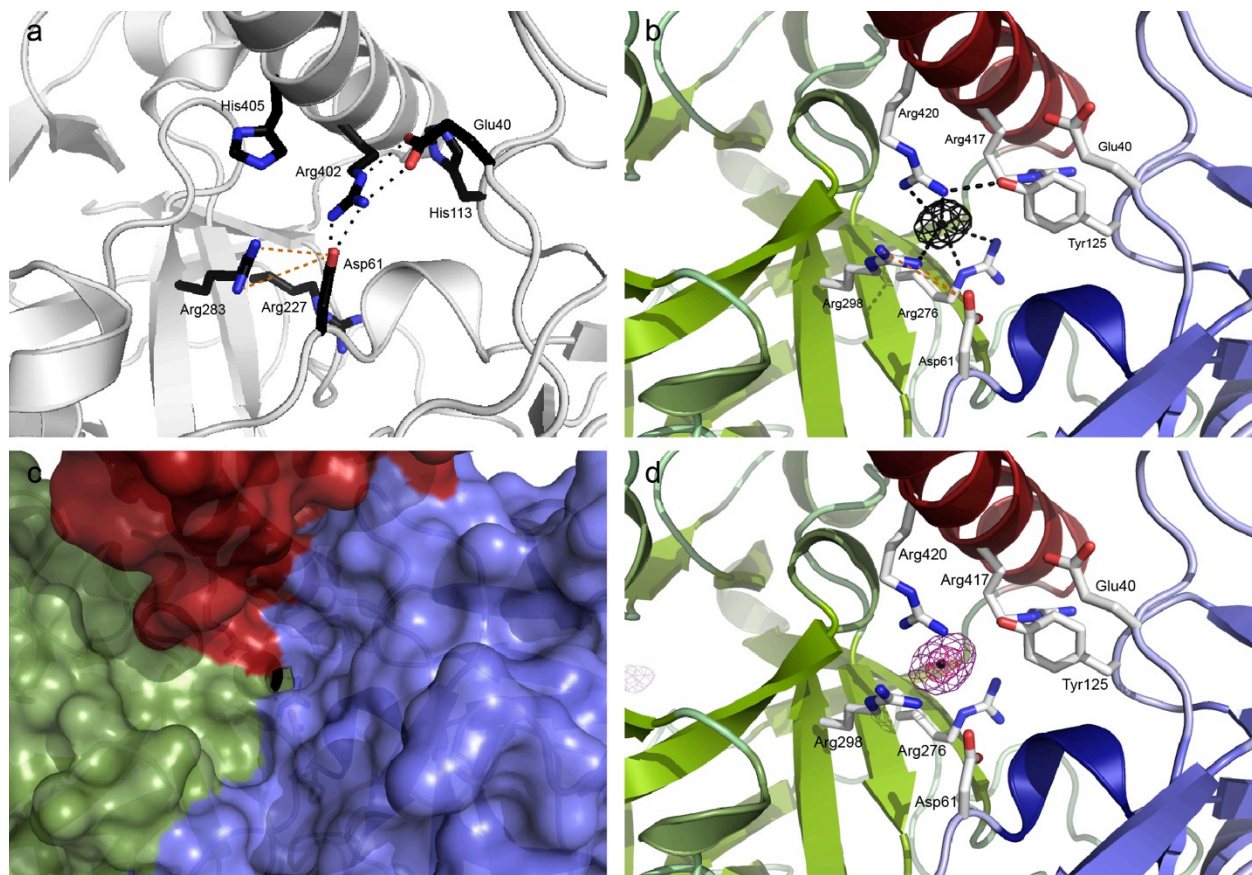


Figure 4.3: Details of the anion-binding site. (a) Inter-domain interaction area for RyR1ABC showing the salt-bridge network involving residues in all three domains. Black dashed lines indicate hydrogen bonds between ionic pairs. Orange dashed lines indicate a salt bridge between Arg283 and Asp61 that is not formed by hydrogen bonds. (b) The corresponding region in RyR2ABC. Domains are colored as in Figure 4.1. $F_o - F_c$ density, contoured at 3σ , is shown for the chloride site. Dashed lines indicate contacts with positively charged arginine atoms and a hydrogen bond between Tyr125 and Arg420. Two histidine residues in RyR1 are replaced by Arg420 and Tyr125 in RyR2. This results in a disruption of the ionic pair network and the creation of a chloride-binding site. Arg298 and Asp61 form a salt bridge that is not mediated by hydrogen bonds. (c) Surface representation of RyR2ABC, with the chloride ion shown as a black sphere. The chloride is inaccessible to solvent. (d) Anomalous difference maps for the bromide-bound structure, contoured at 7σ (outer mesh) and 20σ (inner mesh). The peak is visible up to 34σ .

Instead, the ionic pair network seems to be replaced by a chloride ion. It is coordinated by electrostatic interactions with residues from domains B and C: Arg420, Arg298, and Arg276. The hydroxyl group of Tyr125 is within 4.5Å, too far to create a hydrogen bond, but the Tyr125 side chain forms a “lid” that further shields the anion and its hydroxyl group hydrogen bonds with the Arg420 side chain. Arg417, involved in the network in RyR1, is near the chloride ion, but its positive guanidinium group is pointing away. The chloride site is almost completely buried (Figure 4.3c).

4.2.2 Chloride can be exchanged

The RyR2ABC protein was purified in the presence of high KCl concentration. The chloride binding appeared essential for stability, as removal of chloride prevented the protein from remaining soluble at concentrations required for crystal growth. The absence of an anion would allow several positively charged arginines to be in proximity, which destabilizes the domain-domain interactions.

Does the site also accommodate other anions? In order to answer this question, we exchanged KCl with KBr, and the concentrated protein remained stable in solution under these conditions. We then grew RyR2ABC crystals in bromide and obtained a 2.3Å structure. Data were collected at the absorption edge for bromide, allowing us to calculate anomalous difference maps. An anomalous peak was visible up to 34σ (Figure 4.3d), providing an unambiguous assignment for a bromide ion at the anion binding site. As the ionic radius for bromide (1.82Å) is only slightly larger than for chloride (1.67Å), it is not surprising that it can bind to the same site. Bromide ions are not physiologically relevant, but the bromide anomalous signal confirms the presence of a halide-ion binding site. Since the KCl was exchanged for KBr only at the end of the purification, this also means that anion binding to this site is a reversible process. Although

the anion is buried and protected from solvent within the structure, this shows that dynamic breathing motions allow ion exchange.

4.2.3 Chloride dissociation constant is below 4mM

The chloride binding seems important for the structural stability of RyR2ABC since the protein is unstable without the presence of high KCl concentration. We wondered if the chloride ion also has a physiological function in RyR regulation. To answer this question, we probed the chloride affinity of RyR2ABC. If the affinity for the anion were at the physiological level, this would strongly suggest that the chloride binding has a functional role rather than simply being a structural part that is always bound to the protein.

We attempted to measure the affinity of the chloride binding in RyR2ABC using ITC. For this experiment, we used the HMT-RyR2ABC fusion protein since RyR2ABC on its own becomes insoluble at the concentration required for ITC experiments when chloride ions are dialyzed out. The maltose binding protein in the HMT portion would help stabilize RyR2ABC. We titrated 800 μ M of NaCl into 43 μ M of HMT-RyR2ABC but could not detect any binding. Subsequent gel filtration chromatography showed that the protein was partially aggregated, indicating that the removal of chloride ions caused protein misfolding.

Next, we wondered if we could crystallize RyR2ABC at lower KCl concentrations and capture different levels of bound-chloride occupancies. We performed serial dilutions of RyR2ABC in lower KCl concentrations starting from 50mM in the presence of 150mM Na-HEPES pH7.4 to compensate for the ionic strength in the buffer. A protein concentration of 6.5mg ml⁻¹ was used, which is high enough for the crystallization to occur but still lower than usual, which may prevent the insolubility in low salt. RyR2ABC was soluble up to 5mM KCl but was partially precipitated at 4.5mM and 4mM KCl. The protein was completely insoluble at KCl

concentrations of 0, 2, and 3mM. We collected diffraction data for crystals obtained at 10, 5, 4.5, and 4mM KCl and solved the respective structures. However, the chloride ion occupancy was 100% in every KCl concentration after performing an occupancy refinement, and lower KCl level did not cause structural changes in the protein (Figure 4.4). This suggests that the dissociation constant for the chloride binding is somewhere below 4mM.

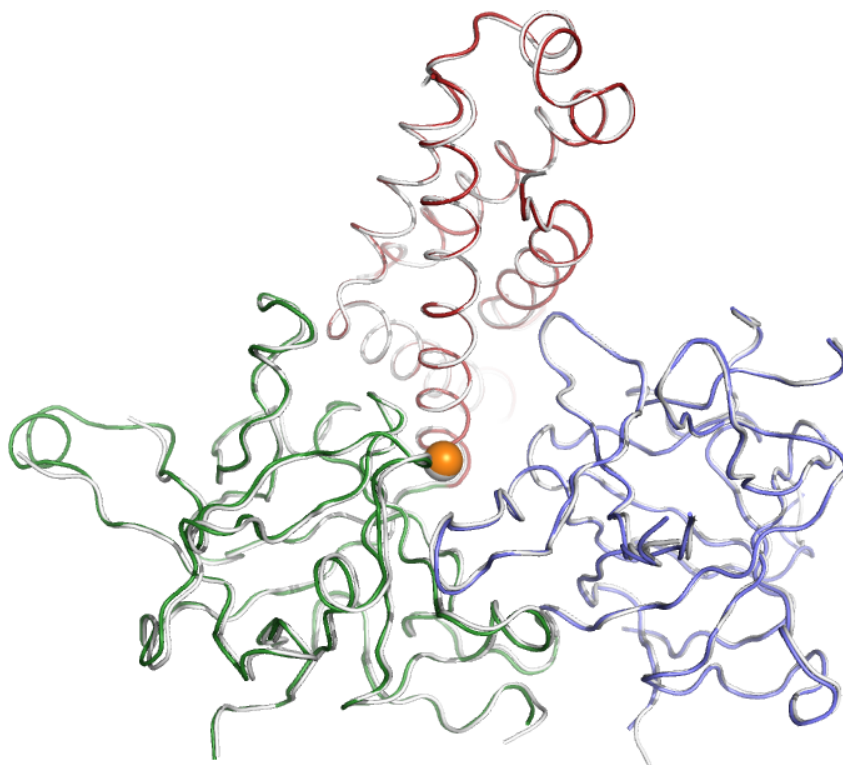


Figure 4.4: Structure of RyR2ABC crystallized in 4mM KCl. The superposition of the structures of RyR2ABC crystallized in the presence of 4mM KCl (colors) and in 250mM KCl (white) shows no structural alterations. For better comparison, the 250mM KCl structure was solved from a crystal soaked in glycerol as the cryo-protectant prior to data collection (unpublished). The spheres represent chloride ion (orange, 4mM KCl; and white, 250mM KCl). The 4mM KCl structure contains an extra helix in domain B that is discussed in detail in Section 4.2.7.

Since we could not obtain crystal structures of RyR2ABC at KCl concentrations lower than 4mM, we performed soaking experiments using crystals grown at 250mM KCl. The crystals

were transferred into drops containing KCl concentrations between 0mM and 4mM, washed by transferring into new drops, and equilibrated over several days. Crystals at all levels of KCl tested stayed intact after the soaking experiment and diffracted well. However, subsequent occupancy refinement of the structures showed that chloride was bound at 100% occupancy in every concentration tested. Moreover, chloride was bound even in crystals that were soaked in the absence of KCl. This suggests that although chloride can be exchanged in solution, it cannot be removed after the protein crystal formation. This is consistent with the observation that the chloride ion bound within RyR2ABC is inaccessible to the solvent (Figure 4.3c), where the crystal lattice tightly packs the ABC domains into rigid structure that no longer “breathes.”

4.2.4 The R420Q disease-associated mutation affects chloride binding

One of the arginines that coordinate the chloride ion, Arg420, is the target for two disease-associated mutations (R420Q and R420W). We investigated the structure of the R420Q mutant, which has been linked to CPVT(277). In RyR1, the corresponding residue is a histidine instead and no chloride binding was detected. We therefore expected the R420Q mutation to abolish the binding site and to re-establish the central ionic pair network observed in RyR1. We solved the crystal structure of RyR2ABC R420Q at 2.15Å resolution (Figure 4.5). As expected, no density was observed for a chloride ion. However, the ionic pair network was not restored. In particular, the Arg417 side chain, which is involved in the network in RyR1 by pairing up with Asp61 and Glu40, still does not pair up with either residue in the R420Q mutant, despite the absence of the chloride ion. This seems to be due to the side chain of Tyr125, which would sterically clash with Arg417 in its configuration necessary for the salt bridges. Both Tyr125 and Arg420 appear to be strongly conserved among all mammalian RyR2 sequences as well as in some other species (Figure 4.6). The exception is RyR2 from *Myotis davidii*, which does contain

Arg420 but not Tyr125. Overall, this suggests that the anion binding is strongly conserved among mammalian RyR2s and may play a functional role.

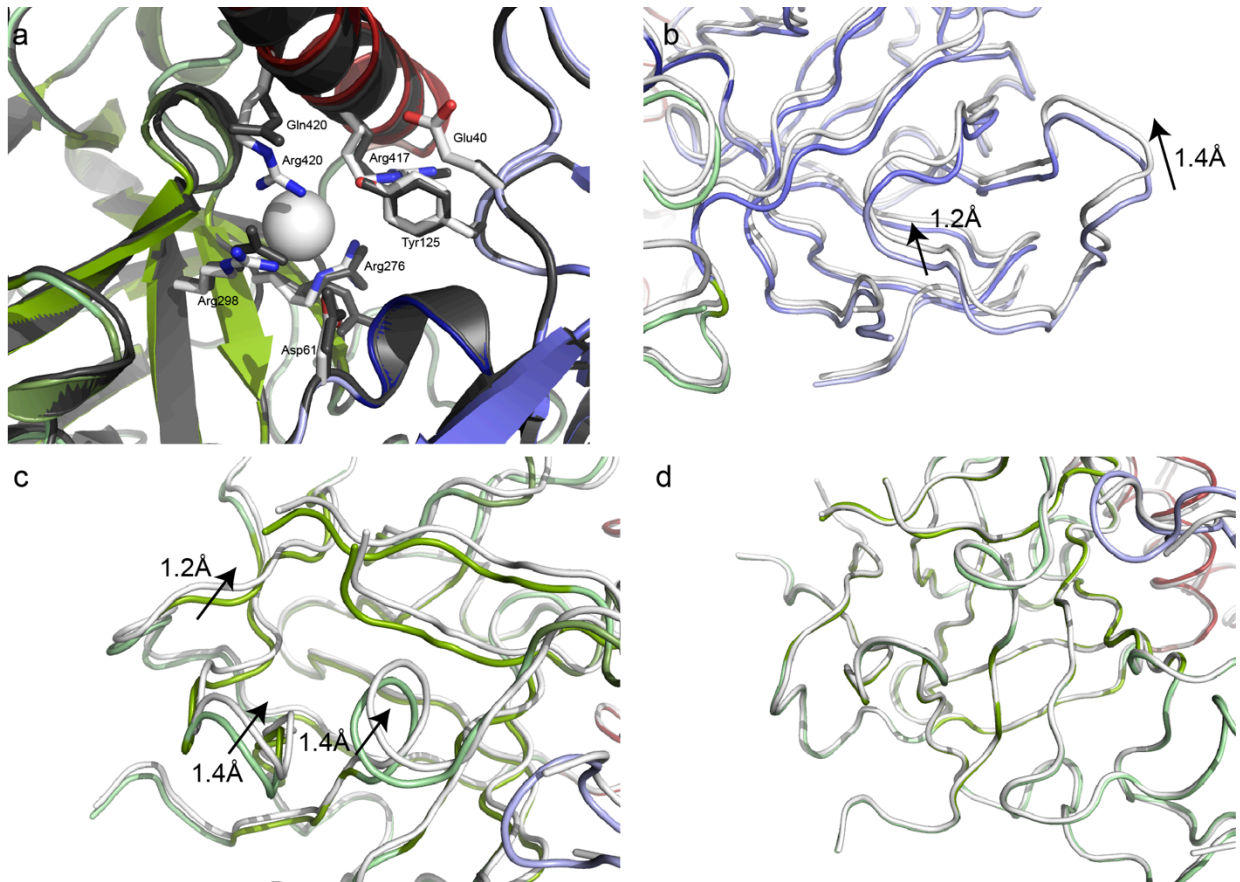


Figure 4.5: Structure of the R420Q disease-associated mutant. (a) Crystal structure of the R420Q disease-associated mutant (gray) superposed on the RyR2ABC wild-type structure (colors). No chloride density was visible for the disease mutant. (b,c) Superposition of wild type (colors) and R420Q RyR2ABC (white) based on domain C, showing the relative positions of domains A (b) and B (c). Shifts in the domain arrangement are indicated by arrows. Domains A and B are shifted relative to domain C. (d) Superposition of wild type and R420Q based on domain A, showing a near-perfect superposition of domain B, indicating the relative orientation of domain A versus domain B is unchanged.

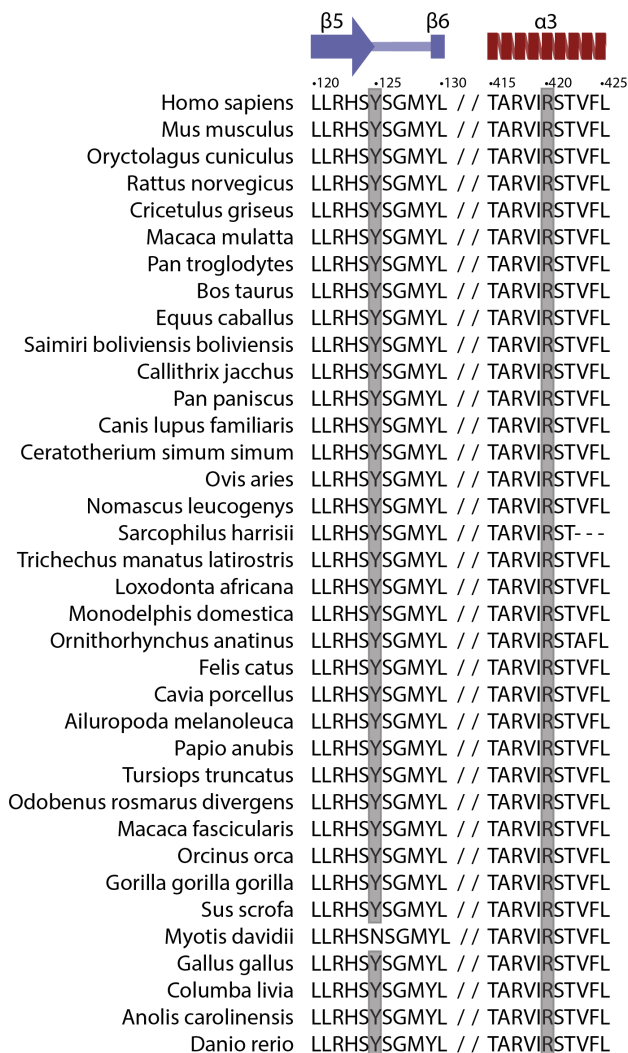


Figure 4.6: Sequence alignment of various mammalian RyR2 sequences. Sequence alignment of various mammalian RyR2 sequences, clustered around Tyr125 and Arg420 (mouse RyR2 numbering; highlighted in gray), along with select RyR sequences from non-mammalian vertebrates. With the exception of *Myotis davidii*, both Tyr125 and Arg420 are strongly conserved.

The absence of chloride in the R420Q structure removes a link between domain C (Arg420) and domain B (Arg276 and Arg298). Although the local rearrangements around the chloride site are small, the mutation seems to affect relative domain reorientations. Superposition based on domain C alone shows that the positions of domains A and B relative to domain C are

changed; main-chain atoms in domain A and B shift by as much as 1.4Å (Figure 4.5b,c). These shifts seem to be the result of a tilting around an axis near the domain B-C interface. As a result, the shifts are almost invisible right next to the chloride-binding site and are largest further away. In contrast, the relative position of domains A and B is unchanged (Figure 4.5d). We have previously observed that interdomain salt bridge mutations in RyR1 can cause similar relative domain reorientations(209). Altering domain orientations, thus, seems to be a common theme with several disease-associated mutations in both RyR1 and RyR2.

Although no chloride was detected for the R420Q mutant, we wondered whether there is still some residual affinity, resulting in a lower occupancy of the anion-binding site that could not be detected in conventional difference maps. We, therefore, also co-crystallized the R420Q mutant with KBr and kept a high concentration of KBr (500mM) during the soak into cryo-protectant. After creating an anomalous difference map, a peak was visible at the anion-binding site but only visible to 5.5σ compared with 34σ for the wild type, suggesting a much lower occupancy despite the increased KBr concentration. The mutant, therefore, has a reduced affinity for anions but can still bind them at much higher concentrations.

4.2.5 Additional RyR2 disease-associated mutations

Figure 4.7a shows the positions of the known disease-associated mutations that target the RyR2ABC domains. In total, 29 RyR2 mutations can be mapped on the RyR2ABC structure, dispersed over 27 distinct sites (as two sites are the target for multiple mutations).

The Δ exon3 is an abnormal mutation that ablates residues 57-91, causing a severe form of CPVT(277-279). The deletion includes a β strand (β 4) that is part of the β -trefoil fold of domain A, but a crystal structure of RyR2A Δ exon3 showed that exon4, a flexible stretch in wild-type RyR2A, can rescue this by inserting itself into the β -trefoil core(211). In a recent NMR

study, the exon4 was shown to form a second α helix in domain A, which replaces the missing β strand in Δ exon3 protein(207). We were unable to purify the RyR2ABC Δ exon3 construct, as it was readily degraded and appeared unstable. Several residues in exon3 interact with domain B (Figure 4.7b). This includes Asp61, which forms a salt bridge with Arg298 on domain B (Figure 4.3b). As the identities of amino acid residues in exon4 are all different(211), the contacts between domains A and B mediated by the exon3 residues are very different. Our inability to obtain pure, non-degraded RyR2ABC Δ exon3 suggests that the alternative contacts involving exon4 are significantly less stable.

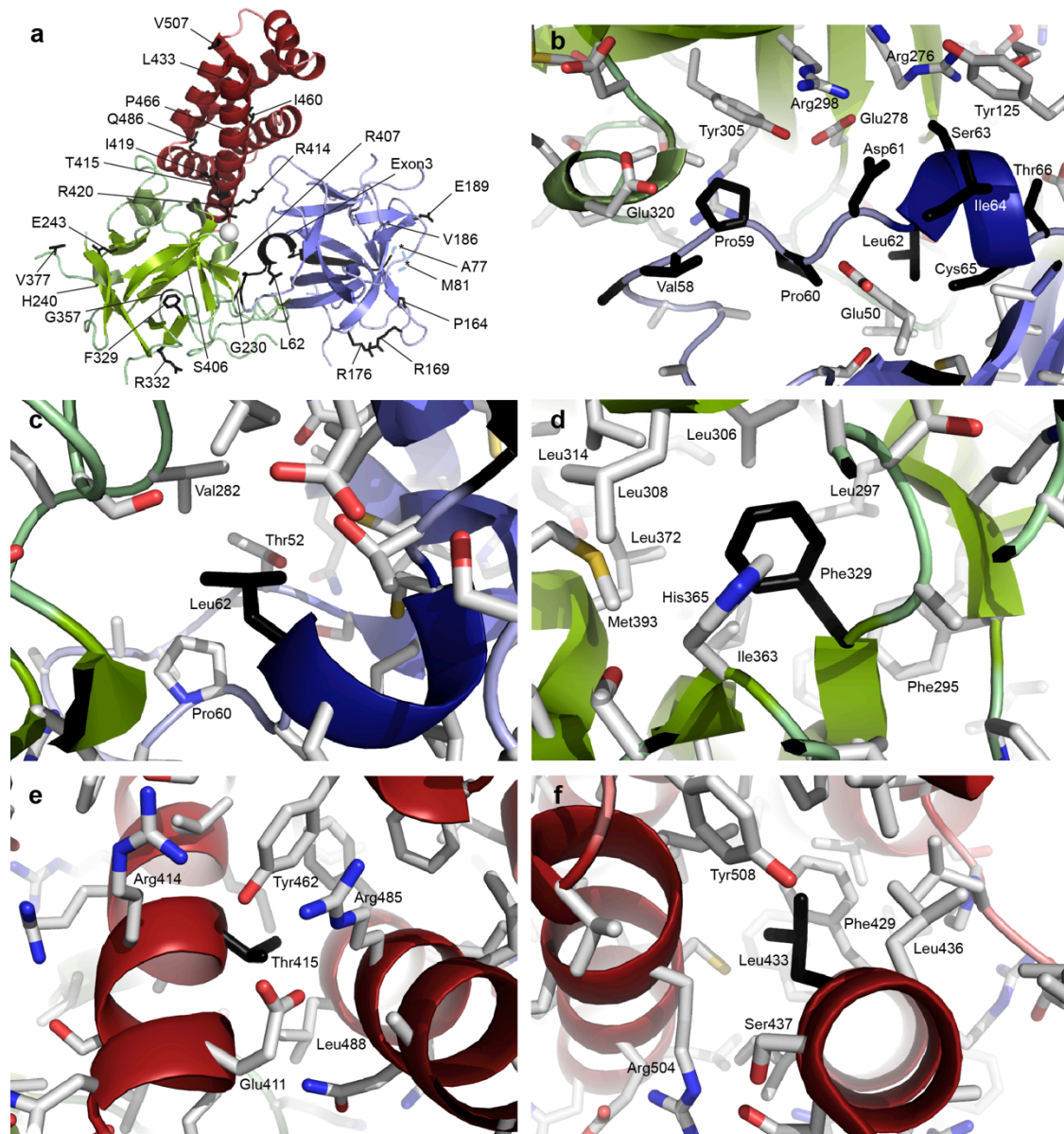


Figure 4.7: Additional RyR2 disease-associated mutants. Domains are colored according to Figure 4.1. (a) Mapping of known disease-associated mutations on the RyR2ABC structure, with the target residues shown as black sticks. Exon3 is shown in black cartoon representation. (b) Detail of several exon3 residues (black) interacting with domain B. (c-f) Details of the environments for four disease-associated-mutation target sites for which purification was attempted. The mutated residue in each case is shown in a black stick representation. All four caused destabilization of the protein, resulting in heavily degraded material. Shown are positions of L62F (c), F329L (d), T415R (e), and L433P (f).

In addition, we created a number of point mutants in RyR2ABC that correspond to individual disease-associated mutations. These include the mutants L62F, G230C, F329L, R414C, T415R, R420Q, and L433P and are either located at intrasubunit domain interfaces or are buried within individual domains (Figure 4.7a). All have been linked to CPVT(277), except for L433P, which has been found to associate with ARVD2(280).

The G230C mutation was reported in a recent study and exhibited increased sensitivity towards activation by cytosolic Ca^{2+} (266). Another study showed that the mutation also sensitizes RyR2 for activation by luminal Ca^{2+} (281). The corresponding residue on RyR1 is also the target for disease-associated mutation(209). On the RyR2ABC structure, Gly230 is located in the loop that connects domains A and B (Figure 4.8). The residue is part of a conserved Gly-Gly motif (Gly230 and Gly231), forming a tight turn just before the first β strand of domain B (β 13). The Gly230 C_α atom is buried near the domains A-B interface, and the addition of the Cys side chain would clash with the adjacent β strand (β 16). We were able to purify the G230C mutant in the RyR2ABC construct, but the majority of the protein readily degraded, and we could not obtain enough intact protein for crystallization experiments. Thermal melt analysis reveals that both the RyR2ABC wild type and G230C mutant unfold in a two-step process, and the G230C mutation causes a leftward shift in the first transition, indicating a decreased thermal stability (Figure 4.8b). Thus, G230C has a destabilizing effect on the N-terminal domains, and the location of the residue at the domains A-B interface suggests that the mutation likely alters the fold and stability of the interface, possibly affecting the relative orientations of domains A and B.

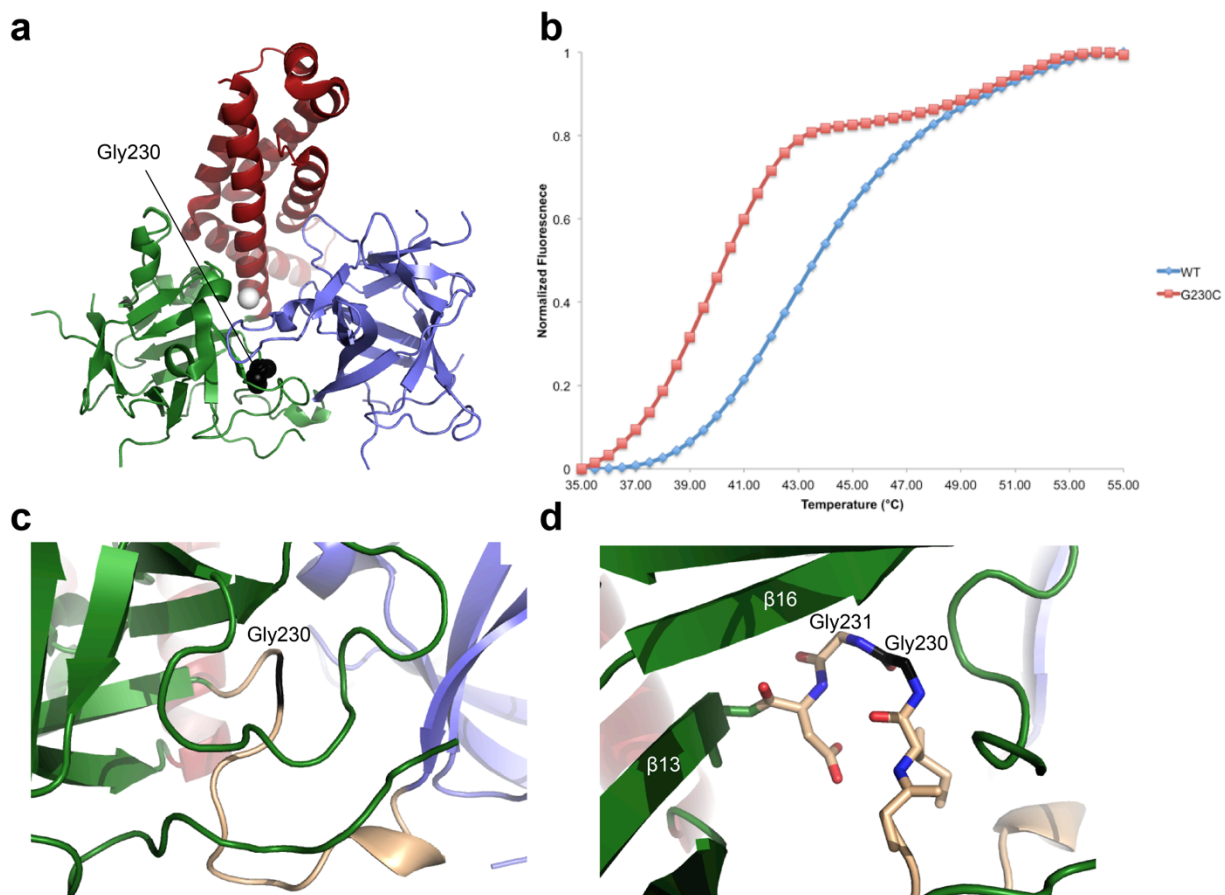


Figure 4.8: The G230C mutation reduces the thermal stability of RyR2ABC. Coloring scheme of the three domains is the same as in Figure 4.1. **(a)** Structure of RyR2ABC, with Gly230 represented by black spheres. **(b)** Representative thermal melting curves of the wild type and G230C mutant RyR2ABC (n=3). The melting temperatures, obtained by taking the maxima of the first derivatives, are $42.0^{\circ}\text{C} \pm 0.5^{\circ}\text{C}$ (wild type) and $39.7^{\circ}\text{C} \pm 0.3^{\circ}\text{C}$ (G230C). Errors indicate standard deviation of the mean. Both curves show two transitions, but due to the shallow nature of the second transition, a melting temperature for this portion could not be obtained reliably. **(c,d)** Close-up views showing the Gly230 residue (black) as part of the turn preceding the first β strand of domain B ($\beta 13$). The loop connecting domains A and B that harbors Gly230 is shown in cream color. In **d**, Gly230 and the neighboring residues in the loop are shown as stick representations that clearly reveal a tight turn formed by the two Gly residues. The C_{α} atom of Gly230 is located in close proximity to $\beta 16$, which would not easily accommodate a Cys side chain.

Arg414 is the target of two CPVT-associated mutations (R414C and R414L)(282-284). The residue is located at the A-C interface but is also exposed at the surface of RyR2ABC. The side chain of Arg414 is not involved in hydrogen bonds or salt bridge interactions, and there is plenty of space for Cys or Leu substitution. We wondered how R414C is able to cause the CPVT phenotype. To gain such insight, we solved the crystal structure of R414C. The overall structure of the R414C mutant does not differ from that of the wild type, but the mutation confers subtle changes at the A-C interface (Figure 4.9). The R414C mutant is able to bind a chloride ion, but two of the arginine residues that coordinate the anion adopt conformations that differ from the wild type, in which Arg417 acquires and Arg276 loses a dual conformation in the mutant (Figure 4.9a). Although this swap does not seem to affect the chloride binding, it may cause subtle changes to the affinity. The Arg414 side chain is not involved in hydrogen bonds or salt bridges, but it does interact with the Phe42 side chain through van der Waals interaction (Figure 4.9a,c). The removal of the arginine side chain in the R414C mutant disrupts this interaction, and the Phe42 side chain swings away from Cys414 (Figure 4.9a,d).

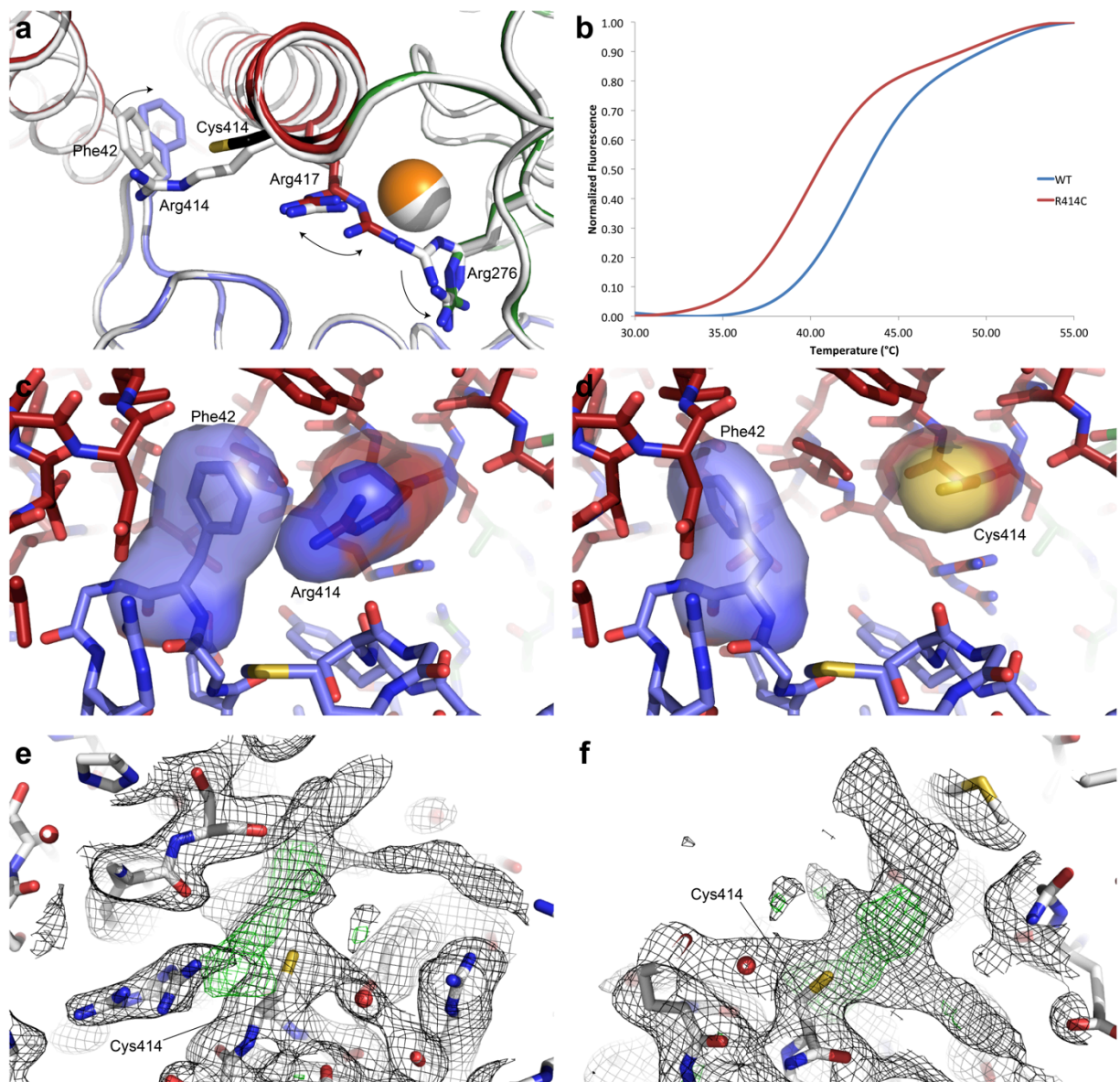


Figure 4.9: The structure and thermal stability of R414C. (a) The crystal structure of RyR2ABC R414C (colors) superposed onto the wild-type structure (white), showing the close-up view around the mutation site. Since the R414C structure was solved using crystals frozen in glycerol, the wild type structure was also solved using crystals frozen in the same cryo-protectant (unpublished) for a better comparison. Coloring scheme of the three domains is the same as in Figure 4.1. Arrows indicate shifts of select side chains in the mutant with respect to the wild type. The chloride ion is represented by a sphere (orange in the mutant and white in the wild type). (b) Representative thermal melting curves of the RyR2ABC wild type and the R414C mutant (n=4). The melting temperatures, obtained by

taking the maxima of the first derivatives, are $42.6^{\circ}\text{C} \pm 0.25^{\circ}\text{C}$ (wild type) and $39.5^{\circ}\text{C} \pm 0.0^{\circ}\text{C}$ (R414C). Errors indicate standard deviation of the mean. Both curves show two transitions, but due to the shallow nature of the second transition, a melting temperature for this portion could not be obtained reliably. **(c)** The surface representation of Phe42 and Arg414 shows van der Waals interaction in the wild type, **(d)** but Cys414 in the R414C mutant is unable to retain this interaction, resulting in Phe42 to swing away. **(e,f)** Two different views of the electron densities around Cys414 in the R414C mutant. Black mesh represents weighted $2F_o-F_c$ contoured at 1.5σ . Green mesh represents positive F_o-F_c contoured at 3.0σ and is visible up to 5.0σ . Water molecules are shown as red spheres. All three domains are shown in white for clarity.

We observed extra electron densities associated with the Cys414 side chain that could not be modeled (Figure 4.9e,f). The positive F_o-F_c density was visible up to 5σ . This strongly suggests that Cys414 is reactive and is involved in cysteine modification, which is not surprising since Cys414 is exposed to the solvent, and swapping the bulky Arg for Cys makes the site more accessible to modifying agents. The likely combination of modifications by β ME and DTT (present at $\sim 1\text{mM}$ and $\sim 5\text{mM}$ in the sample, respectively), as well as being in multiple conformations, could explain the ambiguity in the electron densities that prevented the modeling of the structure. The modification at Cys414 would work as a “wedge” at the A-C interface and destabilize the domain-domain interaction. In fact, the R414C mutation destabilizes the protein by $\sim 3^{\circ}\text{C}$ (Figure 4.9b).

With the exception of R420Q, G230C, and R414C, all other mutant versions of RyR2ABC in this study behaved poorly and were heavily degraded upon extraction and during the first two chromatography steps. This is in sharp contrast with point mutations in RyR1ABC, where multiple mutations destabilized the protein, but could still be purified(209). L62F is located within exon3, at the interface between domains A and B (Figure 4.7c). There is no space for a bulkier Phe group, so domain rearrangements would be necessary. Phe329 is completely

buried within domain B, where it forms part of a hydrophobic core that consists of several Leu, Ile, and a Phe residues (Figure 4.7d). The F329L mutation thus introduces a smaller hydrophobic side chain, reducing the packing and destabilizing the folding of domain B. Thr415 is buried between two α helices within domain C (Figure 4.7e). There is no space for the much longer Arg side chain, so this residue would cause misfolding of domain C. The L433P mutation has previously been shown to reduce the luminal Ca^{2+} threshold at which Ca^{2+} release terminates(101). Leu433 is completely buried within domain C, where it is part of a hydrophobic core (Figure 4.7f). Mutation to a Pro residue has two effects: it affects the hydrophobic packing, and, being a helix breaker, it can also destabilize the α helix in domain C.

4.2.6 Putative ligand binding sites

For the wild-type crystal structure, extra density was observed in two areas near the interfaces of domains A and C and between domains A, B, and C (Figure 4.10). These densities were attributed to low molecular weight polyethylene glycol (PEG) molecules, which were used as cryo-protectant. High molecular weight (MW) PEG was used as a crystallization agent, but small amounts of low MW PEG are often present as contaminant. Using glycerol as cryo-protectant instead, some uninterpretable density remained at these sites, likely corresponding to disordered glycerol or partially occupied low MW PEG that could not be modeled reliably. The cryo-protectants were only used to soak existing crystals and, as expected, did not cause any significant rearrangements.

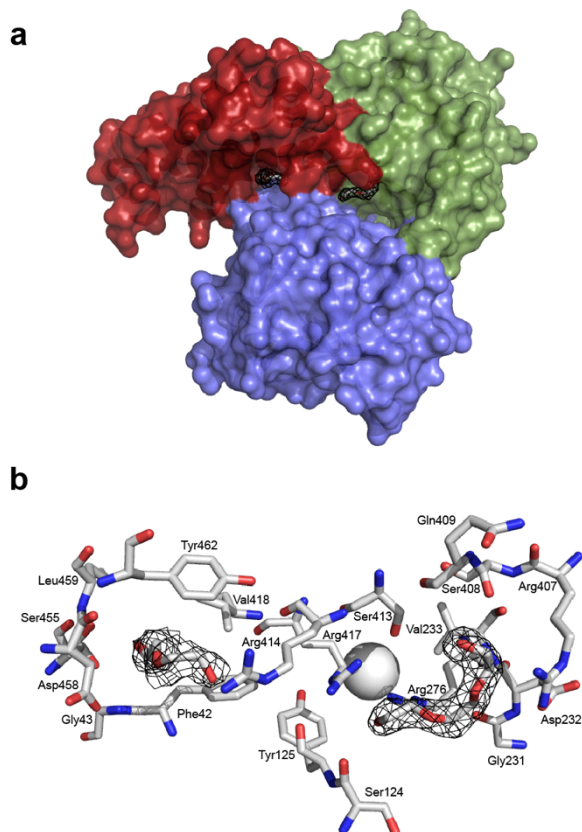


Figure 4.10: PEG binding sites. (a) Surface representation of RyR2ABC, showing two binding pockets for short polyethylene glycol (PEG) molecules. Coloring is according to Figure 4.1. Weighted $2F_o - F_c$ density is shown in black mesh, contoured at 1σ . The view is from the “bottom” compared to Figure 4.1, as viewed from the ER/SR lumen toward the cytosol. (b) Details of the two binding pockets, showing all residues within 4\AA . The chloride ion (sphere, not within 4\AA) is shown for reference.

Both PEG molecules bind in very deep pockets. Pocket 1 is located at the interface between domains A and C, whereas pocket 2 is located primarily between domains B and C. Although PEG molecules are not physiologically relevant, these pockets may form ideal sites for developing small molecules with higher affinity. Since many disease mutations seem to destabilize domain-domain interactions, targeting molecules to such pockets may stabilize the interactions and thus have therapeutic potential.

4.2.7 Interface 1 contains an additional α helix

In the process of solving multiple structures of RyR2ABC in different KCl concentrations, we have unexpectedly come across several structures for which the previously missing β 22- β 23 loop of domain B is now visible (Figure 4.11a). When superposed to RyR1ABC docked into the closed cryo-EM map of RyR1, the loop is found at the intersubunit interface 1 and is juxtaposed to the β 11- β 12 loop across the subunit (Figure 4.11b). Two residues in the loop are the targets of disease-associated mutations in RyR1 and RyR2 combined: Val377 and Arg383 (mouse RyR2 numbering). The middle portion of the loop forms an α -helix that contains Arg383.

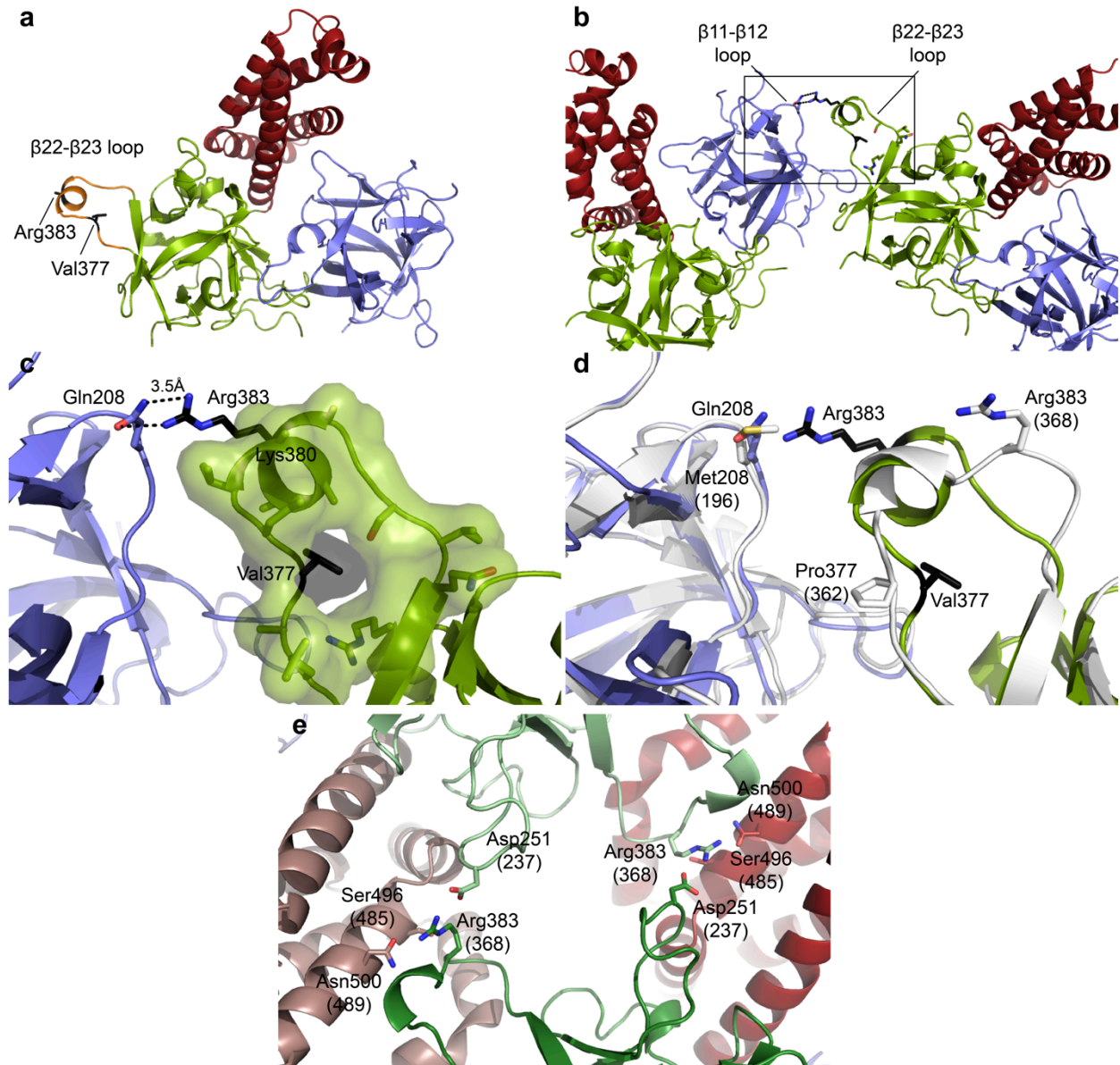


Figure 4.11: The structure of the $\beta 22$ - $\beta 23$ loop at interface 1. (a) The structure of the $\beta 22$ - $\beta 23$ loop within RyR2ABC is shown in orange. The two residues targeted by disease-associated mutations are colored in black. (b) Two subunits of RyR2ABC are shown after superposition with RyR1ABC (PDB accession code 2XOA) subunits according to their docked positions in the closed RyR1 cryo-EM reconstruction (EMDB accession code 1606). The interface 1 area is indicated with a box, whose enlarged views are shown in c and d. The two juxtaposing loops (the $\beta 11$ - $\beta 12$ and $\beta 22$ - $\beta 23$ loops) are labeled. (c) Close-up of the interface 1 that corresponds to the boxed area in b. Relevant side chains are represented in sticks. Disease targets (Val377 and Arg383) are shown in black. The

residues on the β 22- β 23 loop are shown in van der Waals surface representation, showing that the Val377 side chain is tightly packed inside the loop. The side chains of Gln208 and Arg383 are modeled from the most common rotamers. **(d)** Similar view as in **c**, but with the RyR1ABCD structure (white) superposed on top. The residue numbering in parentheses represent rabbit RyR1 numbering. **(e)** Two molecules of RyR1ABCD from the asymmetric unit of the crystal, where the Arg383 side chain is involved in contact with another molecule. One molecule is shown in lighter colors for clarity. The residue numbering in parentheses represents rabbit RyR1 numbering.

The V377M mutation in RyR2 is associated with CPVT(277). The Val377 side chain faces the tightly packed inner side of the β 22- β 23 loop (Figure 4.11c). The V377M mutation would replace a compact Val side chain for a long Met side chain, which would not be compatible in the tight space and would likely result in the destabilization of the loop, altering the interface 1 contact.

Since the β 22- β 23 loop is juxtaposed to the β 11- β 12 loop of domain A of a neighboring subunit, the two loops are the prime candidates for interacting partners at interface 1. Two charged residues reside in the α helix of the β 22- β 23 loop (Lys380 and Arg383), which could form salt bridges across the intersubunit. Lys380 faces away from domain A across the subunit and is unlikely to be involved in the interface 1 interaction. The observation that Lys380 is not found at any interface agrees with the fact that this residue is not a target for disease mutation even though the residue is conserved between the two isoforms. On the other hand, Arg383 is the target for two disease-causing mutations in RyR1: R383Q and R383L(285,286). Although the Arg383 side chain is flexible and could not be modeled in the crystal structure, when the most common rotamer is added to the residue, the side chain extends towards interface 1, close to Gln208. When the Gln208 side chain is replaced with the most common rotamer, the Arg383 and Gln208 side chains extend toward each other with 3.5Å distance in between, strongly suggesting

a formation of hydrogen bonds (Figure 4.11c). Gln208 is not a disease-mutation target and is not conserved across the isoforms. However, Arg383 is conserved, and the R383Q and R383L mutations would break the interaction across interface 1.

We compared the β 22- β 23 loop between RyR2 and RyR1 isoforms. The crystal structure of the longer construct RyR1ABCD (unpublished) also revealed the loop, but it contains a short 3_{10} helix instead of an α helix (Figure 4.11d). Also, Arg383 (or Arg368 in rabbit RyR1 numbering) is placed further away from interface 1, out of reach with the β 11- β 12 loop. The loop in RyR1ABCD, however, is involved in a contact between two molecules from the asymmetric unit of the crystal, and the loop conformation in the crystal structure could deviate from the physiological form (Figure 4.11e). Nonetheless, the interaction partner Gln208 in RyR2 is replaced with a Met residue in RyR1, and it is also possible that the nature of interface 1 contacts between the isoforms is truly different, which may explain the functional differences between the two.

4.3 Discussion

RyRs form large tetrameric assemblies that release Ca^{2+} from the SR or ER. Each subunit consists of many domains that have individual functions(27). Some form binding sites for auxiliary proteins or small molecule ligands, whereas others couple conformational changes in the transmembrane area to movements in the cytoplasmic head. The N-terminal area of RyR1 and RyR2 was previously described as a “hot spot” for disease-associated mutations that cause MH, CCD, CPVT, and other conditions. However, many more mutations are continuously found in between the originally defined hot spots, especially for RyR1 (Figure 1.2). Previous crystallographic studies of the RyR1 N-terminal region have shown that this area consists of three domains: two β -trefoil domains (domains A and B) and an armadillo repeat domain

(domain C). They are located in the cytoplasmic area, forming a continuous ring around the central four-fold symmetry axis(208). Comparison of this area in closed and open RyR1 cryo-EM maps shows that conformational changes in the pore are allosterically coupled to the N-terminal region(122). A plausible model suggests that channel opening results in the disruption of favorable intersubunit interactions, an event that requires an energetic penalty to be paid(209). As such, the N-terminal region would act as a brake on channel opening, and energy through binding of external ligands is required to open the channel. The N-terminal region of inositol-1,4,5-triphosphate receptors (IP₃Rs) shows a similar arrangement of three domains(234,235) and is also located within the cytoplasmic head near the four-fold symmetry axis(234).

The three mammalian RyR isoforms share a large amount of sequence conservation (~65%), but they differ strongly in their functional properties, such as their sensitivity to various inhibitory and activating ligands(24). Some of these differences may be attributed to divergent regions, three stretches within the sequence where the sequence conservation is very low. However, it is likely that some of these differences lie in the remaining >4,500 amino acids, despite their higher sequence conservation. Although we were previously able to crystallize the RyR1 N-terminal three domains, we wondered whether there might be intrinsic differences in this region between RyR1 and RyR2.

Our insights into the RyR2 N-terminal region were limited to the structure of the very N-terminal domain (“RyR2A”)(206), which did not allow us to peer into the interdomain contacts. In order to get further insights into the cardiac RyR, we solved the crystal structure of mouse RyR2 (residues 1-547), covering three N-terminal domains (A, B, and C). The structures of the individual domains are very similar to those in the skeletal muscle isoform (RyR1), but the interactions between these domains are surprisingly very different. In RyR1, the three domains

are kept in a compact conformation through a series of salt bridge interactions. This includes a central ion pair network involving four charged residues that are distributed over the three domains. Networks of ionic pairs are more stabilizing than individual ionic pairs because of the reduced desolvation penalties(287). As such, this network is a great contributor to the overall stability of the domain interactions. In RyR2ABC, however, this salt bridge network is disrupted by the addition of a chloride ion that occupies the space where the three domains meet and shields electrostatic repulsion created by several arginine residues. Although all four residues involved in the salt bridge network in RyR1 are conserved in RyR2, it seems to be specifically disrupted because of two mutations: H420R and H125Y (RyR2 numbering) (Figure 4.3a,b). Arg420 provides an extra ligand for the chloride ion, whereas Tyr125 forms a lid, preventing Arg417 to form salt bridges with Asp61 and Glu40. In addition, Tyr125 hydrogen bonds with the Arg420 side chain. Both Arg420 and Tyr125 are strongly conserved in mammalian RyR2 sequences, suggesting that they are both required for chloride binding (Figure 4.6).

RyRs are complex macromolecules that open and close in response to a range of stimuli. Previously, it has been reported that the activity of RyRs can be influenced by anions(288,289). For RyR2, titrated ryanodine binding was found to be higher in 250mM KCl versus 250mM KMes(290), suggesting that chloride can increase the activity of RyR2. However, in another study, chloride was found to have little or no effect on RyR2 Ca²⁺ release, and the effect likely depends on the extraction conditions(289). The ability of chloride to modulate RyR2 may be due to binding to the RyR2 N-terminal region. Removal of chloride has a large effect on the stability of the RyR2ABC protein, as it no longer shields repulsive interactions between arginines on different domains. Therefore, it is likely that removal or addition of chloride to this site has a functional consequence. The activity of RyR1 is also dependent on chloride, yet it does not

contain a chloride-binding site within the N-terminal region. Chloride dependence on activity may, therefore, be a complex event involving multiple sites, and the previously reported effect of chloride on RyR2 could be the result of multiple sites.

Could chloride binding to the N-terminal region within a physiological setting be a dynamic event that is regulated and provide a functional role, or is the chloride binding simply “structural” (that is, always bound)? The cytosolic concentration of chloride is in the low mM range, so the answer to this question depends on the inherent affinity. A high affinity would mean the site is always occupied, whereas an affinity in the low mM range would imply that RyR2 may exist in both chloride-bound and unbound conformations in physiological settings. Although chloride could be removed from RyR2ABC through dialysis, the protein readily precipitated at concentrations required to detect binding through, for example, isothermal titration calorimetry. As a result, we were unable to directly determine the affinity. We also dialyzed the protein at different levels of KCl and determined that at relatively high protein concentration (6.5 mg ml^{-1}), RyR2ABC is insoluble below 4mM KCl. However, crystal structures of RyR2ABC in the presence of 4mM KCl showed that chloride is fully occupied at the binding site, and thus we were also unable to measure the affinity indirectly.

We previously analyzed the effect of disease-associated mutations on the structure of RyR1ABC(209). Disease-associated mutations that abolish inter-domain salt bridges (R402G, D61N, and R45C in rabbit RyR1) resulted in relative domain reorientations. As the RyR2ABC protein could not be concentrated in the absence of chloride or bromide, we were unable to assess the effect of chloride removal on the structure. Removal of the chloride would not only take away favorable interactions, but it would also remove the shielding effect around repulsive interactions between several arginine residues. These would likely result in altered domain

orientations. It is not clear at this point which of the states (chloride-bound or chloride-free) would correspond to an activated state of the N-terminal region.

We expressed several disease-associated mutant forms of RyR2ABC. However, with the exception of R420Q, G230C, and R414C, all other mutants readily aggregated or showed signs of aggregation. It is possible that some of the RyR2ABC disease-associated mutations perturb the structures of the individual domains to a level that affects chloride binding, resulting again in repulsive interactions between the exposed arginine residues that further destabilize the protein.

Gly230 is buried near the domains A-B interface, and CPVT-associated G230C mutation destabilizes the N-terminal domains, as indicated by the lowered melting temperature and a large portion of the protein sample being degraded during the purification process. The corresponding residue in RyR1 is also the target for a disease-associated mutation (G216E in rabbit RyR1). We showed in Chapter 2 that G216E expressed well but did not crystallize, and because its CD spectra did not differ from the wild type, the mutation likely affects relative domain movements or increases the flexibility of the domains. This indicates that the tight turn formed by the Gly-Gly motif right before β 13 in domain B is critical for keeping the proper geometry at the domains A-B interface, and the same mutation in RyR2 may also alter domain-domain interfaces. Furthermore, a functional study revealed that the G230C mutation sensitizes RyR2 channel for activation by either cytosolic or luminal Ca^{2+} , suggesting a long-range crosstalk between N-terminal region and the luminal side of the channel with the pore(281). Opening of RyR has been shown to coincide with the allosteric motions of the channel and the disruption of the domains A-B interface across intersubunits(209), and it is likely that the G230C mutation in RyR2 facilitates the channel opening by destabilizing the domains A-B interface, ultimately altering the intersubunit contacts.

Arg414 is located at the domains A-C interface and is the target for two CPVT-associated mutations. The structure of the R414C mutant revealed that the overall structure of the protein is unchanged, although the mutation confers subtle changes at the A-C interface. More strikingly, the mutation seems to add a reactive cysteine, as indicated by the extra electron densities connected to Cys414 side chain. In the present study, the likely candidates for the modifying agents are β ME and DTT. Physiologically, known post-translational modifications on RyRs include glutathionylation and *S*-nitrosylation, both of which have been shown to regulate the channel(291). The mechanism of disease through the R414C mutation could be that it introduces a reactive cysteine that causes altered channel regulation through post-translational modification. The 3°C drop in the thermal stability of the R414C protein likely represents the combination of the subtle structural alteration at the A-C interface and the modification of Cys414 that introduces a “wedge” between the interface. The Cys414 modification would present a foreign moiety at the A-C interface and disrupt or alter the interface interaction, but the relative orientations of the three domains did not differ between the wild type and the mutant. Not seeing a domain-domain reorientation in the crystal structure could be that the crystal contact overcomes the tendency for the domains to rearrange. It is still possible that such movements occur in solution, where a reactive Cys414 facilitates the domain-domain shift. Future NMR studies may shed more light on this speculation, although it would be difficult given the size of the ABC construct.

Two RyR2 disease-associated mutations directly target the chloride binding site: R420Q and R420W. R420W has previously been shown to reduce the luminal Ca^{2+} threshold for Ca^{2+} release termination(101). We analyzed the structure of R420Q and found that chloride binding was abolished. Using the anomalous signal of bromide, we could detect some residual binding of

an anion at very high concentrations, but the occupancy was clearly much lower. In addition, the small perturbations around the chloride-binding site resulted in relative domain reorientations as a result of tilting around an axis near the domain-domain interfaces. Domains A and B maintain the same relative orientation, but both are displaced relative to domain C, with maximum shifts $\sim 1.4\text{\AA}$ furthest away from the tilting axis.

Disease-associated mutations at domain-domain interfaces are insightful on disease mechanisms, where they could weaken the interface interactions and facilitate domain-domain reorientations that lead to channel opening. However, mutations at interface 1 could provide direct evidence of this model since this interface is clearly broken when the channel opens(209). Through solving the structure of the $\beta 22\text{-}\beta 23$ loop at interface 1, we have identified the likely interaction partners at this interface, Gln208 and Arg383, which are within hydrogen-bond distance. Using this candidate interaction as a guide, future experiments may be able to establish more direct evidence of the involvement of interface 1 in the disease mechanism and channel gating.

The observations of domain reorientations are based on an isolated fragment, and the extent of conformational changes may be different in full-length RyR2. However, relative domain reorientations seem to become a common theme in the activation of calcium release channels. IP₃Rs are activated by the ligand IP₃, which binds to a pocket between domains B and C. The binding also causes a relative reorientation of the N-terminal domains(234,235). Thus, what is a regulatory event in IP₃Rs is a permanent event in several disease-associated mutant forms of both RyR1(209) and RyR2. The altered domain reorientations likely destabilize the intersubunit interface, resulting in facilitated channel opening(209,234).

Chapter 5: Conclusion

Ca^{2+} is a potent secondary messenger involved in major cellular processes, such as neurotransmission and muscle contraction. RyR is a Ca^{2+} release channel that plays a major part in E-C coupling by unleashing large amounts of Ca^{2+} from the SR/ER store into the cytoplasm. Three isoforms of RyR have been identified in mammals (RyR1 – RyR3). RyR1 is predominantly found in skeletal muscle, RyR2 in heart, and RyR3 is more ubiquitously expressed. RyR1 and RyR2 are the targets for over 500 disease-associated mutations, underlying the importance of its strict regulation.

Several cryo-EM studies revealed that all three isoforms of RyR resemble a mushroom structure: a huge cap in the cytoplasm and a smaller stem forming the transmembrane region that extends to the SR/ER lumen. RyR is a tetrameric channel, with each subunit comprised of globular domains. Due to its enormous size and its transmembrane nature, high-resolution structures of RyR have been lacking, greatly hampering our knowledge of the detailed mechanisms of normal and diseased-state functions of RyR. The average molecular weight of the available crystal structures in RCSB to date is ~80kDa, far below the full-length size of ~2.3MDa in RyR. In addition to its enormity, the transmembrane nature of RyR imposes difficulty in crystallization, requiring detergent extraction, which increases the mobility and heterogeneity in the sample. A few years ago, the first crystal structure of the very N-terminal domain of RyR1 and RyR2 became available, along with structural analyses of several disease-associated mutations at the periphery of the domain. However, a single-domain construct was insufficient to unambiguously dock the structure into the cryo-EM reconstruction of the full-

length RyR1. Thus the effect of the peripheral mutations remained elusive, although it was supposed that they affect the binding interface.

5.1 Pseudo-atomic structures

In this thesis, we described the crystal structures of the largest portion of RyR1 and RyR2 available to date that encompass three domains in the N-terminal region (RyR1ABC and RyR2ABC), harboring over 80 disease-associated mutations. Docking of RyR1ABC into the RyR1 cryo-EM reconstruction unambiguously placed the N-terminal region at the four-fold symmetry axis, forming a cytoplasmic vestibule. This enabled us to pinpoint the locations of the disease-associated mutations within the full-length channel, which revealed that the mutations are either buried within a domain or found at interfaces between domains or other parts of the channel. Combined with the observed allosteric motion in the region upon channel opening, we proposed a model whereby the disease-associated mutations in the N-terminal region of RyR facilitates channel opening through weakening the interfaces that undergo domain-domain reorientation during channel opening.

The RyR1ABC docking strategy proved the feasibility of the “divide and conquer” approach, in which high-resolution structures of small portions of RyR, in unit of domain, can be pieced together by creating a pseudo-atomic model inside the cryo-EM map. The four-fold symmetry inside the RyR tetramer greatly facilitates this process. Combined with phosphorylation domains, we have already uncovered ~11% of the entire RyR structure.

However, there are limitations and difficulties with this approach. Algorithms used for docking experiments tend to give high scores for crystal structures placed within electron dense regions of the cryo-EM map, such as the clamp region and column region in RyR. This “noise” is especially significant in small crystal structures, such as RyR1A, where the docking contrast

tends to be low. To compensate for this bias towards unspecific placing of fragments to electron dense regions, we have implemented a Laplacian filter in our RyR1ABC docking experiment, which takes into account surface contours of the fragment and the cryo-EM map, thus avoiding the nonspecific placement of a fragment inside electron dense regions with no matching surface features. This approach is especially useful for docking experiments in RyR, since the channel is comprised of multiple globular domains filled with numerous vestibules, each with unique surface contours.

In addition to the implementation of a Laplacian filter, there are several alternative techniques to validate the docking results. One approach is to compare the result from insertion studies, where extra density that arises from fusion protein, such as GFP or GST, is mapped onto the full-length RyR. However, limitations to this approach include the positioning of the insertion site, which may affect the fold of the protein and lead to artificial conformational changes. For example, difference density maps from two insertion studies prior to the availability of the RyR1ABC structure indicated the N-terminal region to be located at the clamp region, but the insertion sites were later found to be likely unfavorable for the proper fold of the protein, causing conformational changes outside the true location(143,144). Another important consideration is the length of the linker that tethers the fusion protein. If the linker were too short, it would hamper proper folding of RyR, but if it were too long, the extra density might appear far away from the true insertion site. These hurdles are easier to overcome using the crystal structure of the portions to be located in RyR. With the appropriate sites of insertion and linker length, fusion protein insertions within domains B and C of RyR2 indicated extra densities consistent with the RyR1ABC docking result, thus validating the docking study(239).

Another approach to validate the docking result is to perform a “superdocking” experiment, where structures of multiple domains of RyR are incorporated in one docking experiment. If one domain occupies a certain location of the full-length RyR, another domain should not overlap in the same location. Since ~11% of the cryo-EM reconstructions is already accounted for by the N-terminal and the phosphorylation domains, one only needs to locate other domains within the remaining ~89% of the area. This technique should prove useful as structures of more domains of RyR become available in the future.

Lastly, docking studies can be further validated through comparison with functional and binding studies. Does the docked position make sense in terms of previous reports of functional properties and protein interactions? The docked position of RyR1ABC, which is far away from the proposed FKBP binding site, was consistent with the failure to observe binding between RyR1ABC and FKBP. The locations of the disease-associated mutation sites in the N-terminal region, in which none of them pointed towards the outer surface of the channel, were also consistent with the failure to observe RyR1ABC binding to peripheral modulatory proteins and ligands. Instead, the sites of disease-associated mutations were distributed across six interfaces in the docked position, with some buried within a domain, indicating that the universal effect of the N-terminal mutations are to weaken the interdomain interfaces.

These validation techniques would be important especially in more difficult docking experiments, such as small fragments or domains sharing similar structural properties. The successful docking of the N-terminal portion of RyR1 brings promise to producing pseudo-atomic structures for the remaining part of RyR.

5.2 Models of disease mutation mechanisms

Two predominant models in the field describe the mechanism of disease-associated mutations in RyR: the zipper hypothesis and FKBP dissociation theory. We proposed an additional model in this thesis that describes the interfaces at the N-terminal region as a restraint in channel opening. Here, we compare our new model to the existing models.

The zipper hypothesis model states that the N-terminal region (residues 1-600) and the central region (residues 2000-2500) form an interdomain interaction that is broken, or “unzipped,” during channel opening through allosteric coupling(292,293). The supporting evidence of the model comes from spectroscopic measurements using peptides of central region, which was reported to competitively inhibit the binding of the endogenous central region to the N-terminal region and led to increased channel activity. This theory originated from the observation that a number of disease-associated mutations cluster in two hot spots in the cytoplasmic portion of RyR, the N-terminal and central regions. The results presented in the current thesis contradict this model because the majority of the disease-associated mutations harbored in the N-terminal region are buried within a domain, found at domain-domain interfaces, or located at the interface between the N-terminal subunits. We investigated these mutations that are buried or found at domain-domain interfaces and showed that they perturb the relative domain orientations, likely weakening the interfaces around the N-terminal region. In fact, the majority of the disease-target residues (66%) are already accounted for at the N-terminal interfaces and are not available for a direct interaction with the central region. The N-terminal region on its own, thus, already has a significant impact on the channel opening, and the zipper hypothesis does not describe a major mechanism, accounting only for 33% of the mutations at most. Also, direct binding of the N-terminal region and the central region has not been observed.

Furthermore, more and more disease-associated mutations are being identified outside of the previously proposed hot spots, and many agree that the notion of hot spots in the RyR has been the result of sequencing bias. Altogether, the theory that proposes a direct interaction between hot spots that no longer exist is no longer valid.

The difference between the two models likely arises from the techniques used. Peptides that are not properly folded can aggregate and cause unexpected, but nonspecific, interference in channel function and spectroscopic experiments. Our approach utilized soluble domains that are well behaved and properly folded. Continued effort of this approach would identify soluble domains of the central region, which then can be used to test direct binding to the N-terminal region. Also, by obtaining pseudo-atomic models of the central region, we could identify if the two regions are located close enough for interaction and whether disease mutations from the two regions share the same interface. Further functional experiments on the N-terminal region, such as cross-linking the intersubunit interface and seeing if the channel is locked in the closed state, may also show that the mutations in the N-terminal region alone can have an impact on channel function.

There are still remaining disease-associated mutations in the N-terminal region that are located at interfaces with other parts of the channel, which could be the central region. Thus, zipper hypothesis cannot be excluded, but the model should be redefined to include interdomain interactions within the N-terminal region. In addition, the experimental tactic of using ill-defined peptides should be replaced with our “divide and conquer” approach, in which soluble domains are identified and studied and then pieced together in a pseudo-atomic model.

Another model describes the disease-associated mutations in RyR as reductions in the affinity of FKBP, causing the dissociation of FKBP and, thus, destabilizing the closed state of

the channel(264). Again, the results in this thesis show otherwise. Our N-terminus construct failed to directly bind FKBP and is located far away from the proposed FKBP binding site in the clamp region of the channel. Furthermore, we have shown that the interfaces at the N-terminal region, the intersubunit interface in particular, are the prime targets of mutations and have proposed that they play an important role in regulating channel opening.

Although our results indicate that the mutations in the N-terminal region alone can already impact channel gating, it is possible that the FKBP dissociation model holds true in other parts of the channel. For instance, the study that supports this model used disease-associated mutations in the central region(264). In addition, we cannot exclude the possibility that the conformational changes at the N-terminal region indirectly alter the affinity for FKBP at the clamp region through allosteric coupling. In fact, we expect a reduced affinity for FKBP when RyRs open. The FKBP unbinding is, then, not the cause of channel opening but rather the effect. In this regard, the FKBP dissociation theory describes the epiphenomenon rather than the mechanism of channel opening. To further support this point, multitudes of functional studies, such as mutated RyRs expressed in HEK cells, demonstrated that the mutations alter the functions of RyR even in the absence of FKBP. Thus, it seems that the involvement of FKBP is not necessary for RyR mutations to cause perturbed channel activity. Future experiments using the domains that are located at the proposed FKBP binding site would clarify the exact effect of mutations around the FKBP binding interface.

Despite the differences, the existing models in the field and our model share a common theme, in which an allosteric coupling holds a key to channel regulation. This theme is also shared across the homologous Ca^{2+} release channel, IP_3R , where channel opening is triggered by ligand-dependent conformational changes at the N-terminal region. Thus, it has become

increasingly clear that allosteric movements throughout the entire channel are responsible for channel gating, and to understand this process, the detailed atomic structure of the entire channel, or a complete pseudo-atomic model, is necessary.

5.3 Ligand-dependent modulation

RyR activation is triggered by various ligands, such as Ca^{2+} , caffeine, and volatile anesthetics. Mutations in RyR rarely cause disease symptoms on their own, but usually require additional triggers, in the form of stress, heat, volatile anesthetics, *etc.* Ligand-dependent modulation of RyR, thus, seems to hold key for regulating the channel opening.

We have shown that the N-terminal region of RyR2 contains an anion-binding site at the core of the three domains. Although the functional significance of this binding site is yet to be investigated, the chloride shields the repulsive charges at the center of the three domains that replaces the stable salt-bridge networks in RyR1. The removal of this chloride in the form of CPVT-associated R420Q mutation caused domain-domain reorientation. The functional study of this mutant is not available, but the similar mutation R420W has been reported to cause gain of function. Furthermore, we have proposed a model where the domain reorientations in the N-terminal region of RyR1 causes channel opening, in much like the way IP_3R opens upon ligand-dependent domain reorientation in the N-terminal region. Therefore, it seems that destabilizing the N-terminal region of RyR leads to channel opening. For the majority of the mutations that cause a gain of function, it would be attractive to stabilize the N-terminal domains in order to compensate for the oversensitivity of the diseased-state channel towards activators.

The affinity of chloride toward RyR2ABC, based on our preliminary results, seems to be at the physiological level of chloride (0-4mM). In many cell types, including the skeletal muscle and neurons, whose intracellular chloride levels are ~3-4mM(294,295), we can expect the

chloride binding at an equilibrium. On the other hand, a chloride ion may bind to RyR2ABC at a mostly full occupancy in other cell types with much higher intracellular chloride concentrations, such as epithelial cells (~40mM)(296) and ventricular cells (~25mM)(297). The chloride binding at the RyR2 N-terminus, thus, could function as a regulatory mechanism in a cell-type dependent manner, in which the ion can bind and unbind according to the chloride flux in some cell types or stay permanently bound to provide a structural stability in other cell types. We have shown that chloride can also be replaced with bromide. It is possible that other anions that are physiologically relevant, such as phosphate, can bind at the same site. Anions that are either smaller or larger than chloride may be able to bind RyR2 at different affinities, and this could be a way to control the binding affinity. Future functional experiments of the wild type and R420Q mutant channels in varying levels of chloride and other anions would clarify the effect of the anion binding at the N-terminal region.

We have also identified other ligands that could potentially modulate the N-terminal domain stability. The R414C mutation destabilized the N-terminal region likely through cysteine modification that puts a wedge between domains A and C. There is currently no functional data on this mutation. Future functional experiments of the R414C channel would clarify if this mutation causes gain of function through redox modification.

Furthermore, we have shown PEG binding sites at intradomain interfaces of RyR2ABC. PEG is not physiologically relevant and high levels were required for the binding, but the binding pockets between the domains could accommodate other molecules that could stabilize the interfaces.

Although the N-terminal constructs failed to bind currently known modulators of RyR, larger construct may reveal binding sites in the future. In addition, the N-terminal region in its

physiological tetramer form, for example through cross-linking, might reveal a ligand-binding site at the intersubunit interface.

Taken together, we have shown that the N-terminal region of RyR harbor key interfaces that are broken upon channel opening and are targeted by disease-associated mutations that weaken such interfaces. Stabilizing these domain-domain interfaces through ligands would be of therapeutic value, where channels over-sensitized towards activators via mutations could be compensated.

5.4 Future directions

We have combined structural and biochemical data to propose an attractive mechanism for mutations at the N-terminal region of RyRs. Here, we propose the next set of experiments that involves obtaining functional data for mutant channels to relate the structural data to the channel gating properties. Functional studies can be performed using the planar lipid bilayer electrophysiology on an intact channel, which enables the observation of single channel properties, including open probability, duration of open/closed time, and conductance.

The RyR1ABC mutants showed variations in the degree of structural changes. Are there correlations between the degree of structural changes or thermal destabilization and channel gating properties? In particular, salt bridge mutants, such as R45C, displayed long-range domain reorientations. Does the R45C mutant channel have properties different from other types of mutants that display only local structural changes, such as the C36R mutant? In addition, would the mutants with only modest structural changes also confer modest changes in functional studies? If the mutant channels display a similar degree of channel activation regardless of the different degrees of structural changes in the crystal structures, then it could suggest that modest

structural changes in the crystal structures are the reflection of rigid restraints due to the crystal packing and that all mutations destabilize the domain-domain interfaces to a similar extent.

Another crucial study is to test the functional consequence of the intersubunit interface between the four subunits of N-terminal regions. Is the motion in the N-terminal region directly coupled to the channel gating? This could be tested by locking the domain-domain interfaces in the region through disulfide bonds or cross-linking. One candidate is one of the salt bridges at the A-C interface that are targeted by disease mutations, such as Arg45 and Asp447 (rabbit RyR1 numbering). Another candidate is the proposed intersubunit interface contact, Gln208 and Arg383 (mouse RyR2 numbering). If locking the interfaces prevents the channel opening, it would serve as a direct evidence for the allosteric coupling of N-terminal motions and channel gating. If the intersubunit interface can be locked through disulfide bonds or crosslinking, it would also be of great interest to obtain the crystal structure of the RyRABC protein in tetramer form. By doing so, we can gain better understanding of the nature of the intersubunit contact area, since the current ABC structure in isolation contains several flexible loops, and the contact area in the absence of the neighboring subunits is unclear.

The N-terminal region of RyR2 contains a unique chloride-binding site, and the preliminary data suggest that this anion-binding site could have a functional role. The R420Q mutation abolishes the anion binding and results in a domain-domain reorientation. Could this mutant confer gain of function through removing chloride from the N-terminal region? We can perform functional studies comparing channel opening between the wildtype and R420Q channels in the presence of different chloride concentrations. Previous studies showed that the wildtype channels are activated by chloride. This could be due to other chloride-binding sites elsewhere on the channel. By directly comparing the wildtype with a mutant that no longer binds

chloride at the N-terminal region, the effect of the anion binding in this region can be determined. The effect of chloride can be calcium dependent, so that we would perform functional studies using varying levels of chloride and calcium.

The structure of the R414C mutant suggested that the mutation may introduce a reactive Cys that can be modified at the A-C interface. Previous studies, using mass spectroscopy, have identified several Cys residues in RyR that are redox modified. The same experiment can be repeated for the R414C mutant channel. Also, functional studies of the R414C mutant channel can test if the mutant channels are sensitive to redox modification.

By continuing studies on the N-terminal region of RyRs using planar lipid bilayer experiments and combining the structural and functional data, we can get a better, fuller picture of the mutation mechanism at this region. By verifying the importance of the N-terminal domain-domain interfaces in the channel gating through functional studies, we can justify the pursuit of molecules that can stabilize the contacts, which would have therapeutic values in RyR channelopathies.

References

1. Rogers, E. F., and Koniuszy, F. R. (1948) Plant insecticides; ryanodine, a new alkaloid from *Ryania speciosa* Vahl. *J. Am. Chem. Soc.* **70**, 3086-3088
2. Meissner, G. (1986) Ryanodine activation and inhibition of the Ca²⁺ release channel of sarcoplasmic reticulum. *J. Biol. Chem.* **261**, 6300-6306
3. Takeshima, H., Nishimura, S., Matsumoto, T., Ishida, H., Kangawa, K., Minamino, N., Matsuo, H., Ueda, M., Hanaoka, M., and Hirose, T. (1989) Primary structure and expression from complementary DNA of skeletal muscle ryanodine receptor. *Nature* **339**, 439-445
4. Otsu, K., Willard, H. F., Khanna, V. K., Zorzato, F., Green, N. M., and MacLennan, D. H. (1990) Molecular cloning of cDNA encoding the Ca²⁺ release channel (ryanodine receptor) of rabbit cardiac muscle sarcoplasmic reticulum. *J. Biol. Chem.* **265**, 13472-13483
5. Hakamata, Y., Nakai, J., Takeshima, H., and Imoto, K. (1992) Primary structure and distribution of a novel ryanodine receptor/calcium release channel from rabbit brain. *FEBS Lett.* **312**, 229-235
6. Sorrentino, V., and Volpe, P. (1993) Ryanodine receptors: how many, where and why? *Trends Pharmacol. Sci.* **14**, 98-103
7. Endo, M. (2009) Calcium-induced calcium release in skeletal muscle. *Physiol. Rev.* **89**, 1153-1176
8. Rios, E., and Brum, G. (1987) Involvement of dihydropyridine receptors in excitation-contraction coupling in skeletal muscle. *Nature* **325**, 717-720

9. Tanabe, T., Beam, K. G., Powell, J. A., and Numa, S. (1988) Restoration of excitation-contraction coupling and slow calcium current in dysgenic muscle by dihydropyridine receptor complementary DNA. *Nature* **336**, 134-139
10. Block, B. A., Imagawa, T., Campbell, K. P., and Franzini-Armstrong, C. (1988) Structural evidence for direct interaction between the molecular components of the transverse tubule/sarcoplasmic reticulum junction in skeletal muscle. *J. Cell Biol.* **107**, 2587-2600
11. Tanabe, T., Beam, K. G., Adams, B. A., Niidome, T., and Numa, S. (1990) Regions of the skeletal muscle dihydropyridine receptor critical for excitation-contraction coupling. *Nature* **346**, 567-569
12. Saito, A., Seiler, S., Chu, A., and Fleischer, S. (1984) Preparation and morphology of sarcoplasmic reticulum terminal cisternae from rabbit skeletal muscle. *J. Cell Biol.* **99**, 875-885
13. Smith, D. S. (1966) The organization and function of the sarcoplasmic reticulum and T-system of muscle cells. *Prog. Biophys. Mol. Biol.* **16**, 107-142
14. Betzenhauser, M. J., and Marks, A. R. (2010) Ryanodine receptor channelopathies. *Pflugers Arch.* **460**, 467-480
15. Gillard, E. F., Otsu, K., Fujii, J., Khanna, V. K., de Leon, S., Derdemezi, J., Britt, B. A., Duff, C. L., Worton, R. G., and MacLennan, D. H. (1991) A substitution of cysteine for arginine 614 in the ryanodine receptor is potentially causative of human malignant hyperthermia. *Genomics* **11**, 751-755
16. Jungbluth, H., Sewry, C. A., and Muntoni, F. (2003) What's new in neuromuscular disorders? The congenital myopathies. *Eur. J. Paediatr. Neurol.* **7**, 23-30

17. Priori, S. G., Napolitano, C., Tiso, N., Memmi, M., Vignati, G., Bloise, R., Sorrentino, V., and Danieli, G. A. (2001) Mutations in the cardiac ryanodine receptor gene (hRyR2) underlie catecholaminergic polymorphic ventricular tachycardia. *Circulation* **103**, 196-200
18. Priori, S. G., Napolitano, C., Memmi, M., Colombi, B., Drago, F., Gasparini, M., DeSimone, L., Coltorti, F., Bloise, R., and Keegan, R. (2002) Clinical and molecular characterization of patients with catecholaminergic polymorphic ventricular tachycardia. *Circulation* **106**, 69-74
19. Kushnir, A., and Marks, A. R. (2010) The ryanodine receptor in cardiac physiology and disease. *Adv. Pharmacol.* **59**, 1-30
20. Bers, D. M. (2004) Macromolecular complexes regulating cardiac ryanodine receptor function. *J. Mol. Cell. Cardiol.* **37**, 417-429
21. Zalk, R., Lehnart, S. E., and Marks, A. R. (2007) Modulation of the ryanodine receptor and intracellular calcium. *Annu. Rev. Biochem.* **76**, 367-385
22. Lanner, J. T., Georgiou, D. K., Joshi, A. D., and Hamilton, S. L. (2010) Ryanodine receptors: structure, expression, molecular details, and function in calcium release. *Cold Spring Harb. Perspect. Biol.* **2**, a003996
23. Marx, S. (2003) Ion channel macromolecular complexes in the heart. *J. Mol. Cell. Cardiol.* **35**, 37-44
24. Fill, M., and Copello, J. A. (2002) Ryanodine receptor calcium release channels. *Physiol. Rev.* **82**, 893-922

25. Palade, P., Mitchell, R. D., and Fleischer, S. (1983) Spontaneous calcium release from sarcoplasmic reticulum. General description and effects of calcium. *J. Biol. Chem.* **258**, 8098-8107
26. Jiang, D., Xiao, B., Yang, D., Wang, R., Choi, P., Zhang, L., Cheng, H., and Chen, S. R. W. (2004) RyR2 mutations linked to ventricular tachycardia and sudden death reduce the threshold for store-overload-induced Ca²⁺ release (SOICR). *Proc. Natl. Acad. Sci. U.S.A.* **101**, 13062-13067
27. Van Petegem, F. (2012) Ryanodine receptors: structure and function. *J. Biol. Chem.* **287**, 31624-31632
28. Revel, J. P. (1962) The sarcoplasmic reticulum of the bat cricothyroid muscle. *J. Cell Biol.* **12**, 571-588
29. Franzini-Armstrong, C. (1970) Studies of the Triad: I. Structure of the Junction in Frog Twitch Fibers. *J. Cell Biol.* **47**, 488-499
30. McCarthy, T. V., Quane, K. A., and Lynch, P. J. (2000) Ryanodine receptor mutations in malignant hyperthermia and central core disease. *Hum. Mutat.* **15**, 410-417
31. Monnier, N., Procaccio, V., Stieglitz, P., and Lunardi, J. (1997) Malignant-hyperthermia susceptibility is associated with a mutation of the alpha 1-subunit of the human dihydropyridine-sensitive L-type voltage-dependent calcium-channel receptor in skeletal muscle. *Am. J. Hum. Genet.* **60**, 1316-1325
32. Rosenberg, H., Davis, M., James, D., Pollock, N., and Stowell, K. (2007) Malignant hyperthermia. *Orphanet J. Rare Dis.* **2**, 21

33. MacLennan, D. H., and Zvaritch, E. (2011) Mechanistic models for muscle diseases and disorders originating in the sarcoplasmic reticulum. *Biochim. Biophys. Acta* **1813**, 948-964
34. Krause, T., Gerbershagen, M. U., Fiege, M., Weisshorn, R., and Wappler, F. (2004) Dantrolene--a review of its pharmacology, therapeutic use and new developments. *Anaesthesia* **59**, 364-373
35. Paul-Pletzer, K., Yamamoto, T., Bhat, M. B., Ma, J., Ikemoto, N., Jimenez, L. S., Morimoto, H., Williams, P. G., and Parness, J. (2002) Identification of a dantrolene-binding sequence on the skeletal muscle ryanodine receptor. *J. Biol. Chem.* **277**, 34918-34923
36. Zhao, F., Li, P., Chen, S. R., Louis, C. F., and Fruen, B. R. (2001) Dantrolene inhibition of ryanodine receptor Ca²⁺ release channels. Molecular mechanism and isoform selectivity. *J. Biol. Chem.* **276**, 13810-13816
37. Szentesi, P., Collet, C., Sárközi, S., Szegedi, C., Jona, I., Jacquemond, V., Kovács, L., and Csernoch, L. (2001) Effects of dantrolene on steps of excitation-contraction coupling in mammalian skeletal muscle fibers. *J. Gen. Physiol.* **118**, 355-375
38. Fujii, J., Otsu, K., Zorzato, F., de Leon, S., Khanna, V. K., Weiler, J. E., O'Brien, P. J., and MacLennan, D. H. (1991) Identification of a mutation in porcine ryanodine receptor associated with malignant hyperthermia. *Science* **253**, 448-451
39. Klingler, W., Rueffert, H., Lehmann-Horn, F., Girard, T., and Hopkins, P. M. (2009) Core myopathies and risk of malignant hyperthermia. *Anesth. Analg.* **109**, 1167-1173
40. Robinson, R., Carpenter, D., Shaw, M.-A., Halsall, J., and Hopkins, P. (2006) Mutations in RYR1 in malignant hyperthermia and central core disease. *Hum. Mutat.* **27**, 977-989

41. Denborough, M. A., Dennett, X., and Anderson, R. M. (1973) Central-core disease and malignant hyperpyrexia. *Br. Med. J.* **1**, 272-273
42. Jungbluth, H., Zhou, H., Hartley, L., Halliger-Keller, B., Messina, S., Longman, C., Brockington, M., Robb, S. A., Straub, V., Voit, T., Swash, M., Ferreiro, A., Bydder, G., Sewry, C. A., Müller, C., and Muntoni, F. (2005) Minicore myopathy with ophthalmoplegia caused by mutations in the ryanodine receptor type 1 gene. *Neurology* **65**, 1930-1935
43. Ferreiro, A., Quijano-Roy, S., Pichereau, C., Moghadaszadeh, B., Goemans, N., Bönnemann, C., Jungbluth, H., Straub, V., Villanova, M., Leroy, J.-P., Romero, N. B., Martin, J.-J., Muntoni, F., Voit, T., Estournet, B., Richard, P., Fardeau, M., and Guicheney, P. (2002) Mutations of the selenoprotein N gene, which is implicated in rigid spine muscular dystrophy, cause the classical phenotype of multiminicore disease: reassessing the nosology of early-onset myopathies. *Am. J. Hum. Genet.* **71**, 739-749
44. Juryneec, M. J., Xia, R., Mackrill, J. J., Gunther, D., Crawford, T., Flanigan, K. M., Abramson, J. J., Howard, M. T., and Grunwald, D. J. (2008) Selenoprotein N is required for ryanodine receptor calcium release channel activity in human and zebrafish muscle. *Proc. Natl. Acad. Sci. U.S.A.* **105**, 12485-12490
45. Kaindl, A. M., Rüschenndorf, F., Krause, S., Goebel, H. H., Koehler, K., Becker, C., Pongratz, D., Müller-Höcker, J., Nürnberg, P., Stoltenburg-Didinger, G., Lochmüller, H., and Huebner, A. (2004) Missense mutations of ACTA1 cause dominant congenital myopathy with cores. *J. Med. Genet.* **41**, 842-848
46. Lahat, H., Pras, E., Olender, T., Avidan, N., Ben-Asher, E., Man, O., Levy-Nissenbaum, E., Khoury, A., Lorber, A., Goldman, B., Lancet, D., and Eldar, M. (2001) A missense

- mutation in a highly conserved region of CASQ2 is associated with autosomal recessive catecholamine-induced polymorphic ventricular tachycardia in Bedouin families from Israel. *Am. J. Hum. Genet.* **69**, 1378-1384
47. Roux-Buisson, N., Cacheux, M., Fourest-Lieuvain, A., Fauconnier, J., Brocard, J., Denjoy, I., Durand, P., Guicheney, P., Kyndt, F., Leenhardt, A., Le Marec, H., Lucet, V., Mabo, P., Probst, V., Monnier, N., Ray, P. F., Santoni, E., Trémeaux, P., Lacampagne, A., Faure, J., Lunardi, J., and Marty, I. (2012) Absence of triadin, a protein of the calcium release complex, is responsible for cardiac arrhythmia with sudden death in human. *Hum. Mol. Genet.* **21**, 2759-2767
48. Nyegaard, M., Overgaard, M. T., Søndergaard, M. T., Vranas, M., Behr, E. R., Hildebrandt, L. L., Lund, J., Hedley, P. L., Camm, A. J., Wettrell, G., Fosdal, I., Christiansen, M., and Børghlum, A. D. (2012) Mutations in calmodulin cause ventricular tachycardia and sudden cardiac death. *Am. J. Hum. Genet.* **91**, 703-712
49. Pflaumer, A., and Davis, A. M. (2012) Guidelines for the diagnosis and management of Catecholaminergic Polymorphic Ventricular Tachycardia. *Heart Lung Circ.* **21**, 96-100
50. Watanabe, H., Chopra, N., Laver, D., Hwang, H. S., Davies, S. S., Roach, D. E., Duff, H. J., Roden, D. M., Wilde, A. A. M., and Knollmann, B. C. (2009) Flecainide prevents catecholaminergic polymorphic ventricular tachycardia in mice and humans. *Nat. Med.* **15**, 380-383
51. Ohnishi, S. T., Taylor, S., and Gronert, G. A. (1983) Calcium-induced Ca²⁺ release from sarcoplasmic reticulum of pigs susceptible to malignant hyperthermia. The effects of halothane and dantrolene. *FEBS Lett.* **161**, 103-107

52. Nelson, T. E. (1983) Abnormality in calcium release from skeletal sarcoplasmic reticulum of pigs susceptible to malignant hyperthermia. *J. Clin. Invest.* **72**, 862-870
53. Wehner, M., Rueffert, H., Koenig, F., Neuhaus, J., and Olthoff, D. (2002) Increased sensitivity to 4-chloro-*m*-cresol and caffeine in primary myotubes from malignant hyperthermia susceptible individuals carrying the ryanodine receptor 1 Thr2206Met (C6617T) mutation. *Clin. Genet.* **62**, 135-146
54. Wehner, M., Rueffert, H., Koenig, F., Meinecke, C.-D., and Olthoff, D. (2003) The Ile2453Thr mutation in the ryanodine receptor gene 1 is associated with facilitated calcium release from sarcoplasmic reticulum by 4-chloro-*m*-cresol in human myotubes. *Cell Calcium* **34**, 163-168
55. Wehner, M., Rueffert, H., Koenig, F., and Olthoff, D. (2004) Functional characterization of malignant hyperthermia-associated RyR1 mutations in exon 44, using the human myotube model. *Neuromuscul. Disord.* **14**, 429-437
56. Kaufmann, A., Kraft, B., Michalek-Sauberer, A., Weindlmayr, M., Kress, H. G., Steinboeck, F., and Weigl, L. G. (2012) Novel double and single ryanodine receptor 1 variants in two Austrian malignant hyperthermia families. *Anesth. Analg.* **114**, 1017-1025
57. Chelu, M. G., Goonasekera, S. A., Durham, W. J., Tang, W., Lueck, J. D., Riehl, J., Pessah, I. N., Zhang, P., Bhattacharjee, M. B., Dirksen, R. T., and Hamilton, S. L. (2006) Heat- and anesthesia-induced malignant hyperthermia in an RyR1 knock-in mouse. *The FASEB J.* **20**, 329-330
58. Yang, T., Riehl, J., Esteve, E., Matthaei, K. I., Goth, S., Allen, P. D., Pessah, I. N., and Lopez, J. R. (2006) Pharmacologic and functional characterization of malignant hyperthermia in the R163C RyR1 knock-in mouse. *Anesthesiology* **105**, 1164-1175

59. Liu, N., Colombi, B., Memmi, M., Zissimopoulos, S., Rizzi, N., Negri, S., Imbriani, M., Napolitano, C., Lai, F. A., and Priori, S. G. (2006) Arrhythmogenesis in catecholaminergic polymorphic ventricular tachycardia: insights from a RyR2 R4496C knock-in mouse model. *Circ. Res.* **99**, 292-298
60. Feng, W., Barrientos, G. C., Cherednichenko, G., Yang, T., Padilla, I. T., Truong, K., Allen, P. D., Lopez, J. R., and Pessah, I. N. (2011) Functional and biochemical properties of ryanodine receptor type 1 channels from heterozygous R163C malignant hyperthermia-susceptible mice. *Mol. Pharmacol.* **79**, 420-431
61. Boncompagni, S., Loy, R. E., Dirksen, R. T., and Franzini-Armstrong, C. (2010) The I4895T mutation in the type 1 ryanodine receptor induces fiber-type specific alterations in skeletal muscle that mimic premature aging. *Aging Cell* **9**, 958-970
62. Loy, R. E., Orynbayev, M., Xu, L., Andronache, Z., Apostol, S., Zvaritch, E., MacLennan, D. H., Meissner, G., Melzer, W., and Dirksen, R. T. (2011) Muscle weakness in Ryr1I4895T/WT knock-in mice as a result of reduced ryanodine receptor Ca²⁺ ion permeation and release from the sarcoplasmic reticulum. *J. Gen. Physiol.* **137**, 43-57
63. Barrientos, G. C., Feng, W., Truong, K., Matthaei, K. I., Yang, T., Allen, P. D., Lopez, J. R., and Pessah, I. N. (2012) Gene dose influences cellular and calcium channel dysregulation in heterozygous and homozygous T4826I-RYR1 malignant hyperthermia-susceptible muscle. *J. Biol. Chem.* **287**, 2863-2876
64. Ghassemi, F., Vukcevic, M., Xu, L., Zhou, H., Meissner, G., Muntoni, F., Jungbluth, H., Zorzato, F., and Treves, S. (2009) A recessive ryanodine receptor 1 mutation in a CCD patient increases channel activity. *Cell Calcium* **45**, 192-197

65. Tilgen, N., Zorzato, F., Halliger-Keller, B., Muntoni, F., Sewry, C., Palmucci, L. M., Schneider, C., Hauser, E., Lehmann-Horn, F., Müller, C. R., and Treves, S. (2001) Identification of four novel mutations in the C-terminal membrane spanning domain of the ryanodine receptor 1: association with central core disease and alteration of calcium homeostasis. *Hum. Mol. Genet.* **10**, 2879-2887
66. Zorzato, F., Yamaguchi, N., Xu, L., Meissner, G., Müller, C. R., Pouliquin, P., Muntoni, F., Sewry, C., Girard, T., and Treves, S. (2003) Clinical and functional effects of a deletion in a COOH-terminal lumenal loop of the skeletal muscle ryanodine receptor. *Hum. Mol. Genet.* **12**, 379-388
67. Avila, G., O'Brien, J. J., and Dirksen, R. T. (2001) Excitation--contraction uncoupling by a human central core disease mutation in the ryanodine receptor. *Proc. Natl. Acad. Sci. U.S.A.* **98**, 4215-4220
68. Avila, G., and Dirksen, R. T. (2001) Functional effects of central core disease mutations in the cytoplasmic region of the skeletal muscle ryanodine receptor. *J. Gen. Physiol.* **118**, 277-290
69. Yang, T., Ta, T. A., Pessah, I. N., and Allen, P. D. (2003) Functional defects in six ryanodine receptor isoform-1 (RyR1) mutations associated with malignant hyperthermia and their impact on skeletal excitation-contraction coupling. *J. Biol. Chem.* **278**, 25722-25730
70. Avila, G., O'Connell, K. M. S., and Dirksen, R. T. (2003) The pore region of the skeletal muscle ryanodine receptor is a primary locus for excitation-contraction uncoupling in central core disease. *J. Gen. Physiol.* **121**, 277-286

71. Tong, J., Oyamada, H., Demaurex, N., Grinstein, S., McCarthy, T. V., and MacLennan, D. H. (1997) Caffeine and halothane sensitivity of intracellular Ca²⁺ release is altered by 15 calcium release channel (ryanodine receptor) mutations associated with malignant hyperthermia and/or central core disease. *J. Biol. Chem.* **272**, 26332-26339
72. Du, G. G., and MacLennan, D. H. (1998) Functional consequences of mutations of conserved, polar amino acids in transmembrane sequences of the Ca²⁺ release channel (ryanodine receptor) of rabbit skeletal muscle sarcoplasmic reticulum. *J. Biol. Chem.* **273**, 31867-31872
73. Lynch, P. J., Tong, J., Lehane, M., Mallet, A., Giblin, L., Heffron, J. J., Vaughan, P., Zafra, G., MacLennan, D. H., and McCarthy, T. V. (1999) A mutation in the transmembrane/luminal domain of the ryanodine receptor is associated with abnormal Ca²⁺ release channel function and severe central core disease. *Proc. Natl. Acad. Sci. U.S.A.* **96**, 4164-4169
74. Tong, J., McCarthy, T. V., and MacLennan, D. H. (1999) Measurement of resting cytosolic Ca²⁺ concentrations and Ca²⁺ store size in HEK-293 cells transfected with malignant hyperthermia or central core disease mutant Ca²⁺ release channels. *J. Biol. Chem.* **274**, 693-702
75. Du, G. G., Oyamada, H., Khanna, V. K., and MacLennan, D. H. (2001) Mutations to Gly2370, Gly2373 or Gly2375 in malignant hyperthermia domain 2 decrease caffeine and cresol sensitivity of the rabbit skeletal-muscle Ca²⁺-release channel (ryanodine receptor isoform 1). *Biochem. J.* **360**, 97-105
76. Sambuughin, N., Nelson, T. E., Jankovic, J., Xin, C., Meissner, G., Mullakandov, M., Ji, J., Rosenberg, H., Sivakumar, K., and Goldfarb, L. G. (2001) Identification and

- functional characterization of a novel ryanodine receptor mutation causing malignant hyperthermia in North American and South American families. *Neuromuscul. Disord.* **11**, 530-537
77. Treves, S., Larini, F., Menegazzi, P., Steinberg, T. H., Koval, M., Vilsen, B., Andersen, J. P., and Zorzato, F. (1994) Alteration of intracellular Ca²⁺ transients in COS-7 cells transfected with the cDNA encoding skeletal-muscle ryanodine receptor carrying a mutation associated with malignant hyperthermia. *Biochem. J.* **301**, 661
78. Otsu, K., Nishida, K., Kimura, Y., Kuzuya, T., Hori, M., Kamada, T., and Tada, M. (1994) The point mutation Arg615-->Cys in the Ca²⁺ release channel of skeletal sarcoplasmic reticulum is responsible for hypersensitivity to caffeine and halothane in malignant hyperthermia. *J. Biol. Chem.* **269**, 9413-9415
79. Jiang, D., Wang, R., Xiao, B., Kong, H., Hunt, D. J., Choi, P., Zhang, L., and Chen, S. R. W. (2005) Enhanced store overload-induced Ca²⁺ release and channel sensitivity to luminal Ca²⁺ activation are common defects of RyR2 mutations linked to ventricular tachycardia and sudden death. *Circ. Res.* **97**, 1173-1181
80. George, C. H., Higgs, G. V., and Lai, F. A. (2003) Ryanodine receptor mutations associated with stress-induced ventricular tachycardia mediate increased calcium release in stimulated cardiomyocytes. *Circ. Res.* **93**, 531-540
81. George, C. H., Jundi, H., Walters, N., Thomas, N. L., West, R. R., and Lai, F. A. (2006) Arrhythmogenic mutation-linked defects in ryanodine receptor autoregulation reveal a novel mechanism of Ca²⁺ release channel dysfunction. *Circ. Res.* **98**, 88-97
82. Cerrone, M., Colombi, B., Santoro, M., di Barletta, M. R., Scelsi, M., Villani, L., Napolitano, C., and Priori, S. G. (2005) Bidirectional ventricular tachycardia and

- fibrillation elicited in a knock-in mouse model carrier of a mutation in the cardiac ryanodine receptor. *Circ. Res.* **96**, e77-82
83. Kannankeril, P. J., Mitchell, B. M., Goonasekera, S. A., Chelu, M. G., Zhang, W., Sood, S., Kearney, D. L., Danila, C. I., De Biasi, M., Wehrens, X. H. T., Pautler, R. G., Roden, D. M., Taffet, G. E., Dirksen, R. T., Anderson, M. E., and Hamilton, S. L. (2006) Mice with the R176Q cardiac ryanodine receptor mutation exhibit catecholamine-induced ventricular tachycardia and cardiomyopathy. *Proc. Natl. Acad. Sci. U.S.A.* **103**, 12179-12184
84. Mickelson, J. R., Gallant, E. M., Litterer, L. A., Johnson, K. M., Rempel, W. E., and Louis, C. F. (1988) Abnormal sarcoplasmic reticulum ryanodine receptor in malignant hyperthermia. *J. Biol. Chem.* **263**, 9310-9315
85. Fill, M., Coronado, R., Mickelson, J. R., Vilven, J., Ma, J. J., Jacobson, B. A., and Louis, C. F. (1990) Abnormal ryanodine receptor channels in malignant hyperthermia. *Biophys. J.* **57**, 471-475
86. Du, G. G., Khanna, V. K., Guo, X., and MacLennan, D. H. (2004) Central core disease mutations R4892W, I4897T and G4898E in the ryanodine receptor isoform 1 reduce the Ca²⁺ sensitivity and amplitude of Ca²⁺-dependent Ca²⁺ release. *Biochem. J.* **382**, 557-564
87. Jiang, D., Xiao, B., Zhang, L., and Chen, S. R. W. (2002) Enhanced basal activity of a cardiac Ca²⁺ release channel (ryanodine receptor) mutant associated with ventricular tachycardia and sudden death. *Circ. Res.* **91**, 218-225

88. Mickelson, J. R., Litterer, L. A., Jacobson, B. A., and Louis, C. F. (1990) Stimulation and inhibition of [3H]ryanodine binding to sarcoplasmic reticulum from malignant hyperthermia susceptible pigs. *Arch. Biochem. Biophys.* **278**, 251-257
89. Shomer, N. H., Louis, C. F., Fill, M., Litterer, L. A., and Mickelson, J. R. (1993) Reconstitution of abnormalities in the malignant hyperthermia-susceptible pig ryanodine receptor. *Am. J. Physiol.* **264**, C125-135
90. Nelson, T. E. (1992) Halothane effects on human malignant hyperthermia skeletal muscle single calcium-release channels in planar lipid bilayers. *Anesthesiology* **76**, 588-595
91. Ohnishi, S. T. (1987) Effects of halothane, caffeine, dantrolene and tetracaine on the calcium permeability of skeletal sarcoplasmic reticulum of malignant hyperthermic pigs. *Biochim. Biophys. Acta* **897**, 261-268
92. Jiang, D., Chen, W., Xiao, J., Wang, R., Kong, H., Jones, P. P., Zhang, L., Fruen, B., and Chen, S. R. W. (2008) Reduced threshold for luminal Ca²⁺ activation of RyR1 underlies a causal mechanism of porcine malignant hyperthermia. *J. Biol. Chem.* **283**, 20813-20820
93. Liang, X., Chen, K., Fruen, B., Hu, J., Ma, J., Hu, X., and Parness, J. (2009) Impaired interaction between skeletal ryanodine receptors in malignant hyperthermia. *Integr. Biol.* **1**, 533
94. Brini, M., Manni, S., Pierobon, N., Du, G. G., Sharma, P., MacLennan, D. H., and Carafoli, E. (2005) Ca²⁺ signaling in HEK-293 and skeletal muscle cells expressing recombinant ryanodine receptors harboring malignant hyperthermia and central core disease mutations. *J. Biol. Chem.* **280**, 15380-15389
95. Zvaritch, E., Depreux, F., Kraeva, N., Loy, R. E., Goonasekera, S. A., Boncompagni, S., Boncompagni, S., Kraev, A., Gramolini, A. O., Dirksen, R. T., Franzini-Armstrong, C.,

- Seidman, C. E., Seidman, J. G., and MacLennan, D. H. (2007) An Ryr1I4895T mutation abolishes Ca²⁺ release channel function and delays development in homozygous offspring of a mutant mouse line. *Proc. Natl. Acad. Sci. U.S.A.* **104**, 18537-18542
96. Xu, L., Wang, Y., Yamaguchi, N., Pasek, D. A., and Meissner, G. (2008) Single channel properties of heterotetrameric mutant RyR1 ion channels linked to core myopathies. *J. Biol. Chem.* **283**, 6321-6329
97. Sato, K., Pollock, N., and Stowell, K. M. (2010) Functional studies of RYR1 mutations in the skeletal muscle ryanodine receptor using human RYR1 complementary DNA. *Anesthesiology* **112**, 1350-1354
98. Haraki, T., Yasuda, T., Mukaida, K., Migita, T., Hamada, H., and Kawamoto, M. (2011) Mutated p.4894 RyR1 function related to malignant hyperthermia and congenital neuromuscular disease with uniform type 1 fiber (CNMDU1). *Anesth. Analg.* **113**, 1461-1467
99. Jiang, D., Chen, W., Wang, R., Zhang, L., and Chen, S. R. W. (2007) Loss of luminal Ca²⁺ activation in the cardiac ryanodine receptor is associated with ventricular fibrillation and sudden death. *Proc. Natl. Acad. Sci. U.S.A.* **104**, 18309-18314
100. Jones, P. P., Jiang, D., Bolstad, J., Hunt, D. J., Zhang, L., Demarex, N., and Chen, S. R. W. (2008) Endoplasmic reticulum Ca²⁺ measurements reveal that the cardiac ryanodine receptor mutations linked to cardiac arrhythmia and sudden death alter the threshold for store-overload-induced Ca²⁺ release. *Biochem. J.* **412**, 171-178
101. Tang, Y., Tian, X., Wang, R., Fill, M., and Chen, S. R. W. (2012) Abnormal termination of Ca²⁺ release is a common defect of RyR2 mutations associated with cardiomyopathies. *Circ. Res.* **110**, 968-977

102. Radermacher, M., Rao, V., Grassucci, R., Frank, J., Timerman, A. P., Fleischer, S., and Wagenknecht, T. (1994) Cryo-electron microscopy and three-dimensional reconstruction of the calcium release channel/ryanodine receptor from skeletal muscle. *J. Cell Biol.* **127**, 411-423
103. Zhou, H., Yamaguchi, N., Xu, L., Wang, Y., Sewry, C., Jungbluth, H., Zorzato, F., Bertini, E., Muntoni, F., Meissner, G., and Treves, S. (2006) Characterization of recessive RYR1 mutations in core myopathies. *Hum. Mol. Genet.* **15**, 2791-2803
104. Zhou, H., Lillis, S., Loy, R. E., Ghassemi, F., Rose, M. R., Norwood, F., Mills, K., Al-Sarraj, S., Lane, R. J. M., Feng, L., Matthews, E., Sewry, C. A., Abbs, S., Buk, S., Hanna, M., Treves, S., Dirksen, R. T., Meissner, G., Muntoni, F., and Jungbluth, H. (2010) Multi-minicore disease and atypical periodic paralysis associated with novel mutations in the skeletal muscle ryanodine receptor (RYR1) gene. *Neuromuscul. Disord.* **20**, 166-173
105. Bonilla, E. (1977) Staining of transverse tubular system of skeletal muscle by tannic acid-glutaraldehyde fixation. *J. Ultrastruct. Res.*, 162-165
106. Somlyo, A. V. (1979) Bridging structures spanning the junctioning gap at the triad of skeletal muscle. *J. Cell Biol.* **80**, 743-750
107. Ferguson, D. G., Schwartz, H. W., and Franzini-Armstrong, C. (1984) Subunit structure of junctional feet in triads of skeletal muscle: a freeze-drying, rotary-shadowing study. *J. Cell Biol.* **99**, 1735-1742
108. Inui, M., Saito, A., and Fleischer, S. (1987) Purification of the ryanodine receptor and identity with feet structures of junctional terminal cisternae of sarcoplasmic reticulum from fast skeletal muscle. *J. Biol. Chem.* **262**, 1740-1747

109. Saito, A., Inui, M., Radermacher, M., Frank, J., and Fleischer, S. (1988) Ultrastructure of the calcium release channel of sarcoplasmic reticulum. *J. Cell Biol.* **107**, 211-219
110. Yin, C. C., and Lai, F. A. (2000) Intrinsic lattice formation by the ryanodine receptor calcium-release channel. *Nat. Cell Biol.* **2**, 669-671
111. Yin, C.-C., Han, H., Wei, R., and Lai, F. A. (2005) Two-dimensional crystallization of the ryanodine receptor Ca²⁺ release channel on lipid membranes. *J. Struct. Biol.* **149**, 219-224
112. Wagenknecht, T., Grassucci, R., Frank, J., Saito, A., Inui, M., and Fleischer, S. (1989) Three-dimensional architecture of the calcium channel/foot structure of sarcoplasmic reticulum. *Nature* **338**, 167-170
113. Radermacher, M., Wagenknecht, T., Grassucci, R., Frank, J., Inui, M., Chadwick, C., and Fleischer, S. (1992) Cryo-EM of the native structure of the calcium release channel/ryanodine receptor from sarcoplasmic reticulum. *Biophys. J.* **61**, 936-940
114. Serysheva, I. I., Orlova, E. V., Chiu, W., Sherman, M. B., Hamilton, S. L., and van Heel, M. (1995) Electron cryomicroscopy and angular reconstitution used to visualize the skeletal muscle calcium release channel. *Nat. Struct. Biol.* **2**, 18-24
115. Sharma, M. R., Penczek, P., Grassucci, R., Xin, H. B., Fleischer, S., and Wagenknecht, T. (1998) Cryoelectron microscopy and image analysis of the cardiac ryanodine receptor. *J. Biol. Chem.* **273**, 18429-18434
116. Jeyakumar, L. H., Copello, J. A., O'Malley, A. M., Wu, G. M., Grassucci, R., Wagenknecht, T., and Fleischer, S. (1998) Purification and characterization of ryanodine receptor 3 from mammalian tissue. *J. Biol. Chem.* **273**, 16011-16020

117. Murayama, T., Oba, T., Katayama, E., Oyamada, H., Oguchi, K., Kobayashi, M., Otsuka, K., and Ogawa, Y. (1999) Further characterization of the type 3 ryanodine receptor (RyR3) purified from rabbit diaphragm. *J. Biol. Chem.* **274**, 17297-17308
118. Sharma, M. R., Jeyakumar, L. H., Fleischer, S., and Wagenknecht, T. (2000) Three-dimensional structure of ryanodine receptor isoform three in two conformational states as visualized by cryo-electron microscopy. *J. Biol. Chem.* **275**, 9485-9491
119. Ludtke, S. J., Serysheva, I. I., Hamilton, S. L., and Chiu, W. (2005) The pore structure of the closed RyR1 channel. *Structure* **13**(8), 1203-1211
120. Serysheva, I. I., Ludtke, S. J., Baker, M. L., Cong, Y., Topf, M., Eramian, D., Sali, A., Hamilton, S. L., and Chiu, W. (2008) Subnanometer-resolution electron cryomicroscopy-based domain models for the cytoplasmic region of skeletal muscle RyR channel. *Proc. Natl. Acad. Sci. U.S.A.* **105**, 9610-9615
121. Samsó, M., Wagenknecht, T., and Allen, P. D. (2005) Internal structure and visualization of transmembrane domains of the RyR1 calcium release channel by cryo-EM. *Nat. Struct. Mol. Biol.* **12**(6), 539-544
122. Samsó, M., Feng, W., Pessah, I. N., and Allen, P. D. (2009) Coordinated movement of cytoplasmic and transmembrane domains of RyR1 upon gating. *PLoS Biol.* **7**, e85
123. Minor, D. L. (2005) Bend to open? *Structure* **13**(8), 1094-1095
124. Frank, J. (2002) Single-particle imaging of macromolecules by cryo-electron microscopy. *Annu. Rev. Biophys. Biomol. Struct.* **31**, 303-319
125. van Heel, M., and Schatz, M. (2005) Fourier shell correlation threshold criteria. *J. Struct. Biol.* **151**, 250-262

126. Ludtke, S. J., and Serysheva, I. I. (2013) Single-particle cryo-EM of calcium release channels: structural validation. *Curr. Opin. Struct. Biol.* **23**, 755-762
127. Du, G. G., Avila, G., Sharma, P., Khanna, V. K., Dirksen, R. T., and MacLennan, D. H. (2004) Role of the sequence surrounding predicted transmembrane helix M4 in membrane association and function of the Ca(2+) release channel of skeletal muscle sarcoplasmic reticulum (ryanodine receptor isoform 1). *J. Biol. Chem.* **279**, 37566-37574
128. Doyle, D. A., Cabral, J. M., Pfuetzner, R. A., Kuo, A., Gulbis, J. M., Cohen, S. L., Chait, B. T., and MacKinnon, R. (1998) The structure of the potassium channel: molecular basis of K⁺ conduction and selectivity. *Science* **280**, 69-77
129. Jiang, Y., Lee, A., Chen, J., Cadene, M., Chait, B. T., and MacKinnon, R. (2002) The open pore conformation of potassium channels. *Nature* **417**, 523-526
130. D'Avanzo, N., Cho, H. C., Tolokh, I., Pekhletski, R., Tolokh, I., Gray, C., Goldman, S., and Backx, P. H. (2005) Conduction through the inward rectifier potassium channel, Kir2.1, is increased by negatively charged extracellular residues. *J. Gen. Physiol.* **125**, 493-503
131. Imoto, K., Busch, C., Sakmann, B., Mishina, M., Konno, T., Nakai, J., Bujo, H., Mori, Y., Fukuda, K., and Numa, S. (1988) Rings of negatively charged amino acids determine the acetylcholine receptor channel conductance. *Nature* **335**, 645-648
132. Andersen, C., Koronakis, E., Hughes, C., and Koronakis, V. (2002) An aspartate ring at the TolC tunnel entrance determines ion selectivity and presents a target for blocking by large cations. *Mol. Microbiol.* **44**, 1131-1139

133. Terlau, H., Heinemann, S. H., Stühmer, W., Pusch, M., Conti, F., Imoto, K., and Numa, S. (1991) Mapping the site of block by tetrodotoxin and saxitoxin of sodium channel II. *FEBS Lett.* **293**, 93-96
134. Long, S. B., Campbell, E. B., and MacKinnon, R. (2005) Voltage sensor of Kv1.2: structural basis of electromechanical coupling. *Science* **309**, 903-908
135. Kuo, A., Gulbis, J. M., Antcliff, J. F., Rahman, T., Lowe, E. D., Zimmer, J., Cuthbertson, J., Ashcroft, F. M., Ezaki, T., and Doyle, D. A. (2003) Crystal structure of the potassium channel KirBac1.1 in the closed state. *Science* **300**, 1922-1926
136. Baker, M. L., Ju, T., and Chiu, W. (2007) Identification of secondary structure elements in intermediate-resolution density maps. *Structure* **15**, 7-19
137. Nishida, M., Cadene, M., Chait, B. T., and MacKinnon, R. (2007) Crystal structure of a Kir3.1-prokaryotic Kir channel chimera. *EMBO J.* **26**, 4005-4015
138. Nishida, M., and MacKinnon, R. (2002) Structural basis of inward rectification: cytoplasmic pore of the G protein-gated inward rectifier GIRK1 at 1.8 Å resolution. *Cell* **111**, 957-965
139. Pegan, S., Arrabit, C., Zhou, W., Kwiatkowski, W., Collins, A., Slesinger, P. A., and Choe, S. (2005) Cytoplasmic domain structures of Kir2.1 and Kir3.1 show sites for modulating gating and rectification. *Nat. Neurosci.* **8**, 279-287
140. Zagotta, W. N., Olivier, N. B., Black, K. D., Young, E. C., Olson, R., and Gouaux, E. (2003) Structural basis for modulation and agonist specificity of HCN pacemaker channels. *Nature* **425**, 200-205

141. Orlova, E. V., Serysheva, I. I., van Heel, M., Hamilton, S. L., and Chiu, W. (1996) Two structural configurations of the skeletal muscle calcium release channel. *Nat. Struct. Biol.* **3**, 547-552
142. Serysheva, I. I., Schatz, M., van Heel, M., Chiu, W., and Hamilton, S. L. (1999) Structure of the Skeletal Muscle Calcium Release Channel Activated with Ca(2+) and AMP-PCP. *Biophys. J.* **77**, 1936-1944
143. Liu, Z., Zhang, J., Sharma, M. R., Li, P., Chen, S. R., and Wagenknecht, T. (2001) Three-dimensional reconstruction of the recombinant type 3 ryanodine receptor and localization of its amino terminus. *Proc. Natl. Acad. Sci. U.S.A.* **98**, 6104-6109
144. Wang, R., Chen, W., Cai, S., Zhang, J., Bolstad, J., Wagenknecht, T., Liu, Z., and Chen, S. R. W. (2007) Localization of an NH(2)-terminal disease-causing mutation hot spot to the "clamp" region in the three-dimensional structure of the cardiac ryanodine receptor. *J. Biol. Chem.* **282**, 17785-17793
145. Paul-Pletzer, K., Yamamoto, T., Ikemoto, N., Jimenez, L. S., Morimoto, H., Williams, P. G., Ma, J., and Parness, J. (2005) Probing a putative dantrolene-binding site on the cardiac ryanodine receptor. *Biochem. J.* **387**, 905-909
146. Wang, R., Zhong, X., Meng, X., Koop, A., Tian, X., Jones, P. P., Fruen, B. R., Wagenknecht, T., Liu, Z., and Chen, S. R. W. (2011) Localization of the dantrolene-binding sequence near the FK506-binding protein-binding site in the three-dimensional structure of the ryanodine receptor. *J. Biol. Chem.* **286**, 12202-12212
147. Liu, Z., Wang, R., Zhang, J., Chen, S. R. W., and Wagenknecht, T. (2005) Localization of a disease-associated mutation site in the three-dimensional structure of the cardiac muscle ryanodine receptor. *J. Biol. Chem.* **280**, 37941-37947

148. Ikemoto, N., and Yamamoto, T. (2002) Regulation of calcium release by interdomain interaction within ryanodine receptors. *Front. Biosci.* **7**, d671-683
149. Tian, X., Liu, Y., Liu, Y., Wang, R., Wagenknecht, T., Liu, Z., and Chen, S. R. W. (2013) Ligand-dependent conformational changes in the clamp region of the cardiac ryanodine receptor. *J. Biol. Chem.* **288**, 4066-4075
150. Du, G. G., Khanna, V. K., and MacLennan, D. H. (2000) Mutation of divergent region 1 alters caffeine and Ca(2+) sensitivity of the skeletal muscle Ca(2+) release channel (ryanodine receptor). *J. Biol. Chem.* **275**, 11778-11783
151. Du, G. G., and MacLennan, D. H. (1999) Ca(2+) inactivation sites are located in the COOH-terminal quarter of recombinant rabbit skeletal muscle Ca(2+) release channels (ryanodine receptors). *J. Biol. Chem.* **274**, 26120-26126
152. Nakai, J., Gao, L., Xu, L., Xin, C., Pasek, D. A., and Meissner, G. (1999) Evidence for a role of C-terminus in Ca(2+) inactivation of skeletal muscle Ca(2+) release channel (ryanodine receptor). *FEBS Lett.* **459**, 154-158
153. Benacquista, B. L., Sharma, M. R., Samsó, M., Zorzato, F., Treves, S., and Wagenknecht, T. (2000) Amino acid residues 4425–4621 localized on the three-dimensional structure of the skeletal muscle ryanodine receptor. *Biophys. J.* **78**, 1349-1358
154. Liu, Z., Zhang, J., Li, P., Chen, S. R. W., and Wagenknecht, T. (2002) Three-dimensional reconstruction of the recombinant type 2 ryanodine receptor and localization of its divergent region 1. *J. Biol. Chem.* **277**, 46712-46719
155. Yamazawa, T., Takeshima, H., Shimuta, M., and Iino, M. (1997) A region of the ryanodine receptor critical for excitation-contraction coupling in skeletal muscle. *J. Biol. Chem.* **272**, 8161-8164

156. Perez, C. F., Mukherjee, S., and Allen, P. D. (2003) Amino acids 1-1,680 of ryanodine receptor type 1 hold critical determinants of skeletal type for excitation-contraction coupling. Role of divergence domain D2. *J. Biol. Chem.* **278**, 39644-39652
157. Liu, Z., Zhang, J., Wang, R., Wayne Chen, S. R., and Wagenknecht, T. (2004) Location of divergent region 2 on the three-dimensional structure of cardiac muscle ryanodine receptor/calcium release channel. *J. Mol. Biol.* **338**, 533-545
158. Hayek, S. M., Zhao, J., Bhat, M., Xu, X., Nagaraj, R., Pan, Z., Takeshima, H., and Ma, J. (1999) A negatively charged region of the skeletal muscle ryanodine receptor is involved in Ca(2+)-dependent regulation of the Ca(2+) release channel. *FEBS Lett.* **461**, 157-164
159. Hayek, S. M., Zhu, X., Bhat, M. B., Zhao, J., Takeshima, H., Valdivia, H. H., and Ma, J. (2000) Characterization of a calcium-regulation domain of the skeletal-muscle ryanodine receptor. *Biochem. J.* **351**, 57-65
160. Proenza, C., O'Brien, J., Nakai, J., Mukherjee, S., Allen, P. D., and Beam, K. G. (2002) Identification of a region of RyR1 that participates in allosteric coupling with the alpha(1S) (Ca(V)1.1) II-III loop. *J. Biol. Chem.* **277**, 6530-6535
161. Koop, A., Goldmann, P., Chen, S. R. W., Thieleczek, R., and Varsányi, M. (2008) ARVC-related mutations in divergent region 3 alter functional properties of the cardiac ryanodine receptor. *Biophys. J.* **94**, 4668-4677
162. Zhang, J., Liu, Z., Masumiya, H., Wang, R., Jiang, D., Li, F., Wagenknecht, T., and Chen, S. R. W. (2003) Three-dimensional localization of divergent region 3 of the ryanodine receptor to the clamp-shaped structures adjacent to the FKBP binding sites. *J. Biol. Chem.* **278**, 14211-14218

163. Danila, C. I., and Hamilton, S. L. (2004) Phosphorylation of ryanodine receptors. *Biol. Res.* **37**, 521-525
164. Petrovic, M. M., Vales, K., Putnikovic, B., Djulejic, V., and Mitrovic, D. M. (2008) Ryanodine receptors, voltage-gated calcium channels and their relationship with protein kinase A in the myocardium. *Physiol. Res.* **57**, 141-149
165. Wehrens, X. H. T., Lehnart, S. E., Reiken, S., Vest, J. A., Wronska, A., and Marks, A. R. (2006) Ryanodine receptor/calcium release channel PKA phosphorylation: a critical mediator of heart failure progression. *Proc. Natl. Acad. Sci. U.S.A.* **103**, 511-518
166. Xiao, B., Jiang, M. T., Zhao, M., Yang, D., Sutherland, C., Lai, F. A., Walsh, M. P., Warltier, D. C., Cheng, H., and Chen, S. R. W. (2005) Characterization of a novel PKA phosphorylation site, serine-2030, reveals no PKA hyperphosphorylation of the cardiac ryanodine receptor in canine heart failure. *Circ. Res.* **96**, 847-855
167. Xiao, B., Zhong, G., Obayashi, M., Yang, D., Chen, K., Walsh, M. P., Shimoni, Y., Cheng, H., ter Keurs, H., and Chen, S. R. W. (2006) Ser-2030, but not Ser-2808, is the major phosphorylation site in cardiac ryanodine receptors responding to protein kinase A activation upon beta-adrenergic stimulation in normal and failing hearts. *Biochem. J.* **396**, 7-16
168. Jones, P. P., Meng, X., Xiao, B., Cai, S., Bolstad, J., Wagenknecht, T., Liu, Z., and Chen, S. R. W. (2008) Localization of PKA phosphorylation site, Ser(2030), in the three-dimensional structure of cardiac ryanodine receptor. *Biochem. J.* **410**, 261-270
169. Meng, X., Xiao, B., Cai, S., Huang, X., Li, F., Bolstad, J., Trujillo, R., Airey, J., Chen, S. R. W., Wagenknecht, T., and Liu, Z. (2007) Three-dimensional localization of serine

- 2808, a phosphorylation site in cardiac ryanodine receptor. *J. Biol. Chem.* **282**, 25929-25939
170. Ahern, G. P., Junankar, P. R., and Dulhunty, A. F. (1997) Subconductance states in single-channel activity of skeletal muscle ryanodine receptors after removal of FKBP12. *Biophys. J.* **72**, 146-162
171. Chelu, M. G., Danila, C. I., Gilman, C. P., and Hamilton, S. L. (2004) Regulation of ryanodine receptors by FK506 binding proteins. *Trends Cardiovasc. Med.* **14**(6), 227-234
172. Marx, S. O., Reiken, S., Hisamatsu, Y., Jayaraman, T., Burkhoff, D., Rosemlit, N., and Marks, A. R. (2000) PKA phosphorylation dissociates FKBP12.6 from the calcium release channel (ryanodine receptor): defective regulation in failing hearts. *Cell* **101**, 365-376
173. Jayaraman, T., Brillantes, A. M., Timerman, A. P., Fleischer, S., Erdjument-Bromage, H., Tempst, P., and Marks, A. R. (1992) FK506 binding protein associated with the calcium release channel (ryanodine receptor). *J. Biol. Chem.* **267**, 9474-9477
174. Timerman, A. P., Onoue, H., Xin, H. B., Barg, S., Copello, J., Wiederrecht, G., and Fleischer, S. (1996) Selective binding of FKBP12.6 by the cardiac ryanodine receptor. *J. Biol. Chem.* **271**, 20385-20391
175. Wagenknecht, T., Grassucci, R., Berkowitz, J., Wiederrecht, G. J., Xin, H.-B., and Fleischer, S. (1996) Cryoelectron microscopy resolves FK506-binding protein sites on the skeletal muscle ryanodine receptor. *Biophys. J.* **70**, 1709-1715
176. Wagenknecht, T., Radermacher, M., Grassucci, R., Berkowitz, J., Xin, H. B., and Fleischer, S. (1997) Locations of calmodulin and FK506-binding protein on the three-

- dimensional architecture of the skeletal muscle ryanodine receptor. *J. Biol. Chem.* **272**, 32463-32471
177. Burkhard, P., Taylor, P., and Walkinshaw, M. D. (2000) X-ray structures of small ligand-FKBP complexes provide an estimate for hydrophobic interaction energies. *J. Mol. Biol.* **295**, 953-962
178. Samsó, M., Shen, X., and Allen, P. D. (2006) Structural characterization of the RyR1-FKBP12 interaction. *J. Mol. Biol.* **356**, 917-927
179. Sharma, M. R., Jeyakumar, L. H., Fleischer, S., and Wagenknecht, T. (2006) Three-dimensional visualization of FKBP12.6 binding to an open conformation of cardiac ryanodine receptor. *Biophys. J.* **90**, 164-172
180. Wagenknecht, T., Berkowitz, J., Grassucci, R., Timerman, A. P., and Fleischer, S. (1994) Localization of calmodulin binding sites on the ryanodine receptor from skeletal muscle by electron microscopy. *Biophys. J.* **67**, 2286-2295
181. Samsó, M., and Wagenknecht, T. (2002) Apocalmodulin and Ca²⁺-calmodulin bind to neighboring locations on the ryanodine receptor. *J. Biol. Chem.* **277**, 1349-1353
182. Ikemoto, T., Iino, M., and Endo, M. (1995) Enhancing effect of calmodulin on Ca²⁺-induced Ca²⁺ release in the sarcoplasmic reticulum of rabbit skeletal muscle fibres. *J. Physiol.* **487 (Pt 3)**, 573-582
183. Tripathy, A., Xu, L., Mann, G., and Meissner, G. (1995) Calmodulin activation and inhibition of skeletal muscle Ca²⁺ release channel (ryanodine receptor). *Biophys. J.* **69**, 106-119

184. Buratti, R., Prestipino, G., Menegazzi, P., Treves, S., and Zorzato, F. (1995) Calcium dependent activation of skeletal muscle Ca²⁺ release channel (ryanodine receptor) by calmodulin. *Biochem. Biophys. Res. Commun.* **213**, 1082-1090
185. Board, P. G., Coggan, M., Watson, S., Gage, P. W., and Dulhunty, A. F. (2004) CLIC-2 modulates cardiac ryanodine receptor Ca²⁺ release channels. *Int. J. Biochem. Cell Biol.* **36**, 1599-1612
186. Littler, D. R., Harrop, S. J., Goodchild, S. C., Phang, J. M., Mynott, A. V., Jiang, L., Valenzuela, S. M., Mazzanti, M., Brown, L. J., Breit, S. N., and Curmi, P. M. G. (2010) The enigma of the CLIC proteins: Ion channels, redox proteins, enzymes, scaffolding proteins? *FEBS Lett.* **584**, 2093-2101
187. Meng, X., Wang, G., Viero, C., Wang, Q., Mi, W., Su, X.-D., Wagenknecht, T., Williams, A. J., Liu, Z., and Yin, C.-C. (2009) CLIC2-RyR1 interaction and structural characterization by cryo-electron microscopy. *J. Mol. Biol.* **387**, 320-334
188. Tripathy, A., Resch, W., Xu, L., Valdivia, H. H., and Meissner, G. (1998) Imperatoxin A induces subconductance states in Ca²⁺ release channels (ryanodine receptors) of cardiac and skeletal muscle. *J. Gen. Physiol.* **111**, 679-690
189. Gurrola, G. B., Arévalo, C., Sreekumar, R., Lokuta, A. J., Walker, J. W., and Valdivia, H. H. (1999) Activation of ryanodine receptors by imperatoxin A and a peptide segment of the II-III loop of the dihydropyridine receptor. *J. Biol. Chem.* **274**, 7879-7886
190. Samso, M., Trujillo, R., Gurrola, G. B., Valdivia, H. H., and Wagenknecht, T. (1999) Three-dimensional location of the imperatoxin A binding site on the ryanodine receptor. *J. Cell Biol.* **146**, 493-499

191. Zhou, Q., Wang, Q.-L., Meng, X., Shu, Y., Jiang, T., Wagenknecht, T., Yin, C.-C., Sui, S.-F., and Liu, Z. (2008) Structural and functional characterization of ryanodine receptor-natratin toxin interaction. *Biophys. J.* **95**, 4289-4299
192. Maximciuc, A. A., Putkey, J. A., Shamoo, Y., and MacKenzie, K. R. (2006) Complex of calmodulin with a ryanodine receptor target reveals a novel, flexible binding mode. *Structure* **14**, 1547-1556
193. Wright, N. T., Prosser, B. L., Varney, K. M., Zimmer, D. B., Schneider, M. F., and Weber, D. J. (2008) S100A1 and calmodulin compete for the same binding site on ryanodine receptor. *J. Biol. Chem.* **283**, 26676-26683
194. Balshaw, D. M., Xu, L., Yamaguchi, N., Pasek, D. A., and Meissner, G. (2001) Calmodulin binding and inhibition of cardiac muscle calcium release channel (ryanodine receptor). *J. Biol. Chem.* **276**, 20144-20153
195. Yamaguchi, N., Xu, L., Pasek, D. A., Evans, K. E., and Meissner, G. (2003) Molecular basis of calmodulin binding to cardiac muscle Ca²⁺ release channel (ryanodine receptor). *J. Biol. Chem.* **278**, 23480-23486
196. Xiong, L.-W., Newman, R. A., Rodney, G. G., Thomas, O., Zhang, J.-Z., Persechini, A., Shea, M. A., and Hamilton, S. L. (2002) Lobe-dependent regulation of ryanodine receptor type 1 by calmodulin. *J. Biol. Chem.* **277**, 40862-40870
197. Zhang, H., Zhang, J.-Z., Danila, C. I., and Hamilton, S. L. (2003) A noncontiguous, intersubunit binding site for calmodulin on the skeletal muscle Ca²⁺ release channel. *J. Biol. Chem.* **278**, 8348-8355

198. Menegazzi, P., Larini, F., Treves, S., Guerrini, R., Quadroni, M., and Zorzato, F. (1994) Identification and characterization of three calmodulin binding sites of the skeletal muscle ryanodine receptor. *Biochemistry* **33**, 9078-9084
199. Zorzato, F., Fujii, J., Otsu, K., Phillips, M., Green, N. M., Lai, F. A., Meissner, G., and MacLennan, D. H. (1990) Molecular cloning of cDNA encoding human and rabbit forms of the Ca²⁺ release channel (ryanodine receptor) of skeletal muscle sarcoplasmic reticulum. *J. Biol. Chem.* **265**, 2244-2256
200. Chen, S. R., and MacLennan, D. H. (1994) Identification of calmodulin-, Ca(2+)-, and ruthenium red-binding domains in the Ca²⁺ release channel (ryanodine receptor) of rabbit skeletal muscle sarcoplasmic reticulum. *J. Biol. Chem.* **269**, 22698-22704
201. Most, P., Remppis, A., Weber, C., Bernotat, J., Ehlermann, P., Pleger, S. T., Kirsch, W., Weber, M., Uttenweiler, D., Smith, G. L., Katus, H. A., and Fink, R. H. A. (2003) The C terminus (amino acids 75-94) and the linker region (amino acids 42-54) of the Ca²⁺-binding protein S100A1 differentially enhance sarcoplasmic Ca²⁺ release in murine skinned skeletal muscle fibers. *J. Biol. Chem.* **278**, 26356-26364
202. Treves, S., Scutari, E., Robert, M., Groh, S., Ottolia, M., Prestipino, G., Ronjat, M., and Zorzato, F. (1997) Interaction of S100A1 with the Ca²⁺ release channel (ryanodine receptor) of skeletal muscle. *Biochemistry* **36**, 11496-11503
203. Prosser, B. L., Wright, N. T., Hernández-Ochoa, E. O., Varney, K. M., Liu, Y., Olojo, R. O., Zimmer, D. B., Weber, D. J., and Schneider, M. F. (2008) S100A1 binds to the calmodulin-binding site of ryanodine receptor and modulates skeletal muscle excitation-contraction coupling. *J. Biol. Chem.* **283**, 5046-5057

204. Du, X.-J., Cole, T. J., Tennis, N., Gao, X.-M., Köntgen, F., Kemp, B. E., and Heierhorst, J. (2002) Impaired cardiac contractility response to hemodynamic stress in S100A1-deficient mice. *Mol. Cell. Biol.* **22**, 2821-2829
205. Amador, F. J., Liu, S., Ishiyama, N., Plevin, M. J., Wilson, A., MacLennan, D. H., and Ikura, M. (2009) Crystal structure of type I ryanodine receptor amino-terminal beta-trefoil domain reveals a disease-associated mutation "hot spot" loop. *Proc. Natl. Acad. Sci. U.S.A.* **106**, 11040-11044
206. Lobo, P. A., and Van Petegem, F. (2009) Crystal structures of the N-terminal domains of cardiac and skeletal muscle ryanodine receptors: insights into disease mutations. *Structure* **17**, 1505-1514
207. Amador, F. J., Kimlicka, L., Stathopoulos, P. B., Gasmi-Seabrook, G. M. C., MacLennan, D. H., Van Petegem, F., and Ikura, M. (2013) Type 2 ryanodine receptor domain A contains a unique and dynamic α -helix that transitions to a β -strand in a mutant linked with a heritable cardiomyopathy. *J. Mol. Biol.* **425**, 4034-4046
208. Tung, C.-C., Lobo, P. A., Kimlicka, L., and Van Petegem, F. (2010) The amino-terminal disease hotspot of ryanodine receptors forms a cytoplasmic vestibule. *Nature* **468**, 585-588
209. Kimlicka, L., Lau, K., Tung, C.-C., and Van Petegem, F. (2013) Disease mutations in the ryanodine receptor N-terminal region couple to a mobile intersubunit interface. *Nat. Commun.* **4**, 1506
210. Kimlicka, L., Tung, C.-C., Carlsson, A.-C. C., Lobo, P. A., Yuchi, Z., and Van Petegem, F. (2013) The cardiac ryanodine receptor N-terminal region contains an anion binding site that is targeted by disease mutations. *Structure* **21**, 1440-1449

211. Lobo, P. A., Kimlicka, L., Tung, C.-C., and Van Petegem, F. (2011) The deletion of exon 3 in the cardiac ryanodine receptor is rescued by β strand switching. *Structure* **19**, 790-798
212. Wehrens, X. H. T., Lehnart, S. E., Reiken, S. R., and Marks, A. R. (2004) Ca^{2+} /calmodulin-dependent protein kinase II phosphorylation regulates the cardiac ryanodine receptor. *Circ. Res.* **94**, e61-70
213. Jiang, M. T., Lokuta, A. J., Farrell, E. F., Wolff, M. R., Haworth, R. A., and Valdivia, H. H. (2002) Abnormal Ca^{2+} release, but normal ryanodine receptors, in canine and human heart failure. *Circ. Res.* **91**, 1015-1022
214. Zhang, H., Makarewich, C. A., Kubo, H., Wang, W., Duran, J. M., Li, Y., Berretta, R. M., Koch, W. J., Chen, X., Gao, E., Valdivia, H. H., and Houser, S. R. (2012) Hyperphosphorylation of the cardiac ryanodine receptor at serine 2808 is not involved in cardiac dysfunction after myocardial infarction. *Circ. Res.* **110**, 831-840
215. Sharma, P., Ishiyama, N., Nair, U., Li, W., Dong, A., Miyake, T., Wilson, A., Ryan, T., MacLennan, D. H., Kislinger, T., Ikura, M., Dhe-Paganon, S., and Gramolini, A. O. (2012) Structural determination of the phosphorylation domain of the ryanodine receptor. *FEBS J.* **279**, 3952-3964
216. Yuchi, Z., Lau, K., and Van Petegem, F. (2012) Disease mutations in the ryanodine receptor central region: crystal structures of a phosphorylation hot spot domain. *Structure* **20**, 1201-1211
217. Wriggers, W. and Chacón, P. (2001) Modeling tricks and fitting techniques for multiresolution structures. *Structure* **9**, 779-788

218. Wriggers, W., and Birmanns, S. (2001) Using situs for flexible and rigid-body fitting of multiresolution single-molecule data. *J. Struct. Biol.* **133**, 193-202
219. Baker, M. L., Serysheva, I. I., Sencer, S., Wu, Y., Ludtke, S. J., Jiang, W., Hamilton, S. L., and Chiu, W. (2002) The skeletal muscle Ca²⁺ release channel has an oxidoreductase-like domain. *Proc. Natl. Acad. Sci. U.S.A.* **99**, 12155-12160
220. Zhu, L., Zhong, X., Chen, S. R. W., Banavali, N., and Liu, Z. (2013) Modeling a ryanodine receptor N-terminal domain connecting the central vestibule and the corner clamp region. *J. Biol. Chem.* **288**, 903-914
221. Yin, C.-C., Blayney, L. M., and Lai, F. A. (2005) Physical coupling between ryanodine receptor-calcium release channels. *Journal of Molecular Biology* **349**, 538-546
222. Yin, C.-C., D'Cruz, L. G., and Lai, F. A. (2008) Ryanodine receptor arrays: not just a pretty pattern? *Trends Cell Biol.* **18**, 149-156
223. Wolfram, F., Morris, E., and Taylor, C. W. (2010) Three-dimensional structure of recombinant type 1 inositol 1,4,5-trisphosphate receptor. *Biochem. J.* **428**, 483-489
224. Sato, C., Hamada, K., Ogura, T., Miyazawa, A., Iwasaki, K., Hiroaki, Y., Tani, K., Terauchi, A., Fujiyoshi, Y., and Mikoshiba, K. (2004) Inositol 1,4,5-trisphosphate receptor contains multiple cavities and L-shaped ligand-binding domains. *J. Mol. Biol.* **336**, 155-164
225. Serysheva, I. I., Bare, D. J., Ludtke, S. J., Kettlun, C. S., Chiu, W., and Mignery, G. A. (2003) Structure of the type 1 inositol 1,4,5-trisphosphate receptor revealed by electron cryomicroscopy. *J. Biol. Chem.* **278**, 21319-21322

226. da Fonseca, P. C. A., Morris, S. A., Nerou, E. P., Taylor, C. W., and Morris, E. P. (2003) Domain organization of the type 1 inositol 1,4,5-trisphosphate receptor as revealed by single-particle analysis. *Proc. Natl. Acad. Sci. U.S.A.* **100**, 3936-3941
227. Hamada, K., Terauchi, A., and Mikoshiba, K. (2003) Three-dimensional rearrangements within inositol 1,4,5-trisphosphate receptor by calcium. *J. Biol. Chem.* **278**, 52881-52889
228. Jiang, Q.-X., Thrower, E. C., Chester, D. W., Ehrlich, B. E., and Sigworth, F. J. (2002) Three-dimensional structure of the type 1 inositol 1,4,5-trisphosphate receptor at 24 Å resolution. *EMBO J.* **21**, 3575-3581
229. Ludtke, S. J., Tran, T. P., Ngo, Q. T., Moiseenkova-Bell, V. Y., Chiu, W., and Serysheva, I. I. (2011) Flexible architecture of IP₃R1 by Cryo-EM. *Structure* **19**, 1192-1199
230. Murray, S. C., Flanagan, J., Popova, O. B., Chiu, W., Ludtke, S. J., and Serysheva, I. I. (2013) Validation of cryo-EM structure of IP₃R1 channel. *Structure* **21**, 900-909
231. Bosanac, I., Yamazaki, H., Matsu-Ura, T., Michikawa, T., Mikoshiba, K., and Ikura, M. (2005) Crystal structure of the ligand binding suppressor domain of type 1 inositol 1,4,5-trisphosphate receptor. *Mol. Cell* **17**, 193-203
232. Chan, J., Yamazaki, H., Ishiyama, N., Seo, M.-D., Mal, T. K., Michikawa, T., Mikoshiba, K., and Ikura, M. (2010) Structural studies of inositol 1,4,5-trisphosphate receptor: coupling ligand binding to channel gating. *J. Biol. Chem.* **285**, 36092-36099
233. Bosanac, I., Alattia, J.-R., Mal, T. K., Chan, J., Talarico, S., Tong, F. K., Tong, K. I., Yoshikawa, F., Furuichi, T., Iwai, M., Michikawa, T., Mikoshiba, K., and Ikura, M. (2002) Structure of the inositol 1,4,5-trisphosphate receptor binding core in complex with its ligand. *Nature* **420**, 696-700

234. Seo, M.-D., Velamakanni, S., Ishiyama, N., Stathopoulos, P. B., Rossi, A. M., Khan, S. A., Dale, P., Li, C., Ames, J. B., Ikura, M., and Taylor, C. W. (2012) Structural and functional conservation of key domains in InsP₃ and ryanodine receptors. *Nature* **483**, 108-112
235. Lin, C.-C., Baek, K., and Lu, Z. (2011) Apo and InsP₃-bound crystal structures of the ligand-binding domain of an InsP₃ receptor. *Nat. Struct. Mol. Biol.* **18**, 1172-1174
236. Yuchi, Z., and Van Petegem, F. (2011) Common allosteric mechanisms between ryanodine and inositol-1,4,5-trisphosphate receptors. *Channels (Austin)* **5**, 120-123
237. Endo, M., Tanaka, M., and Ogawa, Y. (1970) Calcium induced release of calcium from the sarcoplasmic reticulum of skinned skeletal muscle fibres. *Nature* **228**, 34-36
238. Kimlicka, L., and Van Petegem, F. (2011) The structural biology of ryanodine receptors. *Sci. China Life Sci.* **54**, 712-724
239. Zhong, X., Liu, Y., Zhu, L., Meng, X., Wang, R., Van Petegem, F., Wagenknecht, T., Chen, S. R. W., and Liu, Z. (2013) Conformational Dynamics inside Amino-Terminal Disease Hotspot of Ryanodine Receptor. *Structure* **21**, 2051-2060
240. Birmanns, S., Rusu, M., and Wriggers, W. (2011) Using Sculptor and Situs for simultaneous assembly of atomic components into low-resolution shapes. *J. Struct. Biol.* **173**, 428-435
241. Kabsch, W. (2010) XDS. *Acta Crystallogr. D Biol. Crystallogr.* **66**, 125-132
242. McCoy, A. J., Grosse-Kunstleve, R. W., Adams, P. D., Winn, M. D., Storoni, L. C., and Read, R. J. (2007) Phaser crystallographic software. *J. Appl. Crystallogr.* **40**, 658-674
243. Emsley, P., and Cowtan, K. (2004) Coot: model-building tools for molecular graphics. *Acta Crystallogr. D Biol. Crystallogr.* **60**, 2126-2132

244. Murshudov, G. N., Vagin, A. A., and Dodson, E. J. (1997) Refinement of macromolecular structures by the maximum-likelihood method. *Acta Crystallogr. D Biol. Crystallogr.* **53**, 240-255
245. Nettleship, J. E., Brown, J., Groves, M. R., and Geerlof, A. (2008) Methods for protein characterization by mass spectrometry, thermal shift (ThermoFluor) assay, and multiangle or static light scattering. *Methods Mol. Biol.* **426**, 299-318
246. Pettersen, E. F., Goddard, T. D., Huang, C. C., Couch, G. S., Greenblatt, D. M., Meng, E. C., and Ferrin, T. E. (2004) UCSF Chimera--a visualization system for exploratory research and analysis. *J. Comput. Chem.* **25**, 1605-1612
247. Capacchione, J. F., and Muldoon, S. M. (2009) The relationship between exertional heat illness, exertional rhabdomyolysis, and malignant hyperthermia. *Anesth. Analg.* **109**, 1065-1069
248. Durham, W. J., Aracena-Parks, P., Long, C., Rossi, A. E., Goonasekera, S. A., Boncompagni, S., Galvan, D. L., Gilman, C. P., Baker, M. R., Shirokova, N., Protasi, F., Dirksen, R., and Hamilton, S. L. (2008) RyR1 S-nitrosylation underlies environmental heat stroke and sudden death in Y522S RyR1 knockin mice. *Cell* **133**, 53-65
249. Muldoon, S., Deuster, P., Brandom, B., and Bungler, R. (2004) Is there a link between malignant hyperthermia and exertional heat illness? *Exerc. Sport Sci. Rev.* **32**, 174-179
250. Tobin, J. R., Jason, D. R., Challa, V. R., Nelson, T. E., and Sambuughin, N. (2001) Malignant hyperthermia and apparent heat stroke. *JAMA* **286**, 168-169
251. Nishio, H., Sato, T., Fukunishi, S., Tamura, A., Iwata, M., Tsuboi, K., and Suzuki, K. (2009) Identification of malignant hyperthermia-susceptible ryanodine receptor type 1

- gene (RYR1) mutations in a child who died in a car after exposure to a high environmental temperature. *Leg. Med. (Tokyo)* **11**, 142-143
252. Bourdon, L., and Canini, F. (1995) On the nature of the link between malignant hyperthermia and exertional heatstroke. *Med. Hypotheses* **45**, 268-270
253. Bendahan, D., Kozak-Ribbens, G., Confort-Gouny, S., Ghattas, B., Figarella-Branger, D., Aubert, M., and Cozzone, P. J. (2001) A noninvasive investigation of muscle energetics supports similarities between exertional heat stroke and malignant hyperthermia. *Anesth. Analg.* **93**, 683-689
254. Davis, M., Brown, R., Dickson, A., Horton, H., James, D., Laing, N., Marston, R., Norgate, M., Perlman, D., and Pollock, N. (2002) Malignant hyperthermia associated with exercise-induced rhabdomyolysis or congenital abnormalities and a novel RYR1 mutation in New Zealand and Australian pedigrees. *Br. J. Anaesth.* **88**, 508-515
255. Ibarra M, C. A., Wu, S., Murayama, K., Minami, N., Ichihara, Y., Kikuchi, H., Noguchi, S., Hayashi, Y. K., Ochiai, R., and Nishino, I. (2006) Malignant hyperthermia in Japan: mutation screening of the entire ryanodine receptor type 1 gene coding region by direct sequencing. *Anesthesiology* **104**, 1146-1154
256. Lynch, P. J., Krivosic-Horber, R., Reyford, H., Monnier, N., Quane, K., Adnet, P., Haudecoeur, G., Krivosic, I., McCarthy, T., and Lunardi, J. (1997) Identification of heterozygous and homozygous individuals with the novel RYR1 mutation Cys35Arg in a large kindred. *Anesthesiology* **86**, 620-626
257. Tammaro, A., Bracco, A., Cozzolino, S., Esposito, M., Di Martino, A., Savoia, G., Zeuli, L., Piluso, G., Aurino, S., and Nigro, V. (2003) Scanning for mutations of the ryanodine

- receptor (RYR1) gene by denaturing HPLC: detection of three novel malignant hyperthermia alleles. *Clin. Chem.* **49**, 761-768
258. Sato, K., Roesl, C., Pollock, N., and Stowell, K. M. (2013) Skeletal muscle ryanodine receptor mutations associated with malignant hyperthermia showed enhanced intensity and sensitivity to triggering drugs when expressed in human embryonic kidney cells. *Anesthesiology* **119**, 111-118
259. Wu, S., Ibarra M, C. A., Malicdan, M. C. V., Murayama, K., Ichihara, Y., Kikuchi, H., Nonaka, I., Noguchi, S., Hayashi, Y. K., and Nishino, I. (2006) Central core disease is due to RYR1 mutations in more than 90% of patients. *Brain* **129**, 1470-1480
260. Romero, N. B., Monnier, N., Viollet, L., Cortey, A., Chevallay, M., Leroy, J.-P., Lunardi, J., and Fardeau, M. (2003) Dominant and recessive central core disease associated with RYR1 mutations and fetal akinesia. *Brain* **126**, 2341-2349
261. Zhou, H., Treves, S., Jungbluth, H., Sewry, C., and Muntoni, F. (2005) RYR1 gene genotype-phenotype and functional correlative studies in central core disease and multi-minicore disease. *Neuromusc. Dis.* **15**, 676-743
262. Gillard, E. F., Otsu, K., Fujii, J., Duff, C., de Leon, S., Khanna, V. K., Britt, B. A., Worton, R. G., and MacLennan, D. H. (1992) Polymorphisms and deduced amino acid substitutions in the coding sequence of the ryanodine receptor (RYR1) gene in individuals with malignant hyperthermia. *Genomics* **13**, 1247-1254
263. Quane, K. A., Healy, J. M., Keating, K. E., Manning, B. M., Couch, F. J., Palmucci, L. M., Doriguzzi, C., Fagerlund, T. H., Berg, K., and Ording, H. (1993) Mutations in the ryanodine receptor gene in central core disease and malignant hyperthermia. *Nat. Genet.* **5**, 51-55

264. Wehrens, X. H. T., Lehnart, S. E., Huang, F., Vest, J. A., Reiken, S. R., Mohler, P. J., Sun, J., Guatimosim, S., Song, L.-S., Rosemlit, N., D'Armiento, J. M., Napolitano, C., Memmi, M., Priori, S. G., Lederer, W. J., and Marks, A. R. (2003) FKBP12.6 deficiency and defective calcium release channel (ryanodine receptor) function linked to exercise-induced sudden cardiac death. *Cell* **113**, 829-840
265. Lehnart, S. E., Mongillo, M., Bellinger, A., Lindegger, N., Chen, B.-X., Hsueh, W., Reiken, S., Wronska, A., Drew, L. J., and Ward, C. W. (2008) Leaky Ca²⁺ release channel/ryanodine receptor 2 causes seizures and sudden cardiac death in mice. *The J. Clin. Invest.* **118**, 2230
266. Meli, A. C., Refaat, M. M., Dura, M., Reiken, S., Wronska, A., Wojciak, J., Carroll, J., Scheinman, M. M., and Marks, A. R. (2011) A novel ryanodine receptor mutation linked to sudden death increases sensitivity to cytosolic calcium. *Circ. Res.* **109**, 281-290
267. Lin, T. Y., and Kim, P. S. (1991) Evaluating the effects of a single amino acid substitution on both the native and denatured states of a protein. *Proc. Natl. Acad. Sci. U.S.A.* **88**, 10573-10577
268. Stewart, R., Zissimopoulos, S., and Lai, F. A. (2003) Oligomerization of the cardiac ryanodine receptor C-terminal tail. *Biochem. J.* **376**, 795-799
269. Valdivia, H. H., Hogan, K., and Coronado, R. (1991) Altered binding site for Ca²⁺ in the ryanodine receptor of human malignant hyperthermia. *Am. J. Physiol.* **261**, C237-245
270. Dietze, B., Henke, J., Eichinger, H. M., Lehmann-Horn, F., and Melzer, W. (2000) Malignant hyperthermia mutation Arg615Cys in the porcine ryanodine receptor alters voltage dependence of Ca²⁺ release. *J. Physiol.* **526(Pt 3)**, 507-514

271. Van Petegem, F., Clark, K. A., Chatelain, F. C., and Minor, D. L. (2004) Structure of a complex between a voltage-gated calcium channel beta-subunit and an alpha-subunit domain. *Nature* **429**, 671-675
272. Emsley, P., Lohkamp, B., Scott, W. G., and Cowtan, K. (2010) Features and development of Coot. *Acta Crystallogr. D Biol. Crystallogr.* **66**, 486-501
273. Adams, P. D., Afonine, P. V., Bunkóczi, G., Chen, V. B., Davis, I. W., Echols, N., Headd, J. J., Hung, L.-W., Kapral, G. J., Grosse-Kunstleve, R. W., McCoy, A. J., Moriarty, N. W., Oeffner, R., Read, R. J., Richardson, D. C., Richardson, J. S., Terwilliger, T. C., and Zwart, P. H. (2010) PHENIX: a comprehensive Python-based system for macromolecular structure solution. *Acta Crystallogr. D Biol. Crystallogr.* **66**, 213-221
274. MacLennan, D. H., and Phillips, M. S. (1992) Malignant hyperthermia. *Science* **256**, 789-794
275. Zhang, Y., Chen, H. S., Khanna, V. K., de Leon, S., Phillips, M. S., Schappert, K., Britt, B. A., Browell, A. K., and MacLennan, D. H. (1993) A mutation in the human ryanodine receptor gene associated with central core disease. *Nat. Genet.* **5**, 46-50
276. Langer, G., Cohen, S. X., Lamzin, V. S., and Perrakis, A. (2008) Automated macromolecular model building for X-ray crystallography using ARP/wARP version 7. *Nat. Protoc.* **3**, 1171-1179
277. Medeiros-Domingo, A., Bhuiyan, Z. A., Tester, D. J., Hofman, N., Bikker, H., van Tintelen, J. P., Mannens, M. M. A. M., Wilde, A. A. M., and Ackerman, M. J. (2009) The RYR2-encoded ryanodine receptor/calcium release channel in patients diagnosed previously with either catecholaminergic polymorphic ventricular tachycardia or

- genotype negative, exercise-induced long QT syndrome: a comprehensive open reading frame mutational analysis. *J. Am. Coll. Cardiol.* **54**, 2065-2074
278. Bhuiyan, Z. A., van den Berg, M. P., van Tintelen, J. P., Bink-Boelkens, M. T. E., Wiesfeld, A. C. P., Alders, M., Postma, A. V., van Langen, I., Mannens, M. M. A. M., and Wilde, A. A. M. (2007) Expanding spectrum of human RYR2-related disease: new electrocardiographic, structural, and genetic features. *Circulation* **116**, 1569-1576
279. Marjamaa, A., Laitinen-Forsblom, P., Lahtinen, A. M., Viitasalo, M., Toivonen, L., Kontula, K., and Swan, H. (2009) Search for cardiac calcium cycling gene mutations in familial ventricular arrhythmias resembling catecholaminergic polymorphic ventricular tachycardia. *BMC Med. Genet.* **10**, 12
280. Tiso, N., Stephan, D. A., Nava, A., Bagattin, A., Devaney, J. M., Stanchi, F., Larderet, G., Brahmbhatt, B., Brown, K., Bauce, B., Muriago, M., Basso, C., Thiene, G., Danieli, G. A., and Rampazzo, A. (2001) Identification of mutations in the cardiac ryanodine receptor gene in families affected with arrhythmogenic right ventricular cardiomyopathy type 2 (ARVD2). *Hum. Mol. Genet.* **10**, 189-194
281. Liu, Y., Kimlicka, L., Hiess, F., Tian, X., Wang, R., Zhang, L., Jones, P. P., Van Petegem, F., and Chen, S. R. W. (2013) The CPVT-associated RyR2 mutation G230C enhances store overload-induced Ca²⁺ release and destabilizes the N-terminal domains. *Biochem. J.* **454**, 123-131
282. Tester, D. J., Kopplin, L. J., Creighton, W., Burke, A. P., and Ackerman, M. J. (2005) Pathogenesis of unexplained drowning: new insights from a molecular autopsy. *Mayo Clin. Proc.* **80**, 596-600

283. Creighton, W., Virmani, R., Kutys, R., and Burke, A. (2006) Identification of novel missense mutations of cardiac ryanodine receptor gene in exercise-induced sudden death at autopsy. *J. Mol. Diagn.* **8**, 62-67
284. Choi, G., Kopplin, L. J., Tester, D. J., Will, M. L., Haglund, C. M., and Ackerman, M. J. (2004) Spectrum and frequency of cardiac channel defects in swimming-triggered arrhythmia syndromes. *Circulation* **110**, 2119-2124
285. Galli, L., Orrico, A., Lorenzini, S., Censini, S., Falciani, M., Covacci, A., Tegazzin, V., and Sorrentino, V. (2006) Frequency and localization of mutations in the 106 exons of the RYR1 gene in 50 individuals with malignant hyperthermia. *Hum. Mutat.* **27**, 830
286. Levano, S., Vukcevic, M., Singer, M., Matter, A., Treves, S., Urwyler, A., and Girard, T. (2009) Increasing the number of diagnostic mutations in malignant hyperthermia. *Hum. Mutat.* **30**, 590-598
287. Karshikoff, A., and Ladenstein, R. (2001) Ion pairs and the thermotolerance of proteins from hyperthermophiles: a "traffic rule" for hot roads. *Trends Biochem. Sci.* **26**, 550-556
288. Fruen, B. R., Mickelson, J. R., Roghair, T. J., Cheng, H. L., and Louis, C. F. (1994) Anions that potentiate excitation-contraction coupling may mimic effect of phosphate on Ca²⁺ release channel. *Am. J. Physiol.* **266**, C1729-1735
289. Fruen, B. R., Kane, P. K., Mickelson, J. R., and Louis, C. F. (1996) Chloride-dependent sarcoplasmic reticulum Ca²⁺ release correlates with increased Ca²⁺ activation of ryanodine receptors. *Biophys. J.* **71**, 2522-2530
290. Liu, W., Pasek, D. A., and Meissner, G. (1998) Modulation of Ca²⁺-gated cardiac muscle Ca²⁺-release channel (ryanodine receptor) by mono- and divalent ions. *Am. J. Physiol., Cell Physiol.* **274**, C120-C128

291. Niggli, E., Ullrich, N. D., Gutierrez, D., Kyrychenko, S., Poláková, E., and Shirokova, N. (2013) Posttranslational modifications of cardiac ryanodine receptors: Ca(2+) signaling and EC-coupling. *Biochim. Biophys. Acta* **1833**, 866-875
292. Oda, T., Yano, M., Yamamoto, T., Tokuhisa, T., Okuda, S., Doi, M., Ohkusa, T., Ikeda, Y., Kobayashi, S., Ikemoto, N., and Matsuzaki, M. (2005) Defective regulation of interdomain interactions within the ryanodine receptor plays a key role in the pathogenesis of heart failure. *Circulation* **111**, 3400-3410
293. Liu, Z., Wang, R., Tian, X., Zhong, X., Gangopadhyay, J., Cole, R., Ikemoto, N., Chen, S. R. W., and Wagenknecht, T. (2010) Dynamic, inter-subunit interactions between the N-terminal and central mutation regions of cardiac ryanodine receptor. *J. Cell. Sci.* **123**, 1775-1784
294. Hironaka, T., and Morimoto, S. (1980) Intracellular chloride concentration and evidence for the existence of a chloride pump in frog skeletal muscle. *Jpn. J. Physiol.* **30**, 357-363
295. Payne, J. A., Rivera, C., Voipio, J., and Kaila, K. (2003) Cation-chloride co-transporters in neuronal communication, development and trauma. *Trends Neurosci.* **26**, 199-206
296. Treharne, K. J., Crawford, R. M., and Mehta, A. (2006) CFTR, chloride concentration and cell volume: could mammalian protein histidine phosphorylation play a latent role? *Exp. Physiol.* **91**, 131-139
297. Desilets, M., Puceat, M., and Vassort, G. (1994) Chloride dependence of pH modulation by beta-adrenergic agonist in rat cardiomyocytes. *Circ. Res.* **75**, 862-869
298. Bannister, R. A., Esteve, E., Eltit, J. M., Pessah, I. N., Allen, P. D., Lopez, J. R., and Beam, K. G. (2010) A malignant hyperthermia-inducing mutation in RYR1 (R163C):

- consequent alterations in the functional properties of DHPR channels. *J. Gen. Physiol.* **135**, 629-640
299. Esteve, E., Eltit, J. M., Bannister, R. A., Liu, K., Pessah, I. N., Beam, K. G., Allen, P. D., and Lopez, J. R. (2010) A malignant hyperthermia-inducing mutation in RYR1 (R163C): alterations in Ca²⁺ entry, release, and retrograde signaling to the DHPR. *J. Gen. Physiol.* **135**, 619-628
300. Loke, J. C. P., Kraev, N., Sharma, P., Du, G., Patel, L., Kraev, A., and MacLennan, D. H. (2003) Detection of a novel ryanodine receptor subtype 1 mutation (R328W) in a malignant hyperthermia family by sequencing of a leukocyte transcript. *Anesthesiology* **99**, 297-302
301. Vukcevic, M., Broman, M., Islander, G., Bodelsson, M., Ranklev-Twetman, E., Müller, C. R., and Treves, S. (2010) Functional properties of RYR1 mutations identified in Swedish patients with malignant hyperthermia and central core disease. *Anesth. Analg.* **111**, 185-190
302. Andronache, Z., Hamilton, S. L., Dirksen, R. T., and Melzer, W. (2009) A retrograde signal from RyR1 alters DHP receptor inactivation and limits window Ca²⁺ release in muscle fibers of Y522S RyR1 knock-in mice. *Proc. Natl. Acad. Sci. U.S.A.* **106**, 4531-4536
303. Boncompagni, S., Rossi, A. E., Micaroni, M., Hamilton, S. L., Dirksen, R. T., Franzini-Armstrong, C., and Protasi, F. (2009) Characterization and temporal development of cores in a mouse model of malignant hyperthermia. *Proc. Natl. Acad. Sci. U.S.A.* **106**, 21996-22001

304. Zullo, A., Klingler, W., De Sarno, C., Ferrara, M., Fortunato, G., Perrotta, G., Gravino, E., Di Noto, R., Lehmann-Horn, F., Melzer, W., Salvatore, F., and Carsana, A. (2009) Functional characterization of ryanodine receptor (RYR1) sequence variants using a metabolic assay in immortalized B-lymphocytes. *Hum. Mutat.* **30**, E575-590
305. Dirksen, R. T., and Avila, G. (2004) Distinct effects on Ca²⁺ handling caused by malignant hyperthermia and central core disease mutations in RyR1. *Biophys. J.* **87**, 3193-3204
306. Richter, M., Schleithoff, L., Deufel, T., Lehmann-Horn, F., and Herrmann-Frank, A. (1997) Functional characterization of a distinct ryanodine receptor mutation in human malignant hyperthermia-susceptible muscle. *J. Biol. Chem.* **272**, 5256-5260
307. Migita, T., Mukaida, K., Hamada, H., Yasuda, T., Haraki, T., Nishino, I., Murakami, N., and Kawamoto, M. (2009) Functional analysis of ryanodine receptor type 1 p.R2508C mutation in exon 47. *J. Anesth.* **23**, 341-346
308. Lyfenko, A. D., Ducreux, S., Wang, Y., Xu, L., Zorzato, F., Ferreiro, A., Meissner, G., Treves, S., and Dirksen, R. T. (2007) Two central core disease (CCD) deletions in the C-terminal region of RYR1 alter muscle excitation-contraction (EC) coupling by distinct mechanisms. *Hum. Mutat.* **28**, 61-68
309. Yuen, B., Boncompagni, S., Feng, W., Yang, T., Lopez, J. R., Matthaei, K. I., Goth, S. R., Protasi, F., Franzini-Armstrong, C., Allen, P. D., and Pessah, I. N. (2012) Mice expressing T4826I-RYR1 are viable but exhibit sex- and genotype-dependent susceptibility to malignant hyperthermia and muscle damage. *FASEB J.* **26**, 1311-1322

310. Anderson, A. A., Brown, R. L., Polster, B., Pollock, N., and Stowell, K. M. (2008) Identification and biochemical characterization of a novel ryanodine receptor gene mutation associated with malignant hyperthermia. *Anesthesiology* **108**, 208-215
311. Thomas, N. L., George, C. H., and Lai, F. A. (2004) Functional heterogeneity of ryanodine receptor mutations associated with sudden cardiac death. *Cardiovas. Res.* **64**, 52-60
312. van Oort, R. J., Respress, J. L., Li, N., Reynolds, C., De Almeida, A. C., Skapura, D. G., De Windt, L. J., and Wehrens, X. H. T. (2010) Accelerated development of pressure overload-induced cardiac hypertrophy and dysfunction in an RyR2-R176Q knockin mouse model. *Hypertension* **55**, 932-938
313. Mathur, N., Sood, S., Wang, S., van Oort, R. J., Sarma, S., Li, N., Skapura, D. G., Bayle, J. H., Valderrábano, M., and Wehrens, X. H. T. (2009) Sudden infant death syndrome in mice with an inherited mutation in RyR2. *Circ. Arrhythm. Electrophysiol.* **2**, 677-685
314. Thomas, N. L., Lai, F. A., and George, C. H. (2005) Differential Ca²⁺ sensitivity of RyR2 mutations reveals distinct mechanisms of channel dysfunction in sudden cardiac death. *Biochem. Biophys. Res. Commun.* **331**, 231-238
315. Jiang, D., Jones, P. P., Davis, D., Gow, R., Green, M., Birnie, D., Chen, S. R. W., and Gollob, M. H. (2010) Characterization of a novel mutation in the cardiac ryanodine receptor that results in catecholaminergic polymorphic ventricular tachycardia. *Channels* **4**, 302-310
316. Suetomi, T., Yano, M., Uchinoumi, H., Fukuda, M., Hino, A., Ono, M., Xu, X., Tateishi, H., Okuda, S., Doi, M., Kobayashi, S., Ikeda, Y., Yamamoto, T., Ikemoto, N., and Matsuzaki, M. (2011) Mutation-linked defective interdomain interactions within

- ryanodine receptor cause aberrant Ca²⁺release leading to catecholaminergic polymorphic ventricular tachycardia. *Circulation* **124**, 682-694
317. Tester, D. J., Dura, M., Carturan, E., Reiken, S., Wronska, A., Marks, A. R., and Ackerman, M. J. (2007) A mechanism for sudden infant death syndrome (SIDS): stress-induced leak via ryanodine receptors. *Heart Rhythm* **4**, 733-739
318. Goddard, C. A., Ghais, N. S., Zhang, Y., Williams, A. J., Colledge, W. H., Grace, A. A., and Huang, C. L. H. (2008) Physiological consequences of the P2328S mutation in the ryanodine receptor (RyR2) gene in genetically modified murine hearts. *Acta Physiol. (Oxf.)* **194**, 123-140
319. Lehnart, S. E., Wehrens, X. H. T., Laitinen, P. J., Reiken, S. R., Deng, S.-X., Cheng, Z., Landry, D. W., Kontula, K., Swan, H., and Marks, A. R. (2004) Sudden death in familial polymorphic ventricular tachycardia associated with calcium release channel (ryanodine receptor) leak. *Circulation* **109**, 3208-3214
320. Kobayashi, S., Yano, M., Uchinoumi, H., Suetomi, T., Susa, T., Ono, M., Xu, X., Tateishi, H., Oda, T., and Okuda, S. (2010) Dantrolene, a therapeutic agent for malignant hyperthermia, inhibits catecholaminergic polymorphic ventricular tachycardia in a RyR2 (R2474S/+) knock-in mouse model. *Circ. J.* **74**, 2579-2584
321. Cerrone, M., Noujaim, S. F., Tolkacheva, E. G., Talkachou, A., O'Connell, R., Berenfeld, O., Anumonwo, J., Pandit, S. V., Vikstrom, K., Napolitano, C., Priori, S. G., and Jalife, J. (2007) Arrhythmogenic mechanisms in a mouse model of catecholaminergic polymorphic ventricular tachycardia. *Circ. Res.* **101**, 1039-1048
322. Fernández-Velasco, M., Rueda, A., Rizzi, N., Benitah, J.-P., Colombi, B., Napolitano, C., Priori, S. G., Richard, S., and Gómez, A. M. (2009) Increased Ca²⁺ sensitivity of the

- ryanodine receptor mutant RyR2R4496C underlies catecholaminergic polymorphic ventricular tachycardia. *Circ. Res.* **104**, 201-209
323. Kashimura, T., Briston, S. J., Trafford, A. W., Napolitano, C., Priori, S. G., Eisner, D. A., and Venetucci, L. A. (2010) In the RyR2(R4496C) mouse model of CPVT, β -adrenergic stimulation induces Ca waves by increasing SR Ca content and not by decreasing the threshold for Ca waves. *Circ. Res.* **107**, 1483-1489
324. Du, G. G., Guo, X., Khanna, V. K., and MacLennan, D. H. (2001) Functional characterization of mutants in the predicted pore region of the rabbit cardiac muscle Ca(2+) release channel (ryanodine receptor isoform 2). *J. Biol. Chem.* **276**, 31760-31771

Appendices

Appendix A

Table A.1: Summary from functional studies on RyR disease-associated mutations. Mutations that alter RyR functions are listed as gain or loss of function. Mutations with no discernible change compared with wild-type channels are listed as “uncertain.” References to the functional studies are listed beside the corresponding mutations. Amino residue numbering is for human RyRs. (Δ) = deletion mutation. (/) = double mutation. (MH) = Malignant hyperthermia, (CCD) = central core disease, ((MmD) = multi-minicore disease, (CNMDU1) = congenital neuromuscular disease with uniform type 1 fiber, (CPVT) = catecholaminergic polymorphic ventricular tachycardia, (ARVD2) = arrhythmogenic right ventricular dysplasia type 2, and (IVF) = idiopathic ventricular fibrillation.

Effect	Isoform	Mutation	Disease	References
Gain of function	RyR1	C35R	MH	(71,74)
		R44C	MH	(258)
		R163C	MH/CCD/MmD	(58,60,68,69,71,74,97,258,298,299)
		G248R	MH	(71,74,97)
		R328W	MH	(300)
		G341R	MH	(69,71,74)
		H382H	MH	(301)
		R401C	MH	(258)
		I403M	MH/CCD	(71,74)
		Y522S	MH/CCD	(57,68,70,71,74,94,248,302,303)
		R530H	MH	(304)
		R533C	MH	(258)
		R533H	MH	(258)
		R552W	MH	(71,74)
		A612P	MH	(56)

Effect	Isoform	Mutation	Disease	References
Gain of function	RyR1	R614C	MH	(51,52,69,71,74,77,78,84,85,88,89,91-94,305)
		R614L	MH	(71,74)
		E1058K	MH	(301)
		K1393R	MH	(301)
		R1679H	MH	(301)
		R2163C	MH	(69,71,74,305)
		R2163H	MH	(68,71,74,305)
		R2163 P	MH	(304)
		V2168M	MH	(69)
		T2206M	MH	(53)
		N2283H	CCD/MmD	(103)
		N2342S	MH	(304)
		ΔE2347	MH	(305)
		A2350T	MH	(55,76)
		R2355W	MH	(55)
		E2371G	MH	(304)
		G2375A	MH	(55)
		G2434R	MH	(71,74,306)
		R2435H	MH/CCD	(68,71,74)
		R2435L	MH/CCD	(64,305)
		I2453T	MH/CCD	(54)
		R2454H	MH/CCD	(304)
		R2458C	MH	(71,74)
		R2458H	MH	(69,71,74)
		R2458H/	MH	(56)
		R3348C	MH	(56)

Effect	Isoform	Mutation	Disease	References
Gain of function	RyR1	R2508C	MH/CCD	(307)
		R2508G	MH	(301)
		ΔR4214_	CCD	(308)
		F4216		
		T4637A	CCD	(305)
		Y4796C	CCD	(70,305)
		T4826I	MH	(63,69,97,309)
		H4833Y	MH	(97,258,310)
		R4861H	CCD	(65)
		ΔF4863_	CCD	(66)
		D4869		
		R4893W	CCD	(65)
		A4894T	MH	(98)
		I4898T	CCD	(65,73,94)
		G4899R	CCD	(65)
	RyR2	ΔExon 3	CPVT	(101)
		A77V	CPVT/ARVD2	(101)
		R176Q	ARVD2	(83,311-313)
		R176Q/T	ARVD2	(79,100,101,314)
		2504M		
		E189D	CPVT	(315)
		G230C	CPVT	(266,281)
		R420W	ARVD2	(101)
		L433P	ARVD2	(79,101,314)
		S2246L	CPVT	(79-81,100,316)
		R2267H	CPVT	(317)

Effect	Isoform	Mutation	Disease	References
Gain of function	RyR2	P2328S	CPVT	(266,318,319)
		N2386I	ARVD2	(311,314)
		R2474S	CPVT	(79,265,320)
		T2504M	ARVD2	(311)
		N4104K	CPVT	(26,80,81)
		Q4201R	CPVT	(79,100,319)
		R4497C	CPVT	(26,80,81,87)(59,82,321-323)
		S4565R	CPVT	(317)
		V4653F	CPVT	(100,319)
		I4867M	CPVT	(79)
		N4895D	CPVT	(26)
Loss of function	RyR1	S71Y/N2	CCD/MmD	(103)
		283H		
		R109W/ M485V	CCD/MmD	(96,103)
		C4664R	MH	(304)
		G4891R	CCD	(70)
		R4893W	CCD	(70,86)
		A4894P	CNMDU1	(98)
		I4898T	CCD	(67,70,73,86,94,97)(61,62,95)
		G4899R	CCD	(70,96,97)
		G4899E	CCD	(86,96)
		A4906V	CCD	(70)
		R4914G	CCD	(70)
		Δ V4927_ I4928	CCD	(96,308)

Effect	Isoform	Mutation	Disease	References
Loss of function	RyR2	L433P	ARVD2	(311)
		A1107M		
		(T1107M)	CPVT	(101)
		A4860G	IVF	(99,100)
Uncertain effects	RyR1	I403M	MH/CCD	(68)
		A1577T/		
		G2060C	CCD	(103)
		R2939K	MmD	(104)
		G3938A		
		(G3938D)	MH	(324)
		D3986A		
		(D3986E)	MH	(72)
	RyR2			